Fast Aeroelastic Analysis and Optimisation of Large Mixed Materials Wind Turbine Blades

Hegberg, Terry

DOI
10.4233/uuid:643ddf12-97d3-48a1-9742-b4dd22f16164

Publication date
2019

Document Version
Final published version

Citation (APA)
Hegberg, T. (2019). *Fast Aeroelastic Analysis and Optimisation of Large Mixed Materials Wind Turbine Blades*. [Dissertation (TU Delft), Delft University of Technology]. https://doi.org/10.4233/uuid:643ddf12-97d3-48a1-9742-b4dd22f16164

Important note
To cite this publication, please use the final published version (if applicable).
Please check the document version above.

Fast Aeroelastic Analysis and Optimisation of Large Mixed Materials Wind Turbine Blades

Fast Aeroelastic Analysis and Optimisation of Large Mixed Materials Wind Turbine Blades

Proefschrift

ter verkrijging van de graad van doctor
aan de Technische Universiteit Delft,
op gezag van de Rector Magnificus prof. dr. ir. T.H.J.J. van der Hagen,
voorzitter van het College voor Promoties,
in het openbaar te verdedigen op dinsdag 15 januari 2019 te 12.30 uur

door

Terry HEGBERG
Ingenieur Luchtvaart- en Ruimtevaarttechniek, Technische Universiteit Delft, Nederland
geboren te Zaandam, Nederland.

Dit proefschrift is goedgekeurd door de promotoren:
Prof. dr. G.J.W van Bussel
Dr. ir. R. De Breuker

Samenstelling promotiecommissie:

Rector Magnificus,	voorzitter
Prof. dr. G.J.W. van Bussel,	Technische Universiteit Delft, promotor
Dr. ir. R. De Breuker,	Technische Universiteit Delft, promotor

Onafhankelijke leden:

Prof. dr. ir. G.A.M. van Kuik,	Technische Universiteit Delft
Prof. dr. C.L. Bottasso,	Technical University Munich
Prof. dr. M.H. Hansen,	University of Southern Denmark
Dr. J.K.S. Dillinger,	German Aerospace Center
Dr. ir. H.E.N. Bersee,	Suzlon
Prof. dr. S.J. Watson,	Technische Universiteit Delft, reservelid

Keywords: Wind Energy, Aeroelasticity, Optimisation, Structural design.

Printed by: Gildeprint

ISBN 978-94-6323-473-3

Cover design by Sioe Wen Go. Picture from:
https://coloradosun.com/2018/12/06/tri-state-power-renewable-energy-colorado
by John Leyba: Special to The Colorado Sun

Printed in The Netherlands

Voor Sioe Wen, Gohan en Jadzia...

SUMMARY

In this dissertation, structural wind turbine blade layouts are presented that are suitable for 10MW and 20MW wind turbine blades. This has been accomplished by using a medium fidelity static aeroelastic model embedded in an optimisation framework. The structural solutions are the result of a stiffness optimisation where the blade mass is minimised. To accomplish the structurally optimised blade, an aeroelastic analysis model is set up. This model consists of a nonlinear structural analysis module and an aerodynamic module. Both models are comparable in terms of the level of physical modelling and as such, it can be said that both models are of equal fidelity. This equal fidelity is favourable for the aeroelastic coupling between both models, which generates an aeroelastic solution that is accurate up to the level of physics present in the aerodynamic and the structural models.

The structural modelling starts with defining the lay-up and the thickness distribution of all structural parts within the wind turbine blade. Then, a cross-sectional modeller reduces the degrees of freedom from the full 3D blade to cross-sectional properties in the prescribed 1D beam nodes. During this process, the orthotropic behaviour and the cross-sectional properties of the blade are preserved. The cross-sectional information is used for defining the Timoshenko beam elements within the finite element structural analysis of the blade. The external loads resulting from gravity act at the beam nodes and the centrifugal effect is implemented by putting the distributed centrifugal forces on the beam nodes as well. This analysis is embedded in a corotational framework, which means that geometrically nonlinear behaviour is included as well. As such, large blade tip deflections are also taken into account within this model.

The aerodynamic loads are determined using a vortex lattice method. The blade, being the bound surface, is divided into spanwise and chordwise vortex panels which are influenced by each other and vortex panels that form the rotating wake. For the wake, a cylindrical shape is assumed, which is sufficient for determining static aeroelastic blade loads. The induced drag results from the vortex lattice method and to account for parasite drag, aerodynamic drag coefficient tables are also included in the analysis.

The aeroelastic coupling is accomplished by using close coupling of the aerodynamic and structural model. For both the aerodynamic and the structural loads,

sensitivities are determined with respect to the structural degrees of freedom. This yields the aerodynamic and structural stiffness. A Newton-Raphson root finding algorithm is used to determine the converged aeroelastic solution for the blade deformation and the corresponding blade loads.

For the structural optimisation, the variable stiffness concept is used. The objective function calculates the blade mass, which is minimised, as a function of a vector of design variables that contains eight lamination parameters and thickness parameters per laminate used. The thickness parameters depend on using a pure fibre laminate or using a sandwich laminate. For pure fibre laminates only one thickness parameter is required, for sandwich laminates, two are required: one for the equal thickness facing sheets and one for the core. The optimiser used for this problem is the globally convergent method of moving asymptotes, which is a gradient-based method. Two load cases are selected for the optimisation procedure, namely, the normal wind profile and the extreme wind shear. The load cases mentioned are most suitable for static aeroelastic analyses and the extreme wind shear case covers a significant part of the load envelope. The selected constraints are the strain, buckling, tip deflection and, aerodynamic power loss. Because of the gradient-based optimisation, the sensitivities of the objective function and the constraints with respect to the design variables are determined as well.

The optimisations are carried out for 5MW, 10MW, and 20MW blades containing sandwich composites and blades only consisting of pure fibre laminates. In case of the sandwich composites, the blade structure consists of suction skin, pressure skin, spar caps, a front spar and a rear spar. Ribs and longitudinal stiffeners are not necessary in that case. In addition, the sandwich blade optimisation includes the possibility of using sandwich composites in the spar caps. For the pure fibre laminate blades, the suction skin, pressure skin, spar caps and the front and rear spars are present as well. The difference with sandwich skins is, that ribs and longitudinal stiffeners must be added to take care of the skin buckling resistance. For both the sandwich blade and the stiffened skin blade, the optimisation can be carried out for a hybrid composite material blade. The hybrid blade consists of eglass composites where parts of the spar caps are replaced by carbon composites.

The results show that all sandwich structural layouts arrive at a lower blade mass than the baselines. For the sandwich layout, it appeared that applying sandwich composites in the spar caps, a significant mass saving can be achieved, varying between 14% and 26% with respect to full fibre spar caps. Also, the stiffened skin blade structural layout shows lower masses compared to the baselines. However, more significant mass savings are observed for the sandwich blades, resulting in approximately 5% lower masses than the stiffened skin blades. Furthermore, it is observed that aeroelastic tailoring has some effect on the year power production, a production loss of 4.5% is calculated based on the optimised blades.
The blade mass as a function of wind turbine power can be compared to scaling laws from previous studies where the increase in nominal power estimates the

blade mass. It is observed that the optimised results do not follow the scaling laws. This can be an indication that the scaling laws cannot be used to scale towards a 20MW turbine and should be updated. Furthermore, from analyses where the blade mass is plotted against the percentage carbon fibre in the spar caps, it can be said that replacing glass fibres by carbon fibres in the spar caps only, is an efficient way to implement carbon fibre.

It is concluded that replacing full eglass fibre spar caps by eglass sandwich laminate spar caps for the sandwich layout is more favourable than eglass stiffened skin structural solutions. Both the sandwich and the stiffened skin concepts do have significantly lower mass than the baseline designs, however, the eglass sandwich design is in favour. Replacing the eglass fibres by carbon fibres within a predefined part of the spar caps gives another significant mass reduction. Especially, for the 20MW blade, the replacement of eglass fibres by carbon fibres within the spar caps proves to be efficient. The high internal spar cap loads show the limits of glass fibre sandwich laminates in terms of thick facing sheets and a vanishing core thickness at approximately 50% of the blade span. Using carbon fibre sandwich laminates, the facing sheet thickness reduces significantly and a thicker core remains. This results in significant mass reductions, while the blade parts are still able to resist buckling which is the critical constraint.
As a final remark, it can be said that the aeroelastic model makes it possible to perform a complete blade optimisation for different wind turbine blades. From the optimised blade results, it is possible to extract new design rules or adapt the previous ones. From the present research, for tailored blades, it seems that the classical power laws used for upscaling of the blades are not consistent in estimating blade masses for the 10MW and 20MW blades.

SAMENVATTING

In dit proefschrift worden constructieve lay-outs van windturbinebladen gepresenteerd die geschikt zijn voor 10MW en 20MW windturbinebladen. Dit wordt bereikt door een statisch aero-elastisch model van middelhoge betrouwbaarheid te gebruiken, geïmplementeerd in een optimalisatieroutine. De constructieve oplossingen volgen uit een stijfheidsoptimalisatie waarin de bladmassa wordt geminimaliseerd. Voor de geoptimaliseerde bladconstructie wordt een aero-elastisch model opgebouwd. Dit model bestaat uit een niet-lineaire constructieve module en een een aerodynamische module. Beide modellen zijn vergelijkbaar betreffende de details van de fysische modellering, dat betekent dat beide modellen een vergelijkbare betrouwbaarheid hebben betreffende de fysica. Deze vergelijkbare betrouwbaarheid is gunstig voor de aero-elastisch koppeling tussen beide modellen wat zich vertaald in een aeroelastische oplossing die zo nauwkeurig is als de fysica aanwezig in zowel het aerodynamisch model als het constructieve model.

De constructieve modellering begint met de initiële opbouw van de vezelrichtingen en de dikteverdelingen van de constructieve elementen van het blad. Vervolgens wordt de 3-dimensionale representatie van het blad gereduceerd naar oppervlaktes en oppervlaktetraagheidsgrootheden van de voorgeschreven knooppunten van het 1-dimensionale balkmodel door gebruik te maken van een reductiealgorithme voor doorsnede-oppervlaktes. Gedurende dit reductieproces, blijven het orthotropische karakter en de oppervlaktetraagheidsgrootheden van het blad behouden. Deze oppervlaktetraagheidsgrootheden worden gebruikt om de Timoshenko balkelementen te definiëren in de eindige elementen analyse van het blad. De uitwendige belastingen die volgen uit zwaartekracht worden als equivalente knooppuntbelastingen op de voorgeschreven balkknooppunten gezet en de centrifugaaleffecten worden gemodelleerd door de verdeelde centrifugaalkrachten ook op de voorgeschreven balkknooppunten te betrekken. Deze analyse is ingebed in een co-roterend assenstelsel wat betekent dat geometrische niet-lineair gedrag ook meegemodelleerd is. Grote tipverplaatsingen kunnen dus ook worden beschouwd in dit model.

De aero-elastische koppeling wordt bereikt door sterke koppeling tussen het aerodynamisch model en het constructieve model. Voor zowel het aerodynamisch model als het constructieve model worden gevoeligheden naar de constructieve graden van vrijheid bepaald. Dit resulteert in de aerodynamische stijfheid en con-

structieve stijfheid. Een Newton-Raphson nulpuntsbepaling wordt gebruikt om de geconvergeerde aero-elastische oplossing te bepalen voor de bladvervorming en de bijbehorende bladbelastingen.

Voor de optimalisatie van de bladconstructie, wordt het variabel stijfheidsconcept gebruikt. De doelfunctie berekent de bladmassa, die wordt geminimaliseerd, als een functie van de ontwerpvariabelen die bestaan uit acht laminatieparameters en een aantal dikteparameters per laminaat. De dikteparameters variëren per laminaattype: voor een puur vezellaminaat volstaat één dikteparameter, terwijl een sandwichlaminaat er minimaal twee nodig heeft, namelijk één voor de kerndikte en één voor de laminaatdikte als de laminaten gelijke dikte hebben. Het optimalisatiealgorithme dat is gebruikt, is de globaal convergente methode van meebewegende asymptoten. Deze methode is een op gradiënten gebaseerde optimalisatie. Voor de optimalisatie zijn twee load cases gekozen: het normale wind profiel en de extreme windgradiënt. De genoemde loadcases zijn het meest geschikt voor de quasi-statische optimalisatie en de extreme windgradiënt situatie dekt een belangrijk deel van het belastingsspectrum. De gekozen beperkende voorwaarden zijn rek, knik, tipuitwijking en aerodynamisch vermogensverlies. Door de gekozen optimalisatiemethode, zijn de gevoeligheden van de beperkende voorwaarden naar de ontwerpvariabelen ook nodig voor de gehele optimalisatieprocedure.

De optimalisaties zijn uitgevoerd voor 5MW, 10MW en 20MW bladen opgebouwd uit sandwichlaminaten maar ook voor bladen bestaande uit pure vezellaminaten. Voor de sandwichlaminaten, bestaat het blad uit onder- en overdrukhuid en een doosligger met 2 lijfplaten en 2 liggerflenzen. Ribben en langsverstijvers zijn niet nodig voor sandwich huiden. Bovendien is in de optimalisatie de mogelijkheid gecreëerd om de horizontale delen van de doosligger ook uit sandwichlaminaten te laten bestaan. Voor puur vezellaminaat bladen, de over- en onderdrukhuiden zijn verstijfd met ribben en langsverstijvers en de doosligger maakt ook deel uit van deze constructieve oplossing. De huiden dienen nu echter verstijfd te worden om huidknik tegen te gaan. Voor zowel de het sandwich blad als wel het puur vezel blad, worden de optimalisaties ook uitgevoerd met hybride composietmaterialen. Dit hybride blad bestaat dan uit huiden van glasvezel composiet maar een deel van de ligger, en dan slechts delen van de liggerflenzen, wordt vervangen door koolstofvezel composiet.

De resultaten laten zien dat alle sandwich bladen uitkomen op lagere bladmassa's vergeleken met de baseline bladen. Voor de sandwich lay-out blijkt dat, wanneer sandwich composieten ook in de liggerflenzen wordt gebruikt, een significante massabesparing wordt bereikt. Deze besparing ligt tussen de 14% en 26% ten opzichte van de puur vezellaminaat liggerflenzen. Ook de bladen met verstijfde huiden laten een lagere massa zien ten opzichte van de baseline. Echter, de bladmassa's komen lager uit met sandwich liggerflenzen, resulterend in 5% lagere massa's vergeleken met de bladen met het verstijfde huid concept. Verder blijkt uit de aero-elastiche optimalisatie dat een aerodynamisch vermogensverlies van

4.5% optreedt.
De bladmassa, als functie van het windturbinevermogen, kan worden vergeleken met schaalwetten van oudere studies waar uit de toename van het nominaal vermogen de bladmassa wordt geschat. Het blijkt dat de geoptimaliseerde bladen uit dit proefschrift de schaalwetten niet volgen. Dit kan een aanwijzing zijn dat de schaalwetten niet direct kunnen worden gebruikt om een schatting te maken voor een 20MW windtubine. Een update van de schaalwetten zou dan op zijn plaats zijn. Verder blijkt uit analyses gedaan door de bladmassa uit te zetten tegen het percentage koolstofvezel in de liggerflenzen, dat vervangen van glasvezel materialen door koolstofmaterialen efficiënt is.

Er kan worden geconcludeerd dat het vervangen van puur glasvezellaminaten door glasvezel sandwichlaminaten in de liggerflenzen van de bladen met de sandwich lay-out gunstiger is dan het toepassen van het hele blad uit te voeren met het verstijfde huid concept. Zowel het verstijfde huid concept als het sandwich concept geeft als oplossing bladen met lagere massa's dan die van de baseline ontwerpen, echter, de glasvezel sandwich combinatie geeft lichtere bladen. Vervangen van glasvezel door koolstofvezel in een voorgeschreven deel van de liggerflenzen geeft nog eens een extra massabesparing. Voornamelijk het 20MW blad ondervindt voordelen van koolstofvezel in de flenzen. De hoge interne flensbelastingen laten zien dat op ongeveer 50% van de bladradius, de glasvezels de limiet bereiken voor dit 20MW bladontwerp door laminaten die de het kernmateriaal verdringen voor de sandwich lay-out. Gebruik van koolstofvezel reduceert de laminaatdikte weer en de kern krijgt dan ook weer dikte. Dit resulteert in een significante afname van de bladmassa terwijl huidknik, welke beperking kritiek blijkt te zijn, geen probleem meer is.
Als een laatste opmerking, kan worden gezegd dat het aero-elastisch model het mogelijk maakt complete bladoptimalisaties te doen voor verschillende windturbinebladen. Uit de optimalisatieresultaten van de bladen, kunnen nieuwe ontwerpregels worden opgesteld of kunnen oude worden bijgesteld. Uit deze studie blijkt bijvoorbeeld dat, voor geoptimaliseerde bladen, de klassieke opschalingswetten voor bladen niet consistent zijn voor het inschatten van de bladmassa's van 10MW en 20MW bladen.

NOMENCLATURE

ROMAN SYMBOLS

A	Cross-sectional area	m^2
$\mathbf{A}$	Aerodynamic influence coefficient matrix	
$\mathbf{A}$	Laminate in-plane stiffness matrix	N/m
$\mathbf{B}$	Laminate coupling stiffness matrix	N
c	Chord	m
c_d	Section drag coefficient	-
C	Cross-sectional property term in cross-sectional tensor $\mathbf{C}$	
$\mathbf{c}$	Chord vector	m
$\mathbf{C}$	Cross-sectional tensor	
$\mathbf{D}$	Laminate out-of-plane stiffness matrix	N m
$\mathbf{D}$	Drag vector	N
E	Young's modulus	N/m^2
$\mathbf{e}$	Unit vector	
$\mathbf{f}$	Force vector	N
$\mathbf{F}$	Force vector	N
g	Gravitational acceleration	m/s^2
G	Shear stiffness	N/m^2
h	Single layer thickness of a laminate	m
$\mathbf{H}$	Buckling stiffness properties	
I	Second moment of area	m^4
J	Polar area moment of inertia	m^4
$\mathbf{J}$	Jacobi matrix	
$\mathbf{K}$	Stiffness matrix	
$\mathbf{L}$	Lift vector	N
m	Mass	kg
M	Stress resultant moments per unit length	Nm/m
N	Stress resultant forces per unit length	N/m
$\mathbf{n}$	Unit normal vector for vortex panels	-

$\mathbf{p}$	Structural degree of freedom vector	
$\mathbf{Q}$	Stiffness matrix from constitutive equation	N/m^2
R	Rotor radius	m
$\mathbf{r}$	Vector between two points	m
$\mathbf{R}$	Residual vector	
$\boldsymbol{\mathcal{R}}$	Rotation matrix	
R	Radius of curvature of cylindrical buckling panel	m
S	Material strength in shear	N/m^2
S	Surface area	m^2
t	Total laminate thickness	m
$\mathbf{t}$	Sandwich laminate thickness vector	m
$\mathbf{T}$	Coordinate system	
$\mathbf{T}$	Rotation matrix used within lamination theory	
u	flow velocity in $\mathbf{e}_1^b$ direction	m/s
U	Material invariant terms for $\boldsymbol{\Gamma}$ matrices	N/m^2
v	flow velocity in $\mathbf{e}_2^b$ direction	m/s
V	Lamination parameter	
V	Volume	m^3
$\mathbf{V}$	Velocity vector	m/s
w	flow velocity in $\mathbf{e}_3^b$ direction	m/s
x	x-Coordinate	m
X	Material strength in 0-direction	N/m^2
$\mathbf{x}$	Position vector	m
$\mathbf{X}$	Inertial position coordinate	m
y	y-Coordinate	m
Y	Material strength in 90-direction	N/m^2
z	z-Coordinate	m

Greek Symbols

α	Angle of attack	rad
γ	Shear strain	-
Γ	Circulation	m^2/s
$\boldsymbol{\Gamma}$	Material invariant matrix	
ϵ	Membrane strain	-
$\boldsymbol{\epsilon}$	Strain vector	-
η	Number of half waves in lateral direction	
θ	Rotational deformation	rad

κ	Bending strain	-
λ	Number of half waves in longitudinal direction	
λ	Load variation parameter for nonlinear load analysis	
$\boldsymbol{\xi}$	Design variable vector	
ρ	Density	kg/m^2
$\boldsymbol{\sigma}$	Stress vector	-
ϕ	Two dimensional displacement function	-
ϕ	Local inflow angle	
ϕ	Perturbation velocity potential	m^2/s
Ψ	Blade azimuth	deg

Sub/Superscripts

0	Rotating body axis frame fixed at blade root
∞	Freestream conditions
0	Undeformed
a	Aerodynamic load
B	Body axis frame attached to tower
b	Non-rotating body axis frame fixed at blade root
c	Compressive
c	Core of a sandwich composite laminate
e	External load
f	Facing sheet of a sandwich composite laminate
g	Geometric
g	Global reference frame
I	Inertial
k	The $k^{th} layer within a composite laminate$
l	Local reference frame
r	Rigid reference frame
s	Structural load
t	Tangential
t	Tensile
w	Wake surface

Abbreviations

BECAS	Beam Cross-sectional analysis software
BEM	Blade element momentum theory

CFD	Computational fluid dynamics
EWS	Extreme wind shear
FEM	Finite element method
GCMMA	Globally convergent method of moving asymptotes
GDW	General dynamic wake
IEC	International electrotechnical commission
MBS	Multi-body system
NREL	National renewable energy laboratory
NWP	Normal wind profile

CONTENTS

1

Introduction

The world energy demand increases due to modern society. Because of population growth together with the use of modern equipment, energy consumption keeps growing. In the future, mining fossil fuels requires technologically more advanced and expensive solutions. Furthermore, the use of these sources of energy loses public support due to, for instance, strong signals indicating climate change and pollution. As such, the focus on optimising renewable energy sources should increase.

This research focuses on wind energy in particular. Wind energy becomes more and more accepted as a cost-effective renewable energy source for the generation of electricity. With the increasing demand of this resource, efficiency is improved by increasing the power or by reducing the cost of a single wind turbine. For more efficient wind turbines, one could choose for increased hub height, which increases the average aerodynamic power because of increased average wind velocity. The velocity increase gives a significant amount of aerodynamic power increase since the relation between aerodynamic power and wind velocity is cubic. Even more important is the rotor area of the turbine. The power and the area relate linearly, as a consequence, rotor radius relates in a quadratic way to energy yield. This explains the very large dimensions of modern multi-MegaWatt wind turbines. Large wind turbines in large wind farms seem a cost-effective choice for competing with other ways of electricity generation. Recent tender procedures demonstrate the cost-effectiveness of large off-shore wind farms. Those farms are located fairly close to the shore at limited water depth.

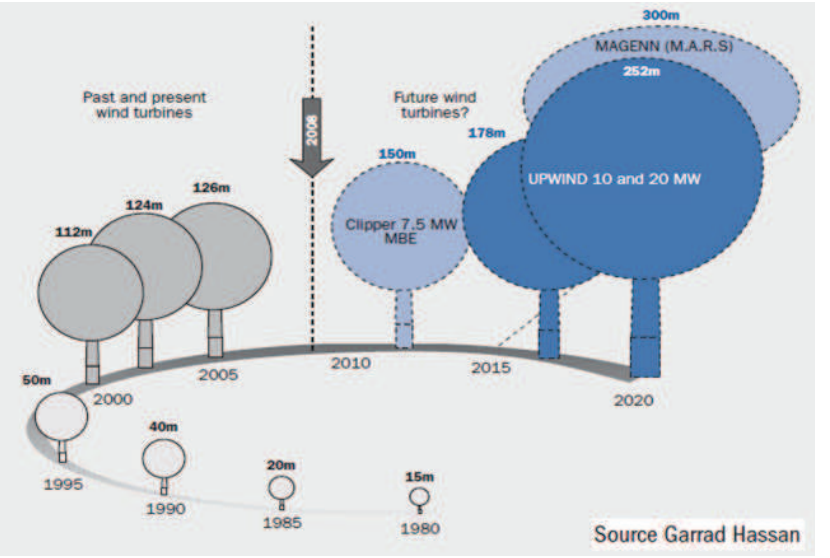

Figure 1.1: Development of wind turbine dimensions over the years.

Figure 1.1 shows the wind turbine current dimensions and some future developments. It is clear that future rotor diameters are growing larger and larger, which will cause additional blade loading: rotor blades moving through the gravitational field cause a significant increase in cyclic loading, and as such the fatigue life could decrease. This finally results in rotors where the gravitational force is the critical loading. Furthermore, the rotor overhang should increase for large rotor blades to account for the increase in tip deflection and as such, for sufficient tower clearance. This increased overhang introduces significant loads in the tower, so mass minimisation is important as well as increased blade stiffness to reduce the maximum tip deflection and as such to reduce the necessary rotor overhang for the required tower clearance. In most rotor designs tower clearance is solved by tilting the rotor a few degrees. Also, pre-cone and pre-bend are applied in some rotor designs. The pre-cone or the pre-bend moves the tips out of the rotor plane, opposite to the undisturbed wind velocity. Some blade manufacturers include in-plane curvature to enhance the bend-twist coupling effect. This is mainly done to reduce loads but could also have some effect on the tip location and, therefore, the tower clearance is increased, as indicated in the recent work of [Scott et al., 2017]. Pre-cone or pre-bend solutions are expected to affect the aerodynamic performance slightly because the actual rotor plane area has slightly decreased compared to the reference rotor plane area. On the other hand, the rotor overhang issue is solved. Another way to reduce or solve the rotor overhang problem is to apply aeroelastic tailoring where mass is minimised and stiffness is constrained by means of a maximum tip deflection. As a secondary effect, the aerodynamic power loss can

be restricted while only optimising the blade structural design: the external blade shape is not changed.

For the structural optimisation of the blade, two structural blade layout changes are proposed. The first layout maintains the sandwich structure but the suction and pressure side of the torsion box will contain sandwich composites as well, the second layout will replace the complete sandwich composite layout by a stiffened skin concept, which means that the sandwich skin is replaced by pure fibre laminate skin stiffened by longitudinal stiffeners and ribs. The torsion box, as in the first proposed layout, is maintained. These structural concepts are proposed because it is expected that they satisfy the stiffness requirements that are imposed by the tower clearance, under the condition that the mass is minimised as well. Furthermore, transport becomes an issue. Large blades should be transported to the turbine site and locally mounted to their operational length. For such problems, stiffened skin blades would be more suitable. In the section below, several issues will be discussed that involve the structural design of wind turbine blades.

1.1 State-of-the-Art of aeroelastic modelling and structural design

1.1.1 Aeroelastic modelling

Many aeroelastic analyses are carried out using an accurate aerodynamic model and a low fidelity structural model or using an accurate finite element model for the structural modelling and a low fidelity aerodynamic model. Examples are the research of [Ferede, 2016] where a full 3D structural layout is subjected to a force distribution resulting from simple blade element momentum theory (BEM). Another example is [Bernhammer, 2015], where quite some attention is given to a multibody dynamics formulation but the aerodynamics is still based on a BEM approach. On the other hand, the BEM based design models are extensively validated and many corrections were added as can be found in [Hansen et al., 2006], [Leishman, 2002], and [Sanderse, 2009], which still makes BEM based models a valuable aerodynamic blade design tool. A more extensive overview of aeroelastic codes is given in Table 1.1.

This overview shows that the leading codes for aeroelastic analysis and design of horizontal axis wind turbines use BEM theory. As an improvement for the unsteady wake, BLADED, HAWC and FAST use the generalized dynamic wake model. The generalized dynamic wake model is based on the acceleration potential method which includes dynamic inflow, yawed flow and tip loss effects inherently. Furthermore, some aeroelastic codes use a corotational approach as well as the cross-sectional modelling technique BECAS (BEam Cross-sectional Analysis Software) as described in [Blasques and Lazarov, 2011]. The results

Table 1.1: Aerodynamic and structural modelling strategies used in the state-of-the-art aeroelastic codes according to [Passon et al., 2007]. GDW - Generalized dynamic wake, Modal refers to the structural dynamic analysis, and MBS - Multi-body system referring to the structural dynamic modelling strategy.

	GH Bladed	**HAWC**	**BHAWC**	**FAST**	**Flex5**
Aerodynamic modelling	BEM GDW	BEM GDW	BEM GDW	BEM	BEM
Structural modelling	FEM Modal	FEM	FEM Corotational formulation	MBS Modal	FEM

from BECAS are equivalent to the results of VABS (Variational Asymptotic Beam Section analysis). Amongst others, [Chen, 2010] points out that VABS is the most reliable cross-sectional tool. It is applied for wind turbine blades by [Cesnik and Hodges, 1997] and is a relatively new concept in wind turbine blade modelling. Considering the cross-sectional modelling of shell structures, an improved model has been developed at the Delft University of Technology and is described in [Ferede, 2016] and [Willaert and Abdalla, 2010]. This tool also transforms a detailed 3-dimensional structure into a 1-dimensional element and preserves all cross-sectional properties more accurate. In addition, the orthotropic behaviour of laminates is preserved as well in this model.

The corotational formulation allows large blade deflections as a result of geometric nonlinearities. It has been implemented in the aeroelastic code BHawC from Siemens-Gamesa, see [Passon et al., 2007] but the aerodynamics is BEM based, however, it also offers the possibility to couple a computational fluid dynamics model. The importance of modelling of nonlinear structural behaviour for large blades also has been pointed out in [Freno et al., 2011]. Within the corotational framework, the results from the cross-sectional modeller are used in a finite element formulation using Euler-Bernoulli beam elements or Timoshenko beam elements as described in [Hodges and Yu, 2007]. Combining a cross-sectional modeller to reduce a 3-dimensional blade model in a 1-dimensional beam model with a corotational approach in which the loads are identified is an interesting basis for an equal fidelity aeroelastic model, especially if the aerodynamic model is also based on a 3-dimensional model that has been reduced to a 1-dimensional line model. The idea of equal fidelity is that the physics within the models that are combined and the reduction of the models are comparable. To roughly define low, medium and high fidelity, aerodynamic modelling is considered as an example. For low fidelity, the blade element momentum physics can be considered, for medium fidelity velocity potential or acceleration potential solutions, and high fidelity can be considered computational fluid dynamics where the full set of Navier Stokes equations is solved.

For aeroelastic modelling, this means that if the 3D structural is reduced to a 1D beam element, the cross-sectional information of the 3D structure is maintained,

and can be referred to as a medium fidelity structural model. Combining this with a multi-panel aerodynamic vortex model, which is also of medium fidelity, this equal fidelity of both the structural model and the aerodynamic model gives the aeroelastic solution comparable accuracy. This equal fidelity of both models is important for optimisations where aeroelastic behaviour is a key issue.

1.1.2 Structural design

Most blades of recently installed wind turbines have a structural layout as is shown in Figure 1.2. This picture shows that for the blade cross-section, the torsion box layout is used, consisting of the shear webs and the spar caps. The skins and spars consist of sandwich laminates.

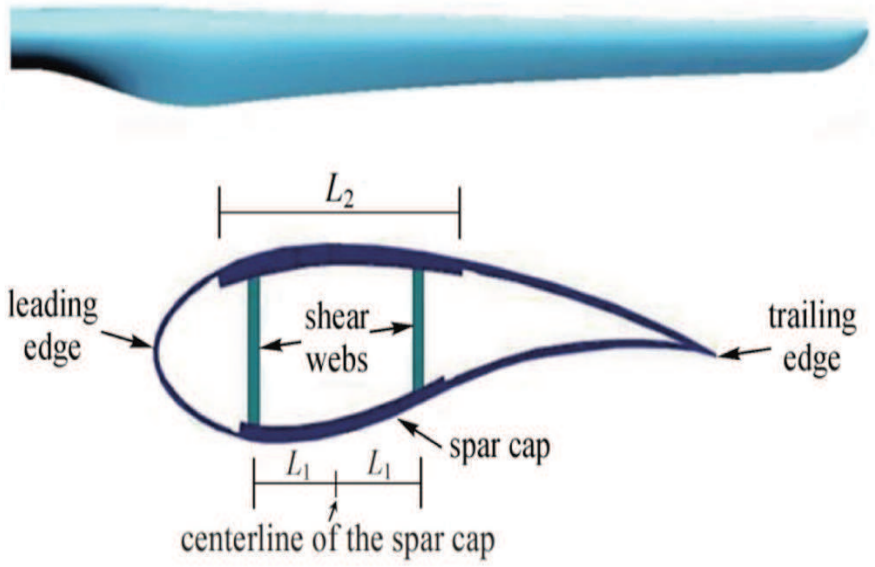

Figure 1.2: Structural lay-out of a large sandwich blade, from [Zhu et al., 2014].

The spar cap skin is a pure fibre laminate and the spars and remaining skin parts are sandwich laminates. In [Jackson et al., 2005] it is concluded, amongst others, that a mix of different composite materials has a positive effect on weight savings, even when additional material costs are taken into account: the cost increase for using S-glass or carbon is quite modest. Other studies as [Joncas, 2010] point out that it might have some advantages to apply a stiffened structural layout for wind turbine blades, as used in aircraft wing structures. In that case, the blade structure includes ribs and skin stiffeners together with the wing box design. [Joncas, 2010] finds a result via a topology optimisation of a thermoplastic wind turbine blade that converges to a such a skin stiffened structural layout, includ-

ing wing ribs that determine the dimensions of the skin and spar buckling panels. Longitudinal skin reinforcing stiffeners, however, are not a result of this optimisation. For large wind turbine blades, it will be obvious that the skin strains, and therefore the stresses, increase because of blade stiffness that should restrict the tip deflection for sufficient tower clearance. As a consequence, it is worth to think of redesigning the structural layout of a wind turbine blade and propose a different lay-up but maintaining the sandwich composite layout or propose a fully stiffened skin set-up. It should be noted, however, that wind turbine blade tailoring is not new, see [Goeij, 1999], but the issues mentioned above might provide some new insights.

1.2 Minimising blade mass and blade optimisation

For wind energy, it is important that electricity from wind arrives at the same cost level as the conventional generation of electricity. The blade shape should be such that it extracts as much power from the wind as possible over a large range of wind velocities. This requires an optimum aerodynamic design of the blade: a well-known method is using the BEM approach and design the airfoil distribution, blade chord distribution and the blade built-in twist distribution to find an optimum value for the average annual energy yield. A procedure for such a shape optimisation is explained in [Hansen, 2003]. However, due to structural deformations, the aerodynamic loads change and to account for that, an aeroelastic blade design method should be used for finding an optimum blade result. In such a way, the structural design determines the blade deformations to have a minimum negative effect on the aerodynamic power. The aerodynamic loads, the blade gravitational and the centrifugal forces in combination with the blade deflections can be used for a stiffness optimization where the mass of the blade could be chosen as an objective. An extensive review of optimization within the field of wind turbines is given in [Chehouri et al., 2015]. This gives a clear picture of the state-of-art of the use of objective functions, constraints, design variables and the optimisation strategies used. Few studies assume that, instead of minimizing the cost of energy, blade mass could be chosen as objective. [Liao et al., 2012] and [Zhu et al., 2012] only chose to optimise spar caps, [Jureczko et al., 2005] performs a shape optimisation using commercial codes. A more recent study performed by [Scott et al., 2017] mentions that large blades might require a different design philosophy. For instance, aeroelastic tailoring was proposed to reduce blade loads by bend-twist coupling and let this mechanism control the local pitch angle of the blade. The bend-twist mechanism is implemented by pure material behaviour or a combined blade shape-material bend-twist coupling mechanism. Of course, the objective is to improve the aerodynamic power and a blade that maintains, approximately, its baseline design mass and stiffness. The results showed a

decreased root bending moments but slightly increased blade masses using some variable stiffness concept. In this research, bend-twist coupling could be a result of the optimisations. However, it is not a separate research goal. The IEA Wind task 37, takes optimisations of the complete wind energy converter into account, see [IEA, 2015]. Another recent work optimises for the structure and the aerodynamics of rotor blades. In [Bottasso et al., 2016], an aerodynamic shape optimisation is carried out together with aeroelastic tailoring of the spar caps. The eventual objective is chosen to be the cost of energy. Minimised blade mass is a significant objective as well, especially for increasing blade radii crossing the gravitational field: fatigue due to deterministic cyclic gravity loads becomes more of an issue. Also extreme load cases have a stronger effect on the structural design of large blades. Furthermore, manufacturers need less material which can lead to a reduction in manufacturing costs. In this research, it is proposed, therefore, to use aeroelastic tailoring and the variable stiffness concept to optimise for the blade mass.

1.3 Aeroelastic Tailoring

The concept of aeroelastic tailoring originates from aerospace engineering as carried out by [Weisshaar, 1987]. Aeroelastic tailoring is also used for helicopter blade improvements, however, in [Veers et al., 1998] one is aware of slightly different objectives for helicopters in comparison with wind turbine blades. For helicopter blades, one ensures in-plane rotor stability and minimised vibration without deteriorating the performance and fatigue life; cost-driven wind turbine blades are designed for maximum performance without losing rotor stability and fatigue life. In the early wind turbine blade design era, tailoring was not meant primarily for lowering blade mass but to reduce loads, to avoid unwanted aeroelastic responses, and to improve the aerodynamic power output. Examples of this are the use of bend-twist coupling as described in [Karaolis et al., 1989]. This smart use of materials is based on the behaviour of composite materials as presented in [Chandra and Chopra, 1992] and recently also by [Scott et al., 2017] for adaptive blades. The idea of weight reduction using aeroelastic tailoring is not new as well, see [Bielawa, 1971]. In this case, tailoring was used as a tool to control the eigenfrequencies of structures. Another example of an aeroelastic tailored wind turbine blade is the Carter turbine from the eighties. Amongst others, this turbine is described in [Aerotrope, 1995] and an image is shown in Figure 1.3.

The Carter turbine is a downwind turbine, which gives a possibility for the blades to allow large deformations. Especially for high wind conditions, the blade is able to deform such that the fatigue loads reduce significantly. Furthermore, the blade pitch was taken care of by elastic twisting of the blade spar, for the stall regulated control strategy of the blades. The tailoring objective for this turbine seems to be mainly for blade control in extreme wind conditions. Large blade

Figure 1.3: The Carter 300kW wind turbine. Source: Aerotrope.

deformations are limited for upwind rotor blade configurations because of the tower clearance constraint. Tailoring studies of upwind wind turbine blades can be found in [Ferede, 2016], for stall regulated 5MW blades. For 10MW, pitch regulated blades, [Zhale et al., 2016] combined an aerodynamic and a structural optimisation, where the objective function was the annual energy production. For pitch regulated turbine blades with radii towards 130 meters, it is favourable to reduce the mass significantly, amongst others, for the cyclic variation of the gravitational load. For this reason, blade mass minimisation is a sound objective for improving 10MW and 20MW turbine blade structural designs.

1.4 Up-scaling of Wind Turbine Blades

Many reasons can be mentioned for up-scaling studies of blades, one of them could be that to maintain the well-known blade design procedure. Several studies were performed to find proper scaling rules considering power, accompanying mechanical stresses and increase in blade mass. Some typical scaling rules for the blade mass are given in [Fingersh et al., 2006] and [Chaviaropoulos, 2007].

It should be noted that the mass not completely has a cubic dependence on the rotor radius, which is, amongst others, due to the development of technology and of course the environmental influences of the behaviour of the wind and, blade deformation. [Nijssen et al., 2001] uses a scaling law in between 4.1 and 4.2, but

many variations were used as mentioned in [Sieros et al., 2012].

The progress in upscaling methods is found in e.g. [Ashuri et al., 2010] and [Castillo Capponi et al., 2011]. The progress in rotor blade technology is not a constant factor in time and technology is generally improving. Due to this, the scaling laws are not always up to date and should be updated now and then. Furthermore, an improved, nonlinear up-scaling method is being developed where basically the internal blade loads are kept to the level of the NREL 5MW baseline. This has a complication: the scaled blade mass is significantly higher for the non-linear method than for the linear method. For either method, the result is an infeasible design, especially for the 20MW turbine configuration. This complication can be solved using aeroelastic tailoring to reduce the blade mass and as a result, the stress levels stay below the allowed stresses for the materials used.

1.5 Research goal

Considering the overview of the previous sections, it is observed that:

- equal fidelity aeroelastic modelling for optimisations purposes can be improved,
- most research is carried out on blade optimisation, but mainly by means of reducing loads and as a secondary effect, reducing mass. With increasing blade dimensions, mass minimisation is chosen to be an objective, with load reduction as a logical consequence,
- to satisfy stiffness constraints, the current blade structural layout may not be not sufficient for large blades. A different, novel structural layout can solve the stiffness constraint problem,
- traditional upscaling laws might not produce convenient results for designing large wind turbine blades, stiffness optimisations using mass as the objective function can be used to update the existing scaling laws.

To address the issues mentioned above, the research goals are formulated by defining the main research question:

Find an optimum structural and material layout for large wind turbine blades using an equal fidelity aeroelastic analysis code suitable for optimisation purposes.

This main research question can be answered by defining the following sub-questions:

- How can a computationally fast equal fidelity aeroelastic model be formulated for large wind turbine blades, suitable for optimisation purposes?

- What is a suitable optimisation procedure?
- What structurally optimised blade and material layouts will appear?

The equal fidelity modelling part includes matching the level of physical modelling of the structural model and the aerodynamic model. The question then is what aerodynamic modelling strategy has a comparable fidelity regarding a Timoshenko beam finite element model, originating from an advanced cross-sectional model?

Furthermore, the structural layout of state-of-the-art wind turbine blades, mainly existing of sandwich panels to resist buckling, is changed in the stiffened skin adopted from aeronautics by means of longitudinal stiffeners and ribs, following the research of Joncas [Joncas, 2010], where a topology optimization converged towards the conventional aircraft wing design. It will also be investigated whether the use of different fibre orientations is of advantage for the structural design besides the fact that costs will be probably higher. The new structural layout will first be compared with the NREL 5MW baseline. The same procedure is followed for a single 10MW rotor blade from DTU [Bak et al., 2013], and for the 20MW preliminary design of ECN, see [Peeringa et al., 2011]. The altered structural layout is obtained by optimising for minimum blade mass using the laminate thickness and the fibre orientation of the skin and spars by means of the variable stiffness concept.

1.6 CHOICES WITHIN THIS RESEARCH

During this research, possible trends are investigated concerning the relationship between the structural and material layout of a large wind turbine blade and the blade mass for increasing nominal aerodynamic power. The NREL 5MW turbine is considered as the baseline and the future trends are represented by blades from 10MW and 20MW wind turbines. Furthermore, only the aeroelastic behaviour up to rated power is considered, which allows the assumption that the flow of a single blade stays attached. Near the blade root, not much lift is generated and since the distance with respect to the blade root is small, the contribution of the aerodynamic loading to the total aerodynamic power is considered to be negligible. As a consequence of this assumption, typical aeroelastic phenomena that occur in the above-rated region are not taken into account in this research.

Furthermore, the optimisations are only performed assuming balanced, symmetric laminates to show whether significant mass savings are obtained. Symmetric laminates do not posses coupling effects as in-plane loadings resulting in out-of-plane deformations and out-of-plane loadings resulting in in-plane deformations. Balanced and unbalanced laminates are symmetric laminates, where symmetric laminates are defined as laminates where the fibre orientation of a single layer is mirrored with respect to the midplane. For unbalanced laminates, the orientation

of a layer is maintained with respect to the midplane, after mirroring. The layer thickness is mirrored with respect to the midplane as well, due to the definition of a symmetric laminate. One could propose using unbalanced, symmetric laminates for this research as well. For instance, [Ferede, 2016] used both balanced and unbalanced laminates. The unbalanced laminates were particularly used to increase the effect of the bend-twist coupling for the stall regulated turbines. He also used balanced laminates and his research showed significant mass savings. With this knowledge, it is decided to use balanced laminates only, to get a good, yet indicative idea of the mass saving potential.

Another important choice is that only steady aerodynamics is considered. It is realised that wind turbine rotors are quite dynamic structures and also the aerodynamics is unsteady, yet it is chosen to consider the blade structural layout changes for steady cases. For steady cases, wind shear and yaw are allowed since such cases show only slow changes in wind velocity, and as such, they can be referred to as steady. Changes in blade pitch, however, cause quick changes in aerodynamic loading and are referred to as unsteady cases. Both steady and unsteady cases are inherently present within a vortex model as used in this work, however, the unsteady aerodynamics is not a subject within this research. To account for a feasible structural layout, it has been decided to consider a severe steady load case for the optimisation: extreme wind shear. This load case is the heaviest case within the steady aerodynamics range, according to [IEC, 2005]. For a more refined design of an optimised blade, it should be subjected to several unsteady load cases. It could be that the resulting optimised blade does not fit the complete envelope, which means that the design should be adapted. During this work, the goal is to search for trends in structural layout to realise reduced blade mass but to maintain an appropriate blade stiffness distribution. All blades are optimised using the same optimisation procedure, such that the relative comparison is still objective.

1.7 Thesis outline

This section describes the main steps during the research, finally leading to the project results and conclusions. In short, using an equal fidelity aeroelastic analysis method embedded within a gradient-based optimiser, two different types of structural layout of large wind turbine blades were optimised for minimisation of the blade mass. The set-up of the models and the optimisation results following from the main research steps are structured by separate chapters.

In chapter 2, the equal fidelity aeroelastic model is explained. The basic concepts considered are axis transformation for describing aerodynamic loads and structural deformations. Also, some specific external loads acting on wind turbine blades are introduced and it is clarified how they are implemented in the struc-

tural model. That is, the external loads such as gravity and centrifugal loads are non-follower forces but must still be transformed to the local beam coordinate system where the deformations are determined. Furthermore, a simple representation of sandwich laminates using lamination parameters is discussed as well as the advanced cross-sectional modelling of airfoil cross-sectional shapes existing of the sandwich laminates. Also, because some locations within a wind turbine blade are buckling sensitive, a buckling model is used and is described as well. The aerodynamic blade element representation of the wind turbine blade is combined with a vortex panel method which gives the aerodynamic model higher fidelity than the blade element momentum formulation. Next, it is described how the aerodynamic loads are coupled to a 1-dimensional Timoshenko beam element within the corotational framework and why the linear stress-strain assumption is valid within the corotational formulation. After elaborating on the structural and the aerodynamic models, the models are coupled using close coupling which means that the necessary sensitivities of the aerodynamic model with respect to the structural degrees of freedom have to be determined. To finish the chapter, the validation of the aeroelastic model for the 5MW NREL rotor blade is performed such that it can be used with confidence for the optimisation.

In chapter 3, the optimisation procedure is explained by means of a flow chart. Then, the objective function is described as well as the sensitivities, especially the inclusion of the sandwich composite within the objective mass and the design variable vector is pointed out. Furthermore, some constraint functions or variables and their sensitivities with respect to design variables are defined if not already done in chapter 2. Next, the design formulation is presented in terms of load cases and design variables required for the optimisation. Lastly, the wind turbine blades considered are shortly described.

Chapter 4 is dedicated to the optimisation of large wind turbine blades. First, the blade structural elements are all composed of sandwich skins and spars. Also, the spar caps are modelled as sandwich composites. Since the state-of-the-art turbine blades have full-fibre composites spar caps, some optimisations are performed for this case as well. The optimisations for the full sandwich blade are performed for the 5MW to compare with the baseline, and for the 10MW and 20MW turbines to find differences between optimised blade designs and the blades generated from up-scaling laws. Next, the sandwich composite will be replaced by a skin stiffened lay-out for the spars and the skin, without altering the wing box and the aerodynamic blade shape. This structural layout is applied for the 5MW, 10MW, and the 20MW turbine blades as well. The chapter continues with an analysis of the behaviour of the sandwich spar caps in comparison with the full-fibre composite spar caps. Also, due to stiffness and strength problems for 10MW or 20MW blades, some spar cap e-glass composite material has been replaced by carbon composite material to observe the effect on blade mass and accompanying stiffness and strength. Then, as a final step, trends are presented considering blade masses against the percentage of carbon fibre in the spar caps and the blade mass

against nominal aerodynamic power.

The thesis finishes with conclusions and recommendations about the optimisation results and a short outlook concerning the future of tailoring of wind turbine blades.

2

Equal Fidelity Static Aeroelastic Modelling of Large Blades

In this chapter, the structure of the aeroelastic model for a wind turbine blade is presented. The model exists of a structural model and an aerodynamic model where the aerodynamics is suitable for wind turbine blades operating in attached flow conditions. Both models interact by means of close aeroelastic coupling. Since the blades are built of composite materials, appropriate stress and strain relations due to external loading are used to model the internal loads. The specific case of sandwich laminates is described and is coupled to the concept of lamination parameters: the relation between the **ABD** matrix and the lamination parameters is explained. The lamination parameters are used for reducing the computational effort during the optimisation procedure in which the aeroelastic model is implemented, and to facilitate continuous optimisation.
The structural model uses linear Timoshenko beam elements embedded in a corotational framework. In this manner, large blade deflections can be analysed. The cross-sectional properties for the beam elements are provided by a cross-sectional modeller that preserves the orthotropic behaviour of the composite materials using the strain energy concept. The aerodynamic model is of a different nature compared to the models used in the state-of-the-art wind turbine aeroelastic codes. Those common aerodynamic models are based on blade element momentum the-

ory including the necessary engineering correction models. Examples of engineering correction models are Prandtl's finite blade correction, Glauert's high loading correction, blade-blade interaction, and the dynamic inflow correction model. During this research, vortex panels are used for modelling the deformed blade and the wake. As such, these blade element momentum correction models do not need to be implemented.
For the closely coupled aeroelastic solutions, the sensitivities of the structural forces and the aerodynamic forces with respect to the structural degrees of freedom are required. The obtained sensitivities represent the structural stiffness matrix and the aerodynamic stiffness matrix; these are required for the static aeroelastic equilibrium equation. For the nonlinear solution of the equation, the Newton-Raphson root finding algorithm is used.
The aeroelastic model, implemented in PROTEUS being the computer code, is applied for the NREL 5MW reference rotor blade for validation, where the normal and tangential force distribution, aerodynamic power per blade as a function of wind velocity, and the tip displacement as a function of the wind velocity are considered as validation cases.

2.1 WIND TURBINE BLADE REFERENCE FRAMES

For the load calculation on wind turbine blades, a number of coordinate transformations are necessary. The wind velocity is expressed in an inertial axis frame and the blade loads are calculated in the local, rotating axis system. The transformations to be done are:

- From tower body axis frame $\mathbf{T}_B = \left[\mathbf{e}_1^B\ \mathbf{e}_2^B\ \mathbf{e}_3^B\right]$ to the non-rotating body axis system fixed at the blade root, $\mathbf{T}_b = \left[\mathbf{e}_1^b\ \mathbf{e}_2^b\ \mathbf{e}_3^b\right]$. The origin of the non-rotating blade system is located at the blade root, i.e. $\mathbf{x}_b = \mathbf{0}$;
- From the non-rotating blade root system to the rotating axis system at the blade root $\mathbf{T}_0 = \left[\mathbf{e}_1^0\ \mathbf{e}_2^0\ \mathbf{e}_3^0\right]$. The origin is also located at the blade root, with the rotation center at the blade root.

The transformation matrices look as follows:

$$\boldsymbol{\mathcal{R}}_B = \begin{pmatrix} 0 & 1 & 0 \\ 0 & 0 & -1 \\ 1 & 0 & 0 \end{pmatrix}, \quad \boldsymbol{\mathcal{R}}_0 = \begin{pmatrix} \cos\Psi & \sin\Psi & 0 \\ -\sin\Psi & \cos\Psi & 0 \\ 0 & 0 & 1 \end{pmatrix}. \tag{2.1}$$

To account for large blade deflections, geometric nonlinearities are introduced by using a corotational framework. This corotational formulation is applied within the local rotating axis system $\mathbf{T}_0$ which is indicated in Figure 2.1. The advantage

of such a formulation is that the stiffness matrix for the linear material behaviour remains valid since the small displacements are defined in a local coordinate system connected to each beam element. As such, geometrically large deflections are allowed because the local systems rotate along with the local beam element. Due to the deflection of the previous element a new local rigid body axis system is defined in which the new elastic deformations are determined.

The corotational formulation is visually summarised in Figure 2.2. For an unambiguous formulation of the framework, the sequence if transformations starts in a fixed axis frame. Next, the rotational transformation is performed. Within the rotated coordinates of the rigid rotor blade, the deformed blade shape is described by means of the corotational formulation. Following the symbols in Figure 2.2, the axis frames are presented using the notation **T**and the rotational transformations with $\boldsymbol{\mathcal{R}}$. This matrix is described in [De Breuker, 2011] and is determined as follows:

$$\boldsymbol{\mathcal{R}} = \sum_{k=0}^{\infty} \frac{\overline{\boldsymbol{\theta}}^k}{k!} = exp\left(\boldsymbol{\theta}\right), \tag{2.2}$$

where $\overline{\boldsymbol{\theta}}$ is the skew-symmetric representation of the pseudo-vector $\boldsymbol{\theta} = \{\theta_x, \theta_y, \theta_z\}^t$.

The axis frame defined as the body axis fixed frame, $\mathbf{T}_b$, can be identified with a non-rotating system attached to the rotor hub. The rotated blade system is defined using the initial orientation frame, $\mathbf{T}_0$, and indicates the rotated or azimuthal position of the undeformed blade. In such a way the blade azimuth can be taken into account. Next, the actual corotational formulation is used: the rigid element frame, $\mathbf{T}_r$, is based on the rigid rotation of the element considered, or the initial orientation frame if the first element is considered, and is expressed with respect to the body axis frame. Finally, with respect to the rigid element frame, the beam node orientations are calculated. Each beam node has its own triad, $\mathbf{t}_i$, indicating the cross-sectional orientation at each node, which means that the local deformations of both nodes are determined and the beam strains can be calculated.

Now that the axis frames are defined, the rotation transformations can be clarified. The $\boldsymbol{\mathcal{R}}_0$ indicates the rotation between the body-fixed frame and the initial, undeformed beam orientation. Then, the transformation from the rotating axis frame $\mathbf{T}_0$ to the rigid element frame $\mathbf{T}_r$ is accomplished using $\boldsymbol{\mathcal{R}}_r$. For the relation between the local triads and the initial beam orientation frame two transformations can be defined: $\boldsymbol{\mathcal{R}}_1^g$ from initial to node 1, or $\boldsymbol{\mathcal{R}}_2^g$ from initial to node 2. $\boldsymbol{\mathcal{R}}^g$ is expressed in $\mathbf{T}_0$ and $\boldsymbol{\mathcal{R}}_l$ is expressed in $\mathbf{T}_r$. Finally, the local element transformations involve the relations between the rigid element axis frame and the nodal triads that represent the cross-sectional orientation: $\boldsymbol{\mathcal{R}}_1^l$ from rigid frame to node 1 and $\boldsymbol{\mathcal{R}}_2^l$ from rigid frame to node 2.

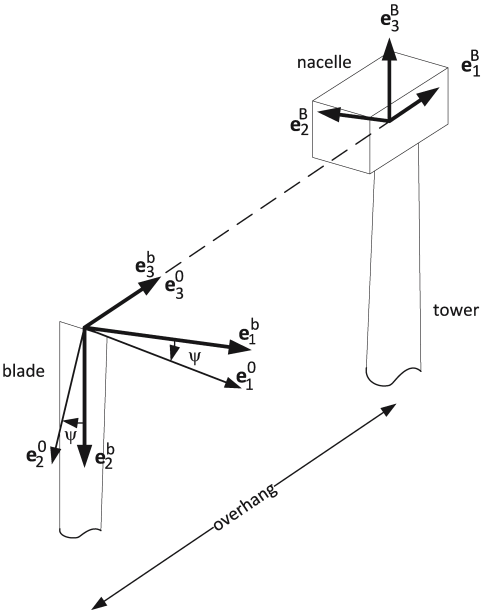

Figure 2.1: Coordinate systems at wind turbine blade root and tower top. The coordinate system $\mathbf{T}_b = [\mathbf{e}_1^b\ \mathbf{e}_2^b\ \mathbf{e}_3^b]$ is defined as non-rotating blade root system, while $\mathbf{T}_0 = [\mathbf{e}_1^0\ \mathbf{e}_2^0\ \mathbf{e}_3^0]$ defines the rotating system. The coordinate system $\mathbf{T}_B = [\mathbf{e}_1^B\ \mathbf{e}_2^B\ \mathbf{e}_3^B]$ is defined at the tower top. In the latter frame the undisturbed wind velocity is defined in $\mathbf{e}_1^B$ direction.

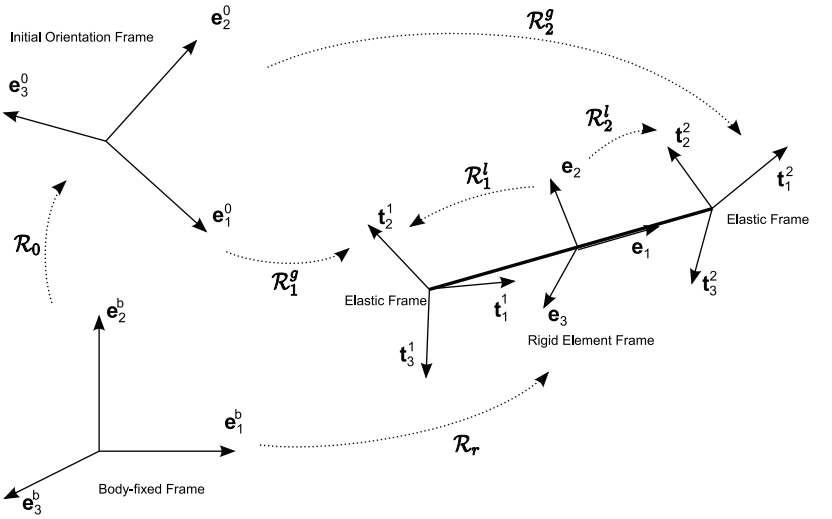

Figure 2.2: Corotating reference frame: review of co-ordinate systems used in [De Breuker, 2011]. The corotational approach is applied within the rotating coordinate system $\mathbf{T}_0$; The orientation of the corotational framework is indicated in Figure 2.1 in which the reference frame orientations of $\mathbf{T}_b$ and $\mathbf{T}_0$ are indicated.

2.2 STRUCTURAL MODELLING

The state-of-the-art wind turbine blades are manufactured using sandwich laminates for the leading and trailing edge parts of the blades as well as the front and rear spar. The spar caps are pure laminates to resist the highest compressive and tensile stresses. The blade cross-section consists of three cells: a narrow box beam with spar caps and to the left and right of the spars the cells that resist torsional deformation. For large wind turbines in the 20MW region, sometimes one adds an extra spar at approximately 70% of the chord to prevent skin buckling. In this work, two novel structural configurations are introduced:

- application of sandwich composite to the spar caps rather than solid spar caps;
- a stiffened skin by means of longitudinal stiffeners supported by ribs.

To analyse the different structural configurations, the following structural concepts are proposed that will be used to determine the internal loads and strains due to the external loads acting on the blade.

STRESS AND STRAIN FORMULATION FOR SANDWICH LAMINATES

The state-of-the-art wind turbine blades consist mainly of sandwich laminates. For the sake of an optimal calculation effort for sandwich laminates, a simplified structural model is applied: the stresses are carried by the facing sheets and the core is added to improve bending stiffness and face sheet buckling behaviour. This has some consequences for the **ABD** matrix and the lamination parameters for such laminates, which will be focused on later in this chapter. The **ABD** matrix is a key variable for the design of composite laminates. For a pure fibre laminate, this matrix couples the stress resultants acting in a cross-section to the local strains as follows:

$$\begin{pmatrix} N_x \\ N_y \\ N_{xy} \\ M_x \\ M_y \\ M_{xy} \end{pmatrix} = \begin{pmatrix} \mathbf{A} & \mathbf{B} \\ \mathbf{B} & \mathbf{D} \end{pmatrix} \begin{pmatrix} \epsilon_x \\ \epsilon_y \\ \gamma_{xy} \\ \kappa_x \\ \kappa_y \\ \kappa_{xy} \end{pmatrix}, \tag{2.3}$$

where the left-hand side represents the stress resultants. The forces N_x and N_y are the forces per unit length in the longitudinal, the lateral direction and the force N_{xy} is the in-plane shear force. The moments M_x and M_y represent bending about the x-axis and the y-axis respectively, while the moment M_{xy}

expresses a moment perpendicular to the xy-plane. The right-hand side shows, essentially, a multiplication of a stiffness matrix or, **ABD** matrix, with a strain vector consisting of extensional strains, shear strains, and curvature strains. The **A** matrix represents the in-plane stiffness and the **D** matrix represents the out-of-plane stiffness properties. The **B** is referred to as a coupling matrix because it couples extensional behaviour to out-of-plane behaviour. The latter becomes clear when one realizes that the strain vector contains 3 extension strains ϵ_x, ϵ_y, and ϵ_{xy} and 3 curvatures κ_x, κ_y, and κ_{xy}. An extensional stress resultant could cause a curvature because of non-zero terms in the **B** matrix. In Figure 2.3, the stress resultants are summarised. Note that the out-of-plane shear resultants V_x and V_y are omitted in case of plane stress and the twisting moments are defined as $M_{yx} = M_{xy}$, which is the case for laminate theory.

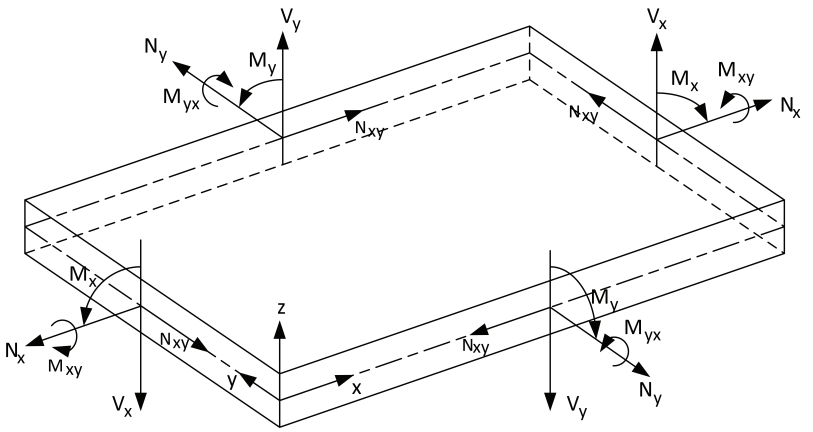

Figure 2.3: General sign convention of stress resultants for orthotropic shells. In the case of laminate theory the plane stress condition is assumed. Source: [Carreira, 2009]

Determining the **ABD** matrix for sandwich laminates requires a slightly different approach, however, the terms for pure laminates are included as well for the facing sheets. For the pure laminates the following elements determine the **A**, **B**, and the **D** matrices:

- the basic constitutive relations $\boldsymbol{\sigma}_{12} = \mathbf{Q}\,\boldsymbol{\epsilon}_{12}$ in the principal direction for each layer. The matrix **Q** include the constitutive relations that relate the internal stresses $\boldsymbol{\sigma}$ to the strains $\boldsymbol{\epsilon}$;

- the transformation matrix $\mathbf{T}_k$ to transform the k^{th} layer to the local axis system of a the local fibres over a rotation angle θ_k,

- the thickness h_k of the k^{th} layer and the total laminate thickness t and,

- the transformed constitutive relation for the k^{th} layer after rotation performed by the matrix $\mathbf{T}_k$, which is written as $\boldsymbol{\sigma}_{xy} = \overline{\mathbf{Q}}_k \, \boldsymbol{\epsilon}_{xy}$.

With this information, the **A**, **B** and **D** matrices of a pure laminate are determined as follows:

$$\begin{aligned} \mathbf{A} &= \sum_{k=1}^{n} \overline{\mathbf{Q}}_k \left(h_k - h_{k-1}\right), \\ \mathbf{B} &= \frac{1}{2} \sum_{k=1}^{n} \overline{\mathbf{Q}}_k \left(h_k^2 - h_{k-1}^2\right), \\ \mathbf{D} &= \frac{1}{3} \sum_{k=1}^{n} \overline{\mathbf{Q}}_k \left(h_k^3 - h_{k-1}^3\right). \end{aligned} \tag{2.4}$$

In this thesis, only symmetric laminates are considered, which means that the coupling matrix $\mathbf{B} = \mathbf{0}$.

The classical lamination theory is part of a conceptual model for sandwich laminates assuming that the faces are symmetric with respect to the mid plane of the laminate, see [Hollaway, 1994], for which the **A** and the **D** matrices transform into:

$$\begin{aligned} \mathbf{A} &= 2\mathbf{A}_f \\ \mathbf{D} &= 2\mathbf{D}_f + \frac{1}{2}\mathbf{A}_f \left({t_f}^2 + {t_c}^2\right) \end{aligned} \tag{2.5}$$

In this model, it is assumed that the loads are carried by the facing sheets of the sandwich structure and the core is only included to reinforce the out-of-plane stiffness to improve, for instance, the buckling behaviour. Using this sandwich laminate conceptual model for symmetric laminates, defining balanced and unbalanced laminates is done in the same manner as for pure fibre laminates because the facing sheets of the sandwich have an equal thickness and equal lay-up. The core does not contribute to the lay-up of the sandwich, which is clearly seen in the in-plane stiffness matrix **A** in Equation 2.5.

Lamination Parameters

Lamination parameters are a compact representation of the stacking sequence. The representation of the mechanical behaviour of a laminate by decomposing this behaviour in a material dependent part and a stacking sequence part is carried out in, amongst others, [Tsai and Hahn, 1980]. This compact representation of stacking sequence is suitable for optimisation purposes since it reduces calculation effort in comparison with the **ABD** representation of laminates. Therefore

the design variables of the optimisations within this research are expressed in lamination parameters, which are expressed as follows:

$$\begin{aligned}
(V_{1\mathbf{A}}, V_{2\mathbf{A}}, V_{3\mathbf{A}}, V_{4\mathbf{A}}) &= \frac{1}{h}\int_{-h/2}^{h/2} (\cos 2\theta, \sin 2\theta, \cos 4\theta, \sin 4\theta)\, dz, \\
(V_{1\mathbf{B}}, V_{2\mathbf{B}}, V_{3\mathbf{B}}, V_{4\mathbf{B}}) &= \frac{4}{h^2}\int_{-h/2}^{h/2} z\,(\cos 2\theta, \sin 2\theta, \cos 4\theta, \sin 4\theta)\, dz, \\
(V_{1\mathbf{D}}, V_{2\mathbf{D}}, V_{3\mathbf{D}}, V_{4\mathbf{D}}) &= \frac{12}{h^3}\int_{-h/2}^{h/2} z^2\,(\cos 2\theta, \sin 2\theta, \cos 4\theta, \sin 4\theta)\, dz. \quad (2.6)
\end{aligned}$$

The lamination parameters can be related to the **ABD** matrix. Using material invariant matrices $\mathbf{\Gamma}$ and the laminate thickness the **ABD** matrices are reconstructed according to [Tsai and Pagano, 1968]:

$$\begin{aligned}
\mathbf{A} &= h\left(\mathbf{\Gamma}_0 + \mathbf{\Gamma}_1 V_{1\mathbf{A}} + \mathbf{\Gamma}_2 V_{2\mathbf{A}} + \mathbf{\Gamma}_3 V_{3\mathbf{A}} + \mathbf{\Gamma}_4 V_{4\mathbf{A}}\right), \\
\mathbf{B} &= \frac{h^2}{4}\left(\mathbf{\Gamma}_1 V_{1\mathbf{B}} + \mathbf{\Gamma}_2 V_{2\mathbf{B}} + \mathbf{\Gamma}_3 V_{3\mathbf{B}} + \mathbf{\Gamma}_4 V_{4\mathbf{B}}\right), \\
\mathbf{D} &= \frac{h^3}{12}\left(\mathbf{\Gamma}_0 + \mathbf{\Gamma}_1 V_{1\mathbf{D}} + \mathbf{\Gamma}_2 V_{2\mathbf{D}} + \mathbf{\Gamma}_3 V_{3\mathbf{D}} + \mathbf{\Gamma}_4 V_{4\mathbf{D}}\right). \quad (2.7)
\end{aligned}$$

The material invariant matrices $\mathbf{\Gamma}_i$ are functions of the material invariants U_i. The material invariants are only functions of the material properties but do not vary with the fibre angles. Therefore, U_i is a function of the stiffness matrix $\mathbf{Q}$ from the constitutive relation:

$$\begin{aligned}
U_1 &= \left(3Q_{11} + 3Q_{22} + 2Q_{12} + 4Q_{66}\right)/8 \\
U_2 &= \left(Q_{11} - Q_{22}/2\right) \\
U_3 &= \left(Q_{11} + Q_{22} - 2Q_{12} - 4Q_{66}\right)/8 \\
U_4 &= \left(Q_{11} + Q_{22} - 6Q_{12} - 4Q_{66}\right)/8 \\
U_5 &= \left(Q_{11} + Q_{22} - 2Q_{12} + 4Q_{66}\right)/8 \quad (2.8)
\end{aligned}$$

For the sake of differentiating between balanced and unbalanced laminates, it is necessary to show the material invariant matrices. The matrices are constructed as follows:

$$\mathbf{\Gamma}_0 = \begin{pmatrix} U_1 & U_4 & 0 \\ U_4 & U_1 & 0 \\ 0 & 0 & U_5 \end{pmatrix}, \quad \mathbf{\Gamma}_1 = \begin{pmatrix} U_2 & 0 & 0 \\ 0 & -U_2 & 0 \\ 0 & 0 & 0 \end{pmatrix}, \quad \mathbf{\Gamma}_2 = \begin{pmatrix} 0 & 0 & U_2/2 \\ 0 & 0 & U_2/2 \\ U_2/2 & U_2/2 & 0 \end{pmatrix},$$

$$\mathbf{\Gamma}_3 = \begin{pmatrix} U_3 & -U_3 & 0 \\ -U_3 & U_3 & 0 \\ 0 & 0 & U_3 \end{pmatrix}, \quad \mathbf{\Gamma}_4 = \begin{pmatrix} 0 & 0 & U_3 \\ 0 & 0 & -U_3 \\ U_3 & -U_3 & 0 \end{pmatrix}. \tag{2.9}$$

For the case of a symmetric laminate, the **B** matrix vanishes and eight lamination parameters remain. For the case of balanced laminates there only remain four lamination parameters since the material invariant matrices $\mathbf{\Gamma}_2$ and $\mathbf{\Gamma}_4$, the shear-tension coupling, vanish. Using lamination parameters for optimisation causes some problems considering the feasibility of the laminate. A drawback of lamination parameters is that no set of closed-form expression exists that fully describe the feasibility region. This also has been pointed out in [Dillinger, 2014]. In [Werter, 2017], the necessary feasibility constraints are mentioned. These constraints are used in this work as well, especially for the optimisation procedure.

For sandwich structures, the lamination parameters can be used as well using the **ABD** properties from Equation 2.5. In that case, lamination parameters are coupled to the faces assuming that the upper and lower faces are equal. It is possible to decouple the upper and the lower face of the sandwich laminate by designating different sets of lamination parameters but this increases the computational effort significantly. Furthermore, one should verify whether the sandwich laminate remains symmetric. The thickness of the sandwich core is not taken into account in the lamination parameters but is included later on in the **ABD** matrix. This gives us the possibility to use the eight lamination parameters for a symmetric laminate and have additional design variables for laminate thickness, namely the face and the core. Defining a sandwich laminate in this manner for optimisation purposes is convenient since the number of design variables is limited. For balanced sandwich laminates, the 4 lamination parameters together with 1 face thickness parameter and 1 core thickness parameters result in 6 design variables. The unbalanced laminate gives a total of 10 design variables: 8 lamination parameters, 1 for the facing sheet thickness and 1 for the core thickness.

Cross-sectional modelling

A three dimensional representation of the blade can be transformed to a one dimensional Timoshenko beam element using a cross-sectional reduction model that preserves the strain energy and the orthotropic behaviour of laminates. A detailed cross-section at an arbitrary station across the wind turbine blade structural design is defined in 8 laminates, see Figure 2.4:

- the suction- and pressure side leading edge skin, sections 12 and 78;
- the suction side spar cap, section 23;
- the pressure side spar cap, section 67;

- the suction- and pressure side trailing edge skin, sections 34 and 56;
- the shear webs, sections 27 and 36.

For each laminate within the cross-section, the lamination parameters as well as the **ABD** matrices are determined for the cross-sectional modeller that converts this information to 1-dimensional element cross-sectional property tensor **C** for the blade segment considered. The **C** matrix is part of the relation where integral loadings and internal displacements are related as follows:

$$\begin{pmatrix} F_1 \\ F_2 \\ F_3 \\ M_1 \\ M_2 \\ M_3 \end{pmatrix} = \begin{pmatrix} EA & 0 & 0 & 0 & C_{15} & C_{16} \\ 0 & GA_2 & C_{23} & C_{24} & 0 & 0 \\ 0 & C_{32} & GA_3 & C_{34} & 0 & 0 \\ 0 & C_{42} & C_{43} & GJ & 0 & 0 \\ C_{51} & 0 & 0 & 0 & EI_2 & C_{56} \\ C_{61} & 0 & 0 & 0 & C_{65} & EI_3 \end{pmatrix} \begin{pmatrix} \epsilon_{11} \\ \epsilon_{12} \\ \epsilon_{13} \\ \kappa_1 \\ \kappa_2 \\ \kappa_3 \end{pmatrix} \tag{2.10}$$

In this expression, the displacements, ϵ_{ij} and curvatures, κ_i in the cross-section, for instance, an airfoil shape, are related to the stress resultants, F_i and M_i. Furthermore, the cross-sectional tensor shows some non-zero terms C_{ij} that indicates the orthotropic behaviour of the composite laminates included, and clearly the shear deformation is present as well, as indicated by the terms GA_i. In Equation 2.10 the balanced laminates case is represented, while for unbalanced laminates the cross-sectional tensor does not contain any zero elements. For completeness, it is noted that for a full isotropic material only the main diagonal contains non-zero terms, assuming that the inertia properties are defined with respect to the cross-sectional principal axes.

The lamination parameters are not the only manner to feed input for the cross-sectional modeller but are essential for the optimisation procedure performed for the optimal structural layout. In addition, the lamination parameters are necessary for the calculation of the **ABD** matrices of each blade segment. These matrices are functions of the rotor spanwise and the chordwise position, and *are* the necessary inputs for the cross-sectional modeller. The **ABD** properties are calculated using the lamination parameters of the pure laminates, or for the sandwich structures, the lamination parameters of the pure laminate faces together with the core thicknesses. Amongst others, the Equations 2.6 and 2.9 are required to obtain this property information. Within the cross-sectional modeller, the orthotropic properties of the blade segments are preserved and expressed in the cross-sectional tensor represented as a 1-dimensional beam segment.

The blade stiffness distribution is plotted along the blade span for the 5MW blade for both the reference blade as defined by NREL and the present model, referred to as PROTEUS, to validate the blade as defined in the structural model. Figure 2.5 shows the flap-wise and edgewise stiffness distribution comparison.

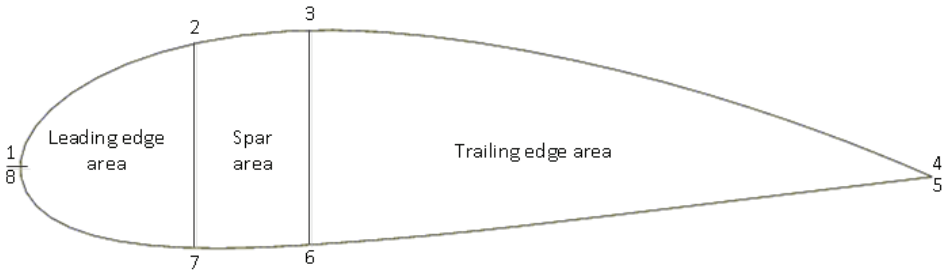

Figure 2.4: Composite areas for cross-sectional modelling

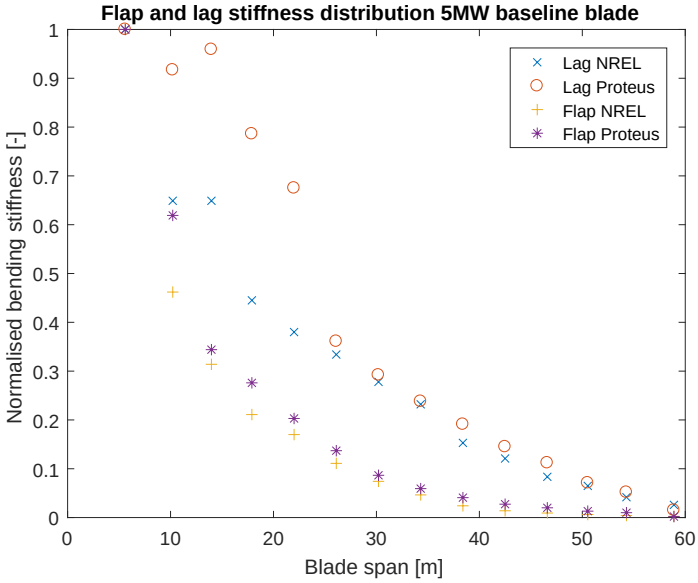

Figure 2.5: Comparison between NREL reference blade stiffness and stiffness property distribution resulting from the advanced cross-sectional modeller. Note that the stiffness distribution is an optimised results for thickness only. The lay-up is quasi isotropic.

As can be seen, the flap bending stiffness resulting from the cross-sectional modeller is quite similar to the reference flap stiffness distribution as calculated in [Jonkman et al., 2009], the deviation from the NREL result is +3%. The edge stiffness and the torsional stiffness distribution, however, deviate more from the reference blade stiffness results. The torsional stiffness data is shown in Figure 2.6:

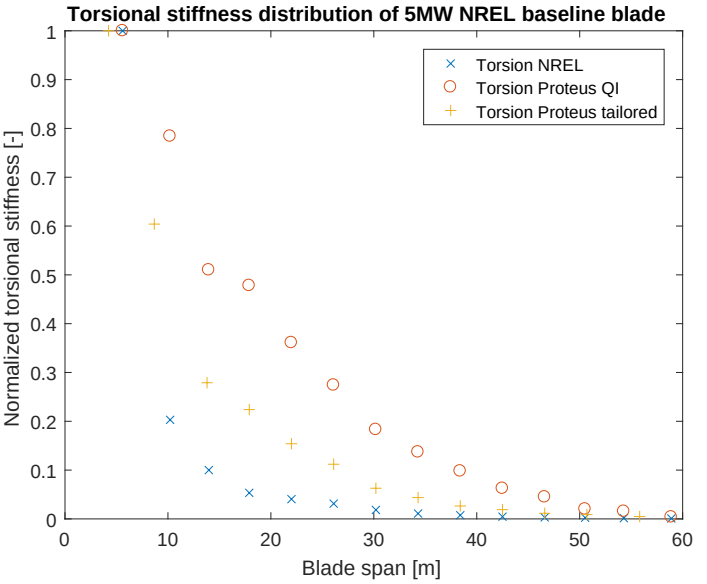

Figure 2.6: Comparison between NREL reference blade torsional stiffness ans stiffness property distribution resulting from the advanced cross-sectional modeller. Note that the stiffness distribution is an optimised results for thickness only. The lay-up is quasi isotropic.

The edgewise bending stiffness shows good agreement for the outer blade section; for the inner blade section the stiffnesses show relative high value, this is caused by the transformation of the circular cross-section and the airfoil shapes. This results in a +11% deviation from the NREL results, which is significant. The torsional stiffness distribution has an overall higher value than the reference blade which could be the result of assuming a quasi-isotropic lay-up of the blade, and a higher thickness distribution, a deviation of +19% is observed. Including the lay-up as an extra variable as a function of the blade span gives a more reliable distribution of the torsional stiffness, which is also shown in the deviation percentage: the difference is reduced to 8%. It should be noted that [Jonkman et al., 2009] points out that the torsional stiffness has been generated in a less accurate manner. Since the origin of the NREL cross-sectional properties is not clear, and the cross-sectional properties used in PROTEUS follow from a well-validated cross-sectional modeller, see [Ferede, 2016], it is assumed that the PROTEUS cross-sectional

results are adequate for optimisation purposes.

Buckling

The adopted buckling model is taken from [Werter, 2017], previously used by [Dillinger, 2014], from which it is concluded that the wing or blade should at least exist of spars and ribs. This is the case for large wind turbine blades, however, the curvature of the cross-sectional airfoil shape is not included within the proposed model. Furthermore, ribs are not yet used in wind turbine blades which means that buckling panels become fairly large, which has its influence on the buckling behaviour. Still, the proposed model can be used, which is explained next. Since the proposed model is a theoretical model, it can be compared to a study carried out by [Gaudern and Symons, 2010]. In this study, such a theoretical model has been compared to a finite element study for wind turbines where the curvature of the cross-sectional airfoil shape has been taken into account and also the simply supported boundary condition results were compared to the clamped results. From this work, it is concluded that simply supported boundary conditions are conservative, which means that the buckling load is estimated to be lower than the actual value caused by boundary conditions between simply supported and clamped. Furthermore, it is mentioned that curvature causes the compression load to be higher than for a flat plate. To clarify this, the work of [Gaudern and Symons, 2010] is used as well. The following equations are used for the calculation of theoretical buckling loads of cylindrical panels:

$$N_x = -\frac{1}{\lambda^2}\left[\left(\frac{\mathbf{H}_{12}^2}{\mathbf{H}_{11}}\right) + \mathbf{H}_{22} + N_y\eta^2\right], \tag{2.11}$$

where:

$$\begin{aligned}
\mathbf{H}_{11} &= \lambda^4\mathbf{S}_{22} + 2\left(\mathbf{S}_{12} + \frac{1}{2}\mathbf{S}_{33}\right)\lambda^2\eta^2 + \mathbf{S}_{11}\eta^4,\\
\mathbf{H}_{12} &= \frac{\lambda^2}{R},\\
\mathbf{H}_{22} &= \lambda^4\mathbf{D}_{11} + 2\left(\mathbf{D}_{12} + 2\mathbf{D}_{33}\right)\lambda^2\eta^2 + \mathbf{D}_{22}\eta^4,\\
\mathbf{S} &= \mathbf{A}^{-1}.
\end{aligned} \tag{2.12}$$

Where N_x and N_y are the compressive loadings in longitudinal and lateral direction respectively. Furthermore, the quantities λ and η indicate the number of half waves in longitudinal and lateral direction respectively. Lastly, $\mathbf{A}$ indicates the in-plane stiffness matrix, $\mathbf{D}$ is the out-of-plane stiffness matrix, and $\mathbf{S}$ is the inverse of the in-plane stiffness matrix resulting from the $\mathbf{ABD}$ matrix of a laminate. The Equations 2.11 and 2.12 are used to explain that for an increasing radius

of curvature R the buckling load decreases. This means that the critical buckling load is lower for a flat plate than for a cylindrical shell. Assuming flat panels for the leading edge and realising that they underestimate the actual buckling load for a curved panel, this assumption is conservative as well as imposing simply supported boundary conditions at the edges of the panels. As a consequence, skin thicknesses will be overestimated during, for instance, an optimisation procedure.

According to [Werter, 2017], the buckling panels should be rectangular and the stresses are assumed to be constant across the panels. The constant stress assumption is easily met because the buckling panels are smaller than or equal to the dimensions of composite panels as defined in Figure 2.4. To accomplish that for the blades considered during the research, it is assumed to give the buckling panels such dimensions that the blade thickness distribution of the baseline is approximated. Contrary to pure fibre laminate skins, ribs are not required for sandwich skins. Since sandwich skins are subject to local buckling as well and for valid data resulting from the adopted buckling model, the buckling panels are determined by placing artificial ribs at fixed distances. Using artificial ribs gives the possibility to control the buckling modes of the sandwich skin and define appropriate dimensions of the buckling panels suitable for the model. Therefore, the artificial ribs do not influence the total blade mass and simply supported boundary conditions are imposed. Note that for pure fibre laminate skins, the rib mass *must* be taken into account considering the total blade mass.

Since the panels are already limited in chordwise direction by means of the spar webs, the panel dimensions are defined. It should be noted that the leading edge part of the blade is curved and for the structural layout of the blade, this is a curved buckling panel bounded by two ribs and the spar and the leading edge. The curvature of this cross-sectional part can be approximated by assuming a cylindrical curvature but is modelled as a flat buckling panel to be conservative. Considering the simply supported boundary conditions applied, the artificial ribs in spanwise direction are only placed in such a way that buckling behaviour of the baseline is approximated, based on [Ferede, 2016]. A quick sensitivity study was performed to check the model. The length of the buckling panels was chosen to be 1, 2, and 4 meters. Starting from the 2 meters as present in the simulations, a decrease in blade mass was observed for the 1-meter panels, while for the 4-meter panels an increase in blade mass was observed. In addition, the panel length variations showed appropriate blade mass variations. This means, that the buckling model behaves as expected. To be conservative for the optimised blade mass, the rib masses are included in the total blade mass. From the above, it can be concluded that the buckling behaviour is modelled in a conservative manner.

The buckling calculation within this research is, just like the cross-sectional modeller, based on strain energy from which the stiffness matrices are derived that are required for the buckling analysis. The governing equation is formulated as an eigenvalue problem from which the inverse buckling value r is calculated for

each panel. A value $r \leq 1$ means a buckling free panel:

$$(\mathbf{K}_g - r\mathbf{K})\,\mathbf{a} = \mathbf{0}, \tag{2.13}$$

where $\mathbf{K}_g$ is the geometric stiffness matrix, $\mathbf{K}$ the actual stiffness matrix, and $\mathbf{a}$ contains the coefficients from the assumed displacement functions. The geometric stiffness matrix $\mathbf{K}_g$ is containing the information of the local buckling element loading:

$$\mathbf{K}_g = -N_x\mathbf{K}^{xx} - N_y\mathbf{K}^{yy} - N_{xy}\mathbf{K}^{xy}, \tag{2.14}$$

where is assumed that the local loadings are constant across the buckling panel. The actual stiffness matrix $\mathbf{K}$ is given as:

$$\mathbf{K} = \sum_{i=1,2,6}\sum_{i=1,2,6} D_{ij}\mathbf{K}^{ij}, \tag{2.15}$$

where D_{ij} are the out-of-plane components from the local **ABD** matrix and the $\mathbf{K}^{ij}$ terms are based on the integral over a product of the second derivatives of the assumed displacement functions across the buckling element. The two-dimensional assumed displacement functions are written as:

$$w(\xi,\eta) = \sum_p \sum_q a_{pq}\phi_p\left(\xi\right)\phi_q\left(\eta\right), \tag{2.16}$$

where the the ϕ represent bubble functions expressed in two perpendicular, non-dimensional directions ξ and η and a_{pq} represents the coefficients of the polynomials. Since the displacement function is defined, the term $\mathbf{K}^{ij}$ is calculated as, for example:

$$K_{pq}^{11} = \iint_A \frac{\partial^2\phi_p}{\partial x^2}\frac{\partial^2\phi_q}{\partial x^2}dA. \tag{2.17}$$

The geometrical stiffness matrix terms $\mathbf{K}^{xx}$, $\mathbf{K}^{yy}$, and $\mathbf{K}^{xy}$ are based on the integral over the product of the first derivative of the product of the aforementioned displacements functions, which gives:

$$K_{pq}^{xx} = \iint_A \frac{\partial\phi_p}{\partial x}\frac{\partial\phi_q}{\partial x}dA, \tag{2.18}$$

$$K_{pq}^{yy} = \iint_A \frac{\partial\phi_p}{\partial y}\frac{\partial\phi_q}{\partial y}dA, \tag{2.19}$$

and

$$K_{pq}^{xy} = \iint_A \frac{\partial \phi_p}{\partial x} \frac{\partial \phi_q}{\partial y} dA, \tag{2.20}$$

where A represents the buckling panel area and x and y the panel coordinates.

Geometrically nonlinear beam model

The structural model is based on the model from [De Breuker, 2011]; an overview of the model will be given in this section. To account for geometrically nonlinear solutions, linear Timoshenko beam elements are embedded in a co-rotational framework as shown in figure 2.2.

In addition, the cross-section is constant over the element length. The latter means that the blade should should be discretised in sufficient spanwise elements to account for the cross-sectional variation in spanwise direction. The beam strain energy of the local Timoshenko beam element is described as:

$$U = \frac{L_0}{2} \int_0^1 \boldsymbol{\epsilon}^T \mathbf{C} \boldsymbol{\epsilon} \, d\xi, \tag{2.21}$$

where U is the strain energy, L_0 the local, undeformed element length, $\boldsymbol{\epsilon}$ the strain vector containing the local strains and the local curvatures, $\mathbf{C}$ the cross-sectional tensor from equation 2.10, and ξ the nondimensional element length normalised by L_0.

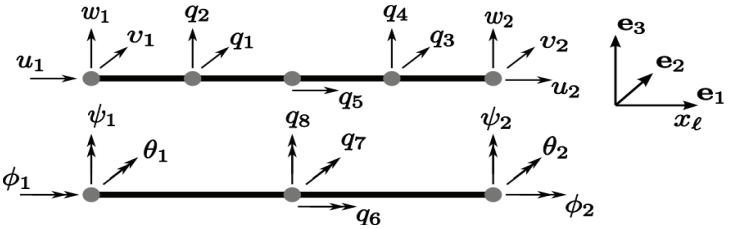

Figure 2.7: Timoshenko beam element. Source: [De Breuker, 2011].

Since the strains and curvatures are expressed in terms of beam displacements and rotations and their first derivatives with respect to the beam co-ordinate ξ, the relations with respect to the beam co-ordinates, with help of figure 2.7, are as follows:

$$
\begin{aligned}
u &= u_1(1-\xi) + u_2\xi + q_5\xi(1-\xi) \\
v &= v_1(1-\xi) + v_2\xi + q_1\xi(1-\xi) + q_3(1-\xi)(1/2-\xi) \\
w &= w_1(1-\xi) + w_2\xi + q_2\xi(1-\xi) + q_4(1-\xi)(1/2-\xi) \\
\phi &= \phi_1(1-\xi) + \phi_2\xi + q_6\xi(1-\xi) \\
\theta &= \theta_1(1-\xi) + \theta_2\xi + q_7\xi(1-\xi) \\
\psi &= \psi_1(1-xi) + \psi_2\xi + q_8\xi(1-\xi).
\end{aligned} \tag{2.22}
$$

The extra nodes were introduced to include anisotropic effects as well, such as bend-twist coupling of blades or wings. An other advantage of using extra nodes is that shear locking is avoided, [Crisfield, 1986]. Using the above definition of the beam degrees of freedom, the strain vector is set up following [Luo, 2008]:

$$
\boldsymbol{\epsilon} = \left(\frac{1}{l_0}u_\xi, -\psi + \frac{1}{l_0}v_\xi, \theta + \frac{1}{l_0}w_\xi, \frac{1}{l_0}\phi_\xi, -\frac{1}{l_0}\theta_\xi, \frac{1}{l_0}\psi_\xi \right)^T, \tag{2.23}
$$

where the subscript ξ indicates the first derivative with respect to the nondimensional beam co-ordinate ξ. The second derivative of the strain energy U with respect to the degrees of freedom $\mathbf{p}$ determines the beam stiffness matrix. A vector containing all local element degrees of freedom is defined as follows:

$$
\mathbf{p} = (u_1, v_1, w_1, \phi_1, \theta_1, \psi_1, u_2, v_2, w_2, \phi_2, \theta_2, \psi_2, q_1, q_2, q_3, q_4, q_5, q_6, q_7, q_8)^T. \tag{2.24}
$$

The information of only the end nodes is required in the aeroelastic analysis. As such, the static condensation method is used to reduce the degrees of freedom, [Guyan, 1965], to eliminate the internal nodes q_i. Splitting the vector $\mathbf{p}$ into $\mathbf{p}_i$ and $\mathbf{p}_l$ to indicate internal nodes and external nodes respectively, the partitioned equation is obtained:

$$
\left(\begin{array}{c|c} \mathbf{K}_{l,l} & \mathbf{K}_{l,i} \\ \hline \mathbf{K}_{i,l} & \mathbf{K}_{i,i} \end{array}\right) \begin{pmatrix} \mathbf{p}_l \\ \mathbf{p}_i \end{pmatrix} = \begin{pmatrix} \mathbf{f}_l \\ \mathbf{0} \end{pmatrix} \tag{2.25}
$$

The reduction is accomplished by solving the second equation for $\mathbf{p}_i$ and substituting in the first equation. The resulting equilibrium equation reads as:

$$
\mathbf{K}_l \mathbf{p}_l = \mathbf{f}_l, \tag{2.26}
$$

where:

$$
\mathbf{K}_l = \mathbf{K}_{l,l} - \mathbf{K}_{l,i}{\mathbf{K}_{i,i}}^{-1}\mathbf{K}_{i,l}, \tag{2.27}
$$

which is the reduced stiffness matrix of the Timoshenko beam element. Within the corotational formulation, the above beam analysis is defined in the rigid rotated coordinate frame, $\mathbf{T}_r$.

Inclusion of gravity

Large blades are subjected to significant variations in the gravity field, and as such, the weight distribution of the blade is required as well. The gravity force at each beam element is acting in the global coordinate system and must be transformed to the rotating axis system. This is done by using the transformation matrix $\boldsymbol{\mathcal{R}}_0$ from Equation 2.1 as $\mathbf{F}^0_{grav} = \boldsymbol{\mathcal{R}}_0 \mathbf{F}^b_{grav}$. In this manner, the orientation of the blade determines the amount of tangential and normal force distribution across the blade span originating from the gravitational field. The gravity forces are expressed in the rotating coordinate frame and the corotational formulation takes care of the influences of the gravitational components regarding the blade deformation. As a consequence, the internal stresses can be determined as well. It should be noted already that, especially when the blade is in the vertically upward position, gravity causes a situation that is not favourable for the case of local buckling: the gravitational components introduces a significant extra compressive component. Figure 2.8 shows the idea of this transformation.

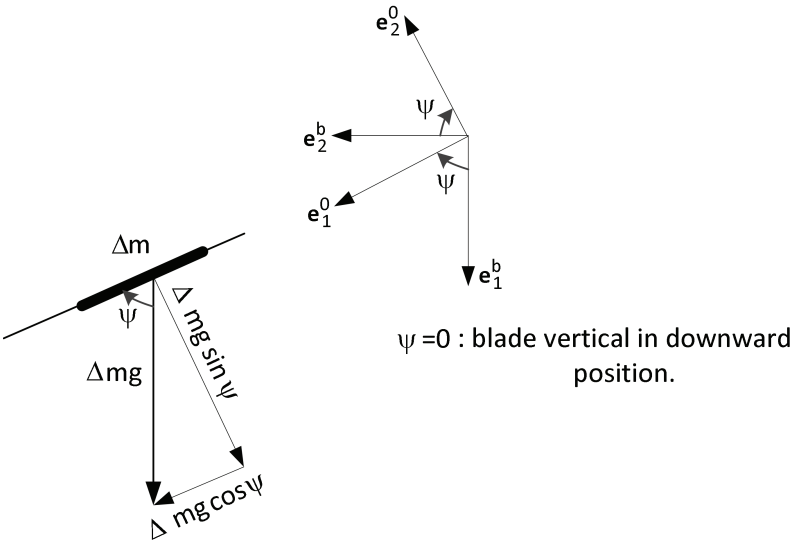

Figure 2.8: Inclusion of gravitational force in the rotating coordinate frame.

Within the hub-fixed framework, $\mathbf{T}_b$ in Figure 2.2, the gravity force is of constant value and is independent of the azimuth. However, for each rotor blade azimuth the gravity components within the local axes are dependent on the angle. Still,

the gravity force does not follow the deformation of the blade nor the azimuthal position. The deformation is calculated using the corotational formulation as follows. The gravity force is transformed to the beam nodes, and is expressed in the global axes first. Then, from the rigid axis frame, the forces are expressed in the local beam coordinates where, eventually, the structural deformation is calculated:

$$\mathbf{F}^{l}_{grav_i} = \frac{1}{2}\boldsymbol{\mathcal{R}}^{l}_{i}\boldsymbol{\mathcal{R}}_{r}\left(\boldsymbol{\mathcal{R}}^{l}{}_{i}\right)^{-1}\boldsymbol{\mathcal{R}}^{g}_{i}\boldsymbol{\mathcal{R}}_{0}\mathbf{F}^{b}_{grav} \tag{2.28}$$

Note that the gravity force $\mathbf{F}^{b}_{grav}$ acts in the midpoint of each beam element and is defined, and thus calculated, in the body fixed axis system $\mathbf{T}_b$.

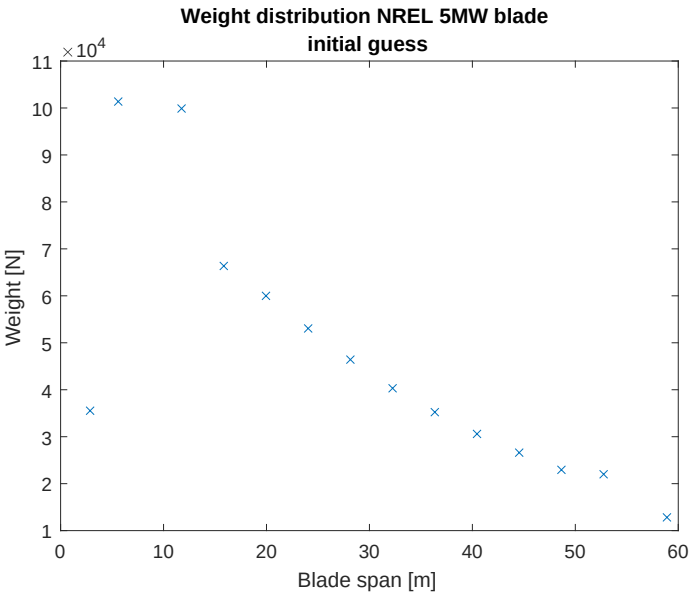

Figure 2.9: Inclusion of gravitational force in non-rotating coordinate frame, blade fixed at 90 degrees azimuth.

Figure 2.9 shows the weight as a function of the blade radius for a 5MW turbine blade. Next, the element gravity is transformed to the nodes and shows a cyclic variation as a function of the azimuth. In Figure 2.10 it is clear that the gravitational forces in the nodes show the variation that is expected in the local beam coordinate system and can be used within the structural analysis in the aeroelastic calculation.

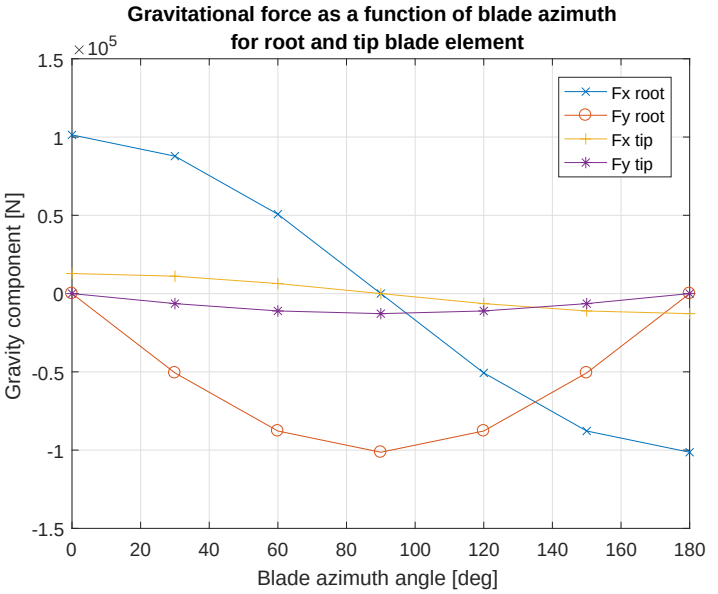

Figure 2.10: Inclusion of gravitational force in rotating coordinate frame, for a rotating blade at multiple blade stations.

Inclusion of centrifugal effect

To take the centrifugal stiffening effect into account, it is essential to include the centrifugal force $\mathbf{F}_c$. This is taken care of by evaluating the expression $\mathbf{F}_c = \Delta m \Omega^2 \mathbf{r}$ midst of each blade structural element, the location of the rigid element frame. The centrifugal force orientation is along the undeformed rotating blade axis, expressed in the initial orientation frame $\mathbf{T}_0$. These forces are applied to the structure as external forces. Figure 2.11 shows how the centrifugal force distribution is built in the rotational coordinate frame.

Within this frame the corotational formulation is used to determine the internal stresses due to the centrifugal force distribution by calculating the local displacements, and from the local stiffness matrix the stresses form this rotating effect are implemented as well. Using the corotational rotation matrices from Figure 2.2, half of the total element centrifugal force is moved to each of the beam nodes as follows:

$$\mathbf{F}^l_{ci} = \frac{1}{2} \boldsymbol{\mathcal{R}}^l_i \boldsymbol{\mathcal{R}}_r \left(\boldsymbol{\mathcal{R}}^l{}_i \right)^{-1} \boldsymbol{\mathcal{R}}^g_i \mathbf{F}^0_c \tag{2.29}$$

Note that the centrifugal force is calculated in the initial orientation frame $\mathbf{T}_0$ labelled as $\mathbf{F}^0_c$ acting halfway the beam element considered. Since the centrifugal

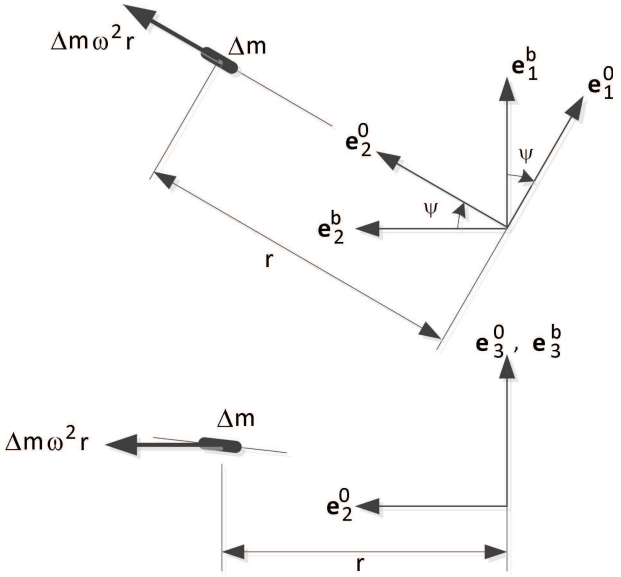

Figure 2.11: Inclusion of centrifugal force in rotating coordinate frame.

force is slightly dependent on the local radius this force follows the deformed elements in a negligible way.

Again, for the 5MW blade, the distribution of the centrifugal force is shown in Figure 2.12. Within the local beam coordinate system, it is expected that the centrifugal force remains constant with respect to the azimuthal position of the blade. It was found from simulations, that this centrifugal effect was indeed independent of the azimuth. Furthermore, the distribution of the force fits the order of magnitude of the linear velocities is 30 m/s and the element mass 4000 kg at midspan. The mass distribution decreases in the spanwise direction towards the blade tip; in combination with the increasing velocity towards the tip, a maximum in the centrifugal force gradient is expected which is shown in the graph as well. The centrifugal force distribution serves as an input for the stiffening effect due to the blade rotation.

2.3 Aerodynamic modelling

Quasi-steady inviscid flow modelling

The aerodynamic theory that is most used for aerodynamic wind turbine blade design is the blade element momentum theory (BEM). The BEM theory is a very fast method for finding the aerodynamic loads on the blade. Essentially, this

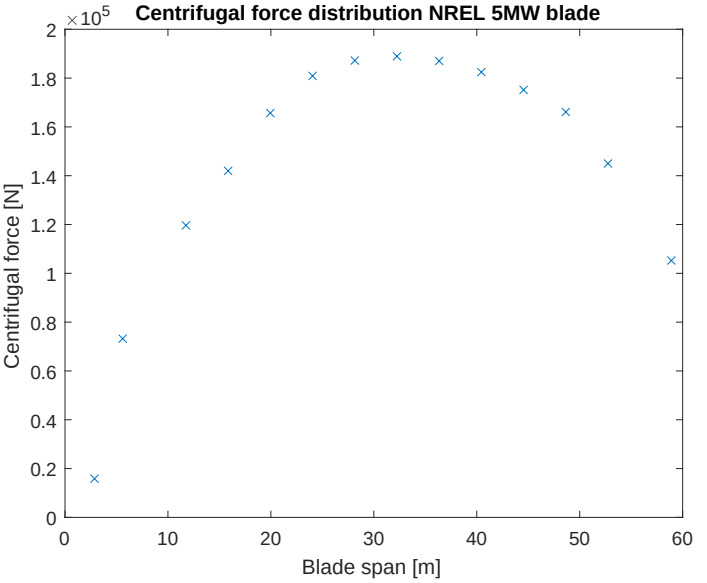

Figure 2.12: Inclusion of centrifugal force in local beam coordinate frame, produced by per blade segment.

theory is low fidelity considering the underlying physics. The BEM models used in codes as BLADED, FAST, and HAWC correct for the limited physical modelling using (semi)-empirical corrections for e.g. tip-loss and skewed wake. This upgrades the accuracy of such BEM models. Yet, because of the limited physics in BEM based models, higher fidelity aerodynamic models have been considered in this thesis. First, the higher order lifting line theory and unified lifting line theory, [van Holten, 1976] and [Guermond, 1990] respectively, were considered for the equal fidelity aerodynamic modelling. Especially the higher order lifting line theory was considered using the work of [van Bussel, 1992], where this theory has been applied on horizontal axis wind turbine rotor blades. The higher order lifting line theory inherently models phenomena as tip-loss and skewed wake and is of medium fidelity.

In this research however, a vortex panel method similar to [Amin et al., 2012], [Werter et al., 2017], or [van Garrel, 2003] was chosen, for the aerodynamics. Such a panel method is a proper method to model a three-dimensional aerodynamic loading, which is transferred to a line load distribution without losing the important aerodynamic properties. This is the same line of reasoning as using the cross-sectional modeller together with a 1-dimensional Timoshenko beam where the three-dimensional properties are preserved as well. Applying such a vortex panel method for the blade and the wake, the aeroelastic loads are calculated in a consistent way as far as fidelity is concerned. Still, the vortex model is used

together with the blade element concept: the induced velocities generated by the vortices are calculated for each aerodynamic element and where the initial velocity is corrected by the local induced velocities. The aerodynamics is of medium fidelity and takes more calculation effort because the wind turbine wake is strongly deformed. This strong wake deformation is the main reason for this increased calculation effort: the wake must be discretised into a number of straight vortex panels to obtain a satisfactory wake contribution. For now, the wake is assumed to be cylindrical but it is possible to include a wake expansion algorithm within the aerodynamic model. This will slow down the aerodynamic analysis but some smart coding techniques may reduce the computational time significantly. Furthermore, the axis systems of the aerodynamic model rotate along with the blade compared to the inertial reference in which the undisturbed wind velocity V_w is defined. A disadvantage is that the parasite drag force is not inherently included in vortex models. This needs to be repaired for realistic results, which is taken care of in this section.

For the aerodynamic load calculation, the inviscid Laplace flow field equation is introduced as:

$$\nabla^2 \phi = 0, \tag{2.30}$$

where ϕ is the perturbation velocity potential. A lift generating solution for this equation is the vortex filament, [Prandtl and Tietjens, 1957]. According to [Katz and Plotkin, 2001], the bound vorticity along the blade is calculated in the rotating blade reference frame using:

$$a_{ij}\Gamma_i = -\mathbf{V}_j \cdot \mathbf{n}_j, \tag{2.31}$$

where a_{ij} are the influence coefficients, $\mathbf{V}_j$ is the local velocity vector at the location considered, and ($\mathbf{n}_j$ is the unit normal at the panel considered. Equation 2.31 is referred to as the linearised flow tangency condition for a blade segment which means that the flow cannot penetrate the lift generating body. The bound vortex distribution across the blade is calculated by coupling the wake influence to the velocities at the blade control points. The velocities induced by the vortex filament are defined by the Biot-Savart equation, given by [Katz and Plotkin, 2001]:

$$d\mathbf{v}_d = \frac{\Gamma}{4\pi} \frac{d\mathbf{l} \times \mathbf{a}}{\|\mathbf{a}\|^3}, \tag{2.32}$$

where $\mathbf{a}$ is the vectorial distance between the vortex filament end points and the location where the induced velocity is calculated. Using Equation 2.32, the influence coefficients a_{ij} are calculated as follows:

$$a_{ij} = \sum_{k=1}^{N} \left[\int_{\mathbf{x}_{p,k}}^{\mathbf{x}_{p,k+1}} \frac{1}{4\pi} \frac{d\mathbf{l} \times \mathbf{a}_k}{\|\mathbf{a}_k\|^3} \right] \mathbf{n}_j. \tag{2.33}$$

In Equation 2.33 it is described how all vortex filaments, except filament j, influence the j^{th} vortex filament. As a consequence, the vortex filament distribution in the wake is required as well.

Discrete vortex modelling

The blade and the wake are built of quadrilateral vortex elements; the blade is both discretised in the spanwise and chordwise direction. The principle is shown in Figure 2.13.

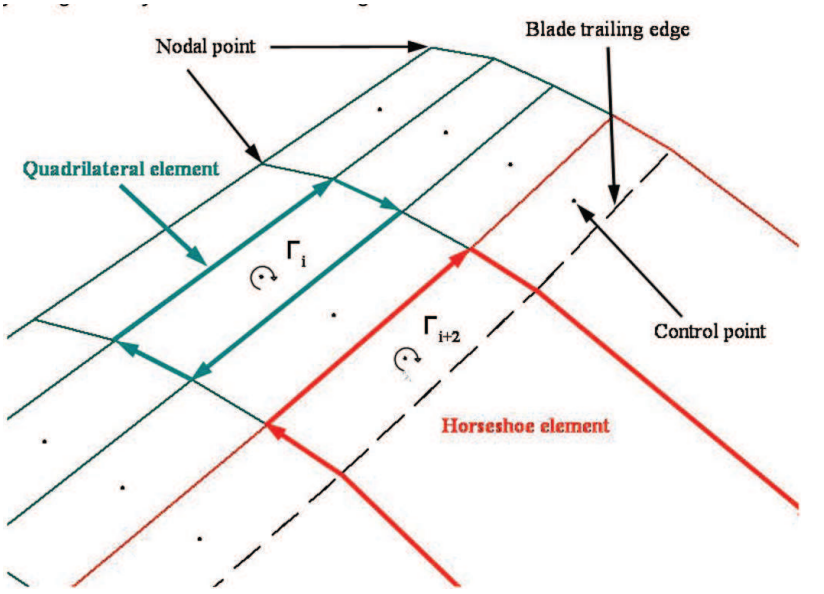

Figure 2.13: Thin airfoil modelled using vortex panels from [Burger and Hartfield, 2006].

At the blade trailing edge, the vorticity is forced to be zero because of the Kutta condition. This is accomplished by defining the circulation of the first vortex wake panel equal but opposite to that of the final bound surface panel in such a way that the circulation at the trailing edge location equals zero, [Katz and Plotkin, 2001]. For quasi-steady aerodynamic simulations this means that no shed vorticity is present in the wake, which is modelled as indicated in Figure 2.13. Since the aerodynamic panels are based on thin airfoil theory, adding camber to the model realizes the approximate correct aerodynamic behaviour. Critical for the vortex

strength of the individual panels is the wake shape and orientation. The wake is assumed to be cylindrical as shown in Figure 2.14 and the vortex panels are moving along with the main wind direction.

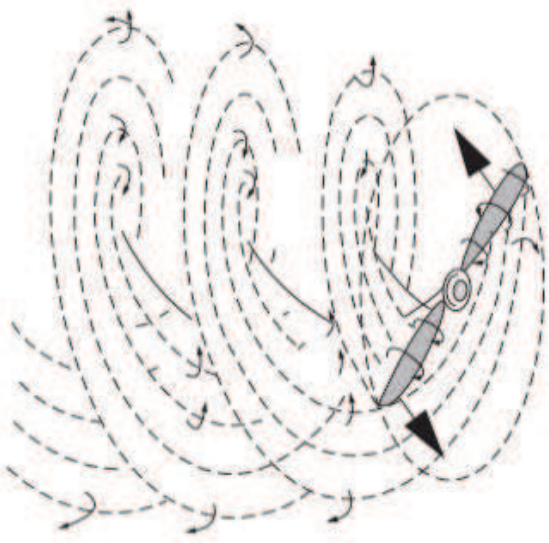

Figure 2.14: Expanded rotor wake vortex system. In this work however, it is assumed that the rotor wake does not expand. Source: http://machineryequipmentonline.com/hvac-machinery/wp-content/uploads

Since this wake is strongly deformed in comparison with fixed-wing wakes, it is even more important to apply a proper discretisation in the azimuthal direction and in the spanwise direction, provided that straight vortex lines are used in the model. For an arbitrary control point on the blade the influence coefficients of a complete vortex system, besides the panel at the control point considered, are calculated using Equation 2.33.

The difficulty with wind turbine wakes, however, arises from the 3-dimensional deformed shape. The wake is discretised in a finite number of quadrilateral wake panels with straight edges. For a cylindrical wake, vortex lines emanating from the trailing edge and can be expressed in cylindrical co-ordinates. Therefore, the nodes of the vortex panels in the wake can be described with the equation:

$$\mathbf{x}_{p,k} = \left[r_k \sin \Delta\Psi_k, r_k \cos \Delta\Psi_k, \frac{v_w \Omega}{\Delta\Psi_k} \right], \tag{2.34}$$

where r_k is the local blade radius, Ψ_k is the local blade azimuth, Ω is the blade angular rate, and v_w is the wind velocity. As can be seen from Figure 2.15, the

vortex panels move in the direction of the total velocity under the inflow angle ϕ with respect to the tangential axis. This angle is also indicated in Figure 2.14; it is assumed that the vortices emanate from the bound surface with the inflow angle across the blade span and maintain this angle, due to the prescribed cylindrical wake. For each of the blade elements, the inflow angle is calculated as:

$$\phi_i = \arctan \frac{\Omega r_i}{v_w}. \tag{2.35}$$

The orientation of the vortex panels behind the trailing edge and the inflow angle ϕ_i coincide, which shows the blade element implementation within the vortex panel method. A significant advantage is, since the wake is discretised by means of a finite number of straight vortex lines for the steady case, that is not necessary to model a new wake since the discretised wake is already suitable for an unsteady analysis. An unsteady analysis, however, is beyond the scope of the present PhD research.

It should be noted that the wake requires a force-free boundary condition, which is not the case for a cylindrical wake. In this research, it is assumed to be sufficient for the blade loads to use the simplified cylindrical wake approach.

Aerodynamic forces and moments

The forces on a blade are a direct effect of the local angle of attack at a blade element as indicated in Figure 2.15 from [Dumitrescu and Cardoş, 2001].

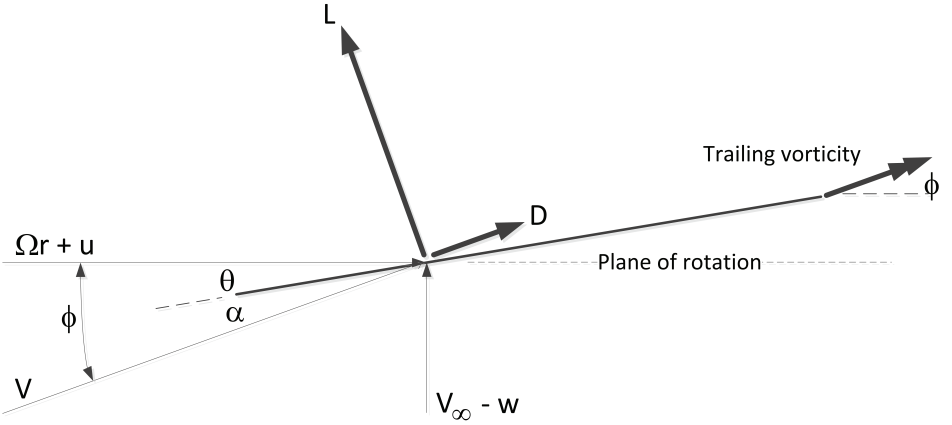

Figure 2.15: Velocities at a blade element presented in the plane of rotation

The velocities u and w are the velocities induced by the wake and all the bound vortex elements. The total velocity at the local control point determines the

vortex strength at the blade element considered because of the flow tangency condition. This approach implies that all elements do influence each other, which is not the case in the blade element momentum theory. From the blade bound vorticity distribution the lift force per segment is calculated by the Kutta-Joukowski relation:

$$\mathbf{L} = \rho \mathbf{V} \times \mathbf{\Gamma}, \tag{2.36}$$

where $\mathbf{\Gamma} = \Gamma \Delta \mathbf{l}$. From Equation 2.36 the aerodynamic moment is generated by the lift as follows:

$$\mathbf{M} = \Delta \mathbf{c} \times \mathbf{L}. \tag{2.37}$$

The velocity vector $\mathbf{V}$ is composed of the tangential and the local wind velocity, $(\Omega r, 0, V_\infty)$. Γ is designated the magnitude of the circulation, and $\Delta \mathbf{l}$ indicates the direction of the vortex line considered. The vector $\Delta \mathbf{c}$ in the moment relation indicates the distance between the quarter chord of the segment airfoil and the location of the beam element.

For a reliable estimate of the aerodynamic wind turbine power, an estimation of the aerodynamic drag should be included as well. Two types of drag are taken into account; the induced drag and the parasitic drag. The induced drag is calculated by carrying out the cross product between the induced velocity of the wake panels on the bound vortex panels and the local circulation vector as proposed by [Katz and Plotkin, 2001]. The induced velocity at the control points is calculated using the aerodynamic wake panels that are used for the lift calculation as well:

$$\mathbf{D}_i = \rho \mathbf{v}_i \times \mathbf{\Gamma}, \tag{2.38}$$

where $\mathbf{v}_i$ is the induced velocity vector and, again, $\mathbf{\Gamma} = \Gamma \Delta \mathbf{l}$.

The parasitic drag is determined by using the airfoil tables as given by [Timmer, 2017]. From the tables, the given drag coefficient is transformed to a drag force at the bound vortex panel, using:

$$\mathbf{D}_{par} = \left(\frac{1}{2} \rho V_{total}^2 S c_d \right) \mathbf{e}_\phi, \tag{2.39}$$

where the unit vector $\mathbf{e}_\phi$ is aligned with the resultant velocity vector, c_d is the local drag coefficent, and S represents the panel area considered. Decomposing the unit vector in the plane of rotation by means of tangential component and a normal component, the unit vector $\mathbf{e}_\phi$ is expressed as $(\cos\phi, 0, \sin\phi)$. In this manner, parasite drag components give the correct contributions in the plane of

rotation as drawn in Figure 2.15. For the parasitic drag coefficient, the local angle of attack required for the aerodynamic look-up tables is determined as:

$$\alpha_i = \phi_i - (\theta_i + \theta_c)\,, \tag{2.40}$$

where α_i is the local angle of attack, ϕ_i the local inflow angle, θ_i the local structural twist angle, and θ_c the collective pitch angle for power control. Assuming that the airfoil as a function of the blade span is given, the appropriate drag coefficient can be searched using the local angle of attack.

The lift, drag, and moment vectors are expressed in the normal and tangential components with respect to the plane of rotation, which means that the normal and tangential contributions of the aerodynamic loads are immediately suitable for the aerodynamic power calculation. Subsequently, the aerodynamic power is calculated as:

$$P = \Omega \sum (\mathbf{L}_i + \mathbf{D}_i) \cdot \boldsymbol{\mathcal{R}}_0 \mathbf{r}_i, \tag{2.41}$$

with $\boldsymbol{\mathcal{R}}_0$ the transformation shown in Equation 2.1. From the above equation, it is observed that the aerodynamic power is based on the tangential force, parallel to the x-axis in the plane of rotation as indicated in Figure 2.15.

Blade pitch control

Wind turbine blades use two types of control: stall regulated or pitch regulated. The control mechanism in this work is pitch control, for recent stall regulated studies it is referred to [Ferede, 2016]. The pitch type of control gives a blade pitch command when the generated power of the complete rotor from the wind exceeds rated power. The blade is pitched towards lower angles of attack so that the aerodynamic blade loads decrease and the power available is rated power. The necessary information for the blades to stay within the wind turbine normal operation envelope is obtained from controller design used in the NREL 5MW report, [Jonkman et al., 2009]. In this research, the control is such that the rated power per blade is not exceeded. This means that the difference between the actual power and the rated power for the blade considered is compared and a pitch action is carried out such that the power stays within the power limits of the turbine considered. The convergence criterion for this algorithm is chosen to be the ratio between the power difference and the rated power:

$$\left| \frac{\Delta P}{P_{rated}} \right| \leq \epsilon. \tag{2.42}$$

The implementation of the aerodynamic power calculation, including a simple collective pitch control mechanism, is shown in figure 2.16.

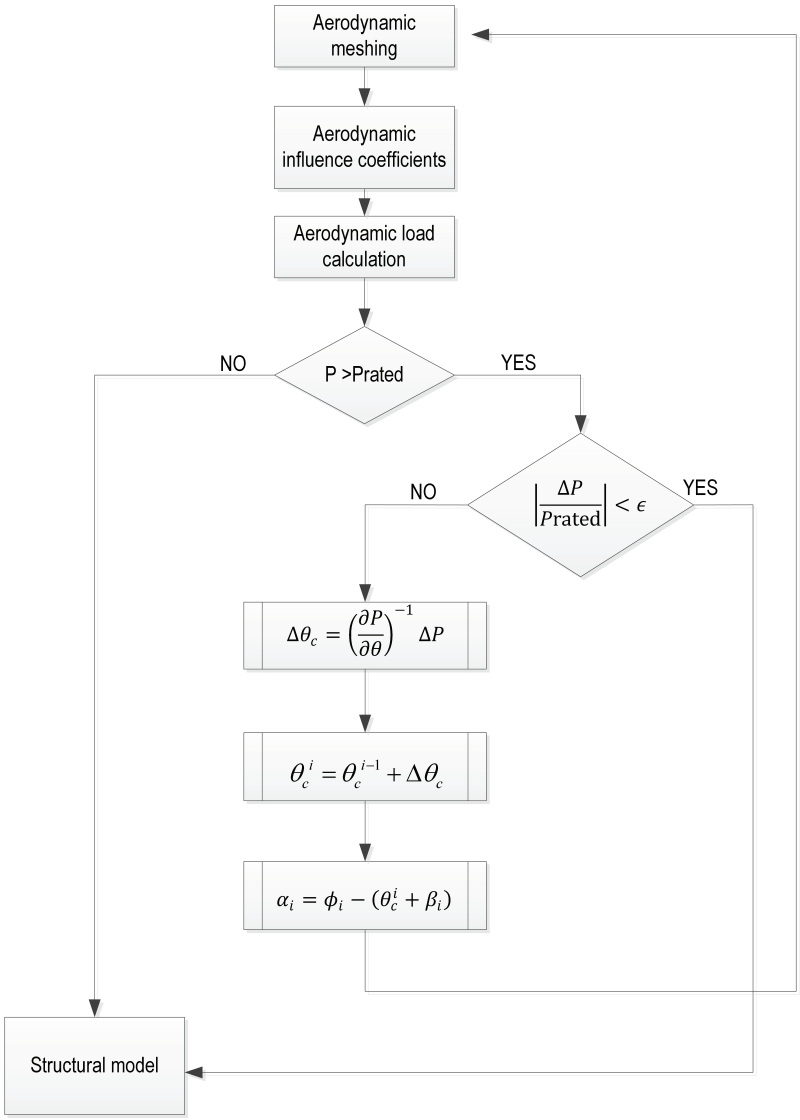

Figure 2.16: Pseudo code for aerodynamic power calculation embedded in the aeroelastic analysis. The flowchart shows that firstly the aeropower from the panel method is evaluated; after this, it is checked whether the power is above rated and is driven towards rated power.

2.4 AEROELASTIC BLADE MODELLING

The idea of equal fidelity modelling is that the models that interact during the aeroelastic iteration procedure are based on physics that is of comparable fidelity. That means that the aerodynamic vortex panel model should have a similar set-up as the structural model. The aerodynamic model exists of quadrilateral vortex panels which are meshed on the blade and in the wake. The panels generate the vorticity at the bound surface at which the aerodynamic load per bound surface element is calculated. Those elements give a contribution to the aerodynamic loads with respect to the quarter chord point of the local aerofoil resulting in the spanwise aerodynamic load distribution at the total quarter chord line of the blade. Concluding: a vortex panel model determines the aerodynamic load distribution across the wind turbine quarter chord line, which is input for the aeroelastic analysis. The structure is first reduced from a full 3D shape to a 1D beam model, so the structural 1D beam model was also constructed from a more refined structural model. This can be compared to the line model resulting from the vortex panel code. Both lines serve as input for the aeroelastic analysis and give proper results and are not limited to the accuracy of the model with the lowest fidelity. The aeroelastic analysis couples the aerodynamic and structural model using the sensitivities of the structural loads with respect to the structural degrees of freedom as well as the aerodynamic loads with respect to the structural degrees of freedom, which is known as a close coupled solution strategy. The aeroelastic solution is found from a non-linear analysis that is shown in Figure 2.17. Following this procedure, first the difference between the aerodynamic forces and the structural forces are compared:

$$\mathbf{f}_s\left(\mathbf{p}\right) - \mathbf{f}_a\left(\alpha, \mathbf{p}, q\right) - \mathbf{f}_{\text{ext}}\left(\mathbf{p}\right) = \mathbf{R}, \tag{2.43}$$

where the residual $\mathbf{R}$ should be equal to zero for the equilibrium situation. Furthermore, it should be noted that the vector $\mathbf{f}_{ext}$ contains the gravity forces and the centrifugal forces. Then, for the first load estimation this equation is linearised around the structural deformation $\mathbf{p}_0$ with a perturbation $\Delta\mathbf{p}$. The dynamic pressure q, within the aerodynamic force, is only dependent on the air density and the local velocity. The aeroelastic equation is written as:

$$\left.\frac{\partial \mathbf{f}_s}{\partial \mathbf{p}}\right|_{\mathbf{p}_0} \Delta\mathbf{p} + \mathbf{f}_s\left(\mathbf{p}_0\right) - \left.\frac{\partial \mathbf{f}_a}{\partial \mathbf{p}}\right|_{\mathbf{p}_0} \Delta\mathbf{p} - \mathbf{f}_a\left(\alpha, \mathbf{p}_0, q\right) - \left.\frac{\partial \mathbf{f}_{\text{ext}}}{\partial \mathbf{p}}\right|_{\mathbf{p}_0} \Delta\mathbf{p} - \mathbf{f}_{\text{ext}}\left(\mathbf{p}_0\right) = \mathbf{0}, \tag{2.44}$$

where the residual at the equilibrium position is defined as:

$$\mathbf{R}_0 = \mathbf{f}_s\left(\mathbf{p}_0\right) - \mathbf{f}_a\left(\alpha, \mathbf{p}_0, q\right) - \mathbf{f}_{\text{ext}}\left(\mathbf{p}_0\right) = \mathbf{0}. \tag{2.45}$$

The equation could also be expressed in terms of stiffness matrices:

$$\underbrace{(\mathbf{K}_s - \mathbf{K}_a - \mathbf{K}_{\text{ext}})}_{\mathbf{J}} \Delta\mathbf{p} = -\mathbf{R}_0 \tag{2.46}$$

The difference between the structural stiffness matrix, the aerodynamic stiffness matrix, and the stiffness matrix due to the external forces as shown in Equation 2.46, is defined as the Jacobi matrix $\mathbf{J}$. The system has a physically correct solution when the residual $\mathbf{R}$ in Equation 2.43 becomes zero, the system is in static equilibrium. This is accomplished by using the Newton-Raphson root finding algorithm.

Sensitivities for aeroelastic analysis

For an optimum convergence of the iterative solution procedure it is essential that the sensitivities with respect to the structural degrees of freedom are correct. The sensitivities of the aerodynamic forces are determined analytically, by differentiating the necessary variables with respect to structural degrees of freedom. The aerodynamic forces $\mathbf{f}_a$ on the blade are to be differentiated with respect to the structural degrees of freedom $\mathbf{p}$ analytically. By means of example, the sensitivity analysis for the lift force looks as follows. Since the aerodynamic loads are determined by a vortex lattice method followed by the aerodynamic load calculation as shown in equations 2.36, 2.37, 2.38, and 2.39, the sensitivities of the lift force at a segment of length $\Delta\mathbf{l}$ are obtained by differentiating 2.36 with respect to the structural degrees of freedom:

$$\frac{\partial \mathbf{L}}{\partial \mathbf{p}} = \rho \mathbf{V} \times \left(\frac{\partial \Gamma}{\partial \mathbf{p}} \Delta\mathbf{l} + \Gamma \frac{\partial \mathbf{l}}{\partial \mathbf{p}} \right) \tag{2.47}$$

From equation 2.47 it is clear that an analytical expression is required for the derivatives of both the vortex strength and the resulting direction vector of the vortex line with respect to the structural degrees of freedom. Realising that the vortex strength and the direction of the vortex line of the aerodynamic panel considered both originate in the definition of the aerodynamic mesh of the blade and the wake, it is essential to determine the sensitivity of the blade aerodynamic mesh nodes with respect to structural deformations of those nodes. As a consequence, the wind turbine blade wake will change with the structural deformation as well. This means that the derivatives of the wake panel nodes with respect to the structural deformations are also required.

With the structural deformations in mind, the sensitivities of the aerodynamic panel nodes with respect to the structural degrees of freedom can be determined by differentiating expression 2.34:

$$\frac{\partial \mathbf{x}_{p,k}}{\partial \mathbf{p}} = \left[\frac{\partial r_k}{\partial \mathbf{p}} \sin \Delta\Psi_k, \frac{\partial r_k}{\partial \mathbf{p}} \cos \Delta\Psi_k, 0 \right] \tag{2.48}$$

Note that this wake is described in the fixed blade root coordinate system, see Equation 2.34. In Equation 2.48 the vector $\mathbf{x}$ represents aerodynamic mesh coordinates, r_k the local blade radius position, $\Delta\Psi$ the azimuthal increase. The undisturbed wind velocity v_w has vanished from the wake sensitivity analysis, considering the sensitivities with respect to the structural degrees of freedom $\mathbf{p}$. From this information the sensitivities of the influence coefficients with respect to the structural coordinates can be derived which leads to the information required for the aerodynamic stiffness matrix $\mathbf{K}_a$. A sensitivity check has been done by comparing the analytical derivatives with the central finite differences; the difference was less than 10^{-4} %. For the close coupling of the aerodynamic model and the structural model, the required sensitivities can be used with confidence within the aeroelastic model. The nonlinear load calculation is summarised in Figure 2.17.

In this pseudo code is shown that the outer loop takes care of the increase in loading. In the case of the static aeroelastic analysis, the wind speed is increased from zero towards the rated wind speed and is indicated as non-dimensional incremental load variable λ that varies between 0 and 1. Furthermore, the inner loop represents the Newton Raphson iterative root finding algorithm that is searching for a static equilibrium. The residual force $\mathbf{R}$ and the combined aerodynamic and structural stiffness matrix $\mathbf{J}$ meant are the variables from equation 2.46. The convergence has been reached when:

$$\left| \frac{\Delta \mathbf{p}}{\mathbf{p}} \right| \leq 10^{-5} \tag{2.49}$$

2.5 AEROELASTIC VALIDATION OF THE 5MW NREL BASELINE ROTOR BLADE

For the aerodynamic validation of the blade, a normal wind profile atmospheric wind shear function, see [IEC, 2005], has been adopted and the blade geometry has been sketched in Figure 2.18.

The exact data for the blade twist angle, the chord distribution, and the aerofoil distribution as a function of the blade span are presented in Table 2.1.

The aerodynamic loading results from Proteus are compared with the thoroughly validated BEM aerodynamic model. It is shown that the normal force distribution follows the BEM results very closely, see Figure 2.19. In addition, the result

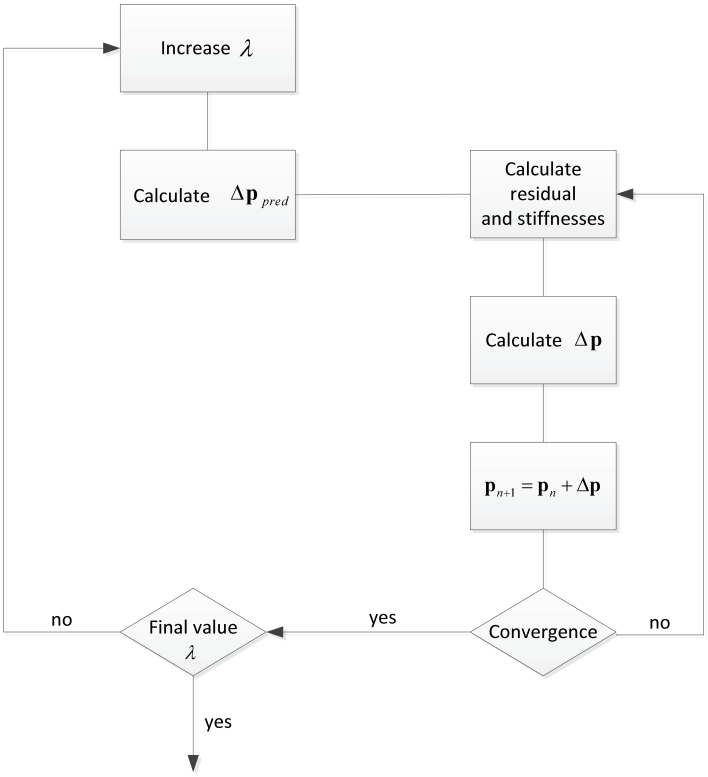

Figure 2.17: The aeroelastic analysis as an example for nonlinear load calculation

NACA0012 indicates a result without camber: this clearly shows that the power generation of the blade will not be sufficient. The tangential force, however, Figure 2.20, shows some significant deviation from the BEM model which has consequences for the aerodynamic power calculation.

The cause for the difference in tangential force distribution can be found in the calculation procedure. The tangential force is built of the lift and the drag components and are subtracted. In general, the lift and drag components in tangential direction are of equal order of magnitude which means that small deviations in both lift and drag components could generate bigger differences in tangential force. For the calculation of rated power, the consequence is that the aerodynamic power is overestimated slightly. In this case, a total power of 6 MW is determined which is acceptable in comparison with the 5.3 MW from [Jonkman et al., 2009].

A pitch-regulated wind turbine allows increasing power and tip displacements below rated wind speed, while at rated wind speed the maximum power and tip displacement are reached. Above rated, the power remains approximately constant and the tip displacement drops with increasing wind speed. The blade

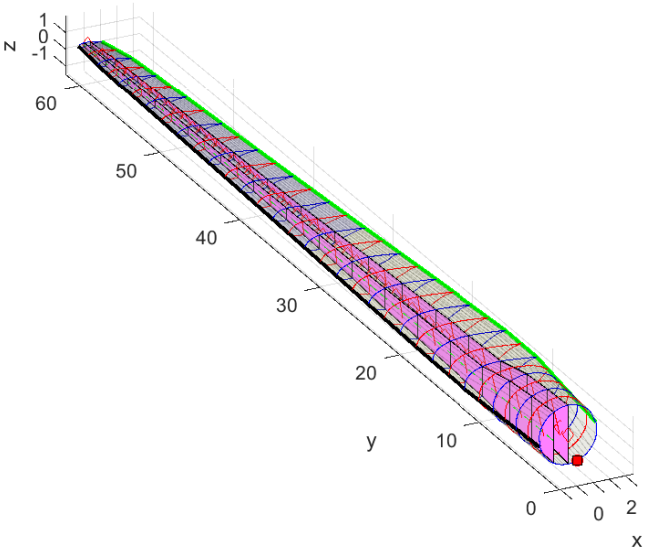

Figure 2.18: Three dimensional representation of the 5MW NREL blade

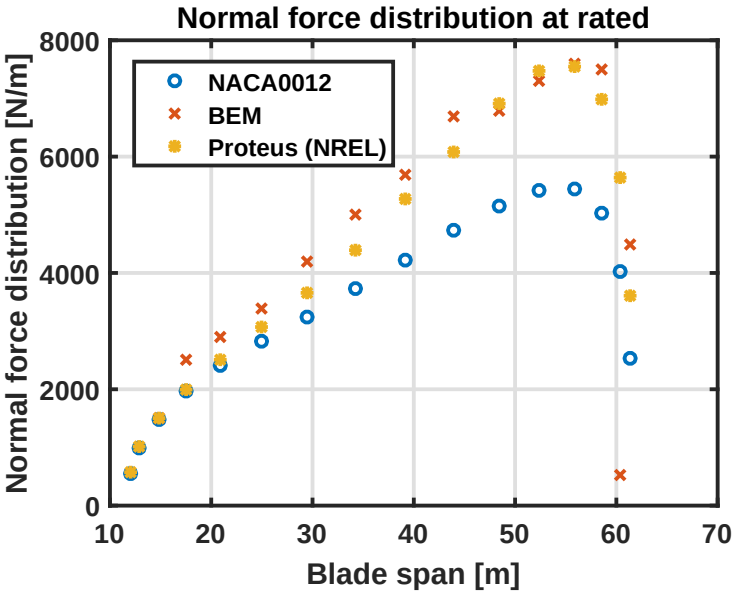

Figure 2.19: Normal force distribution comparison between BEM and the vortex lattice model in PROTEUS.

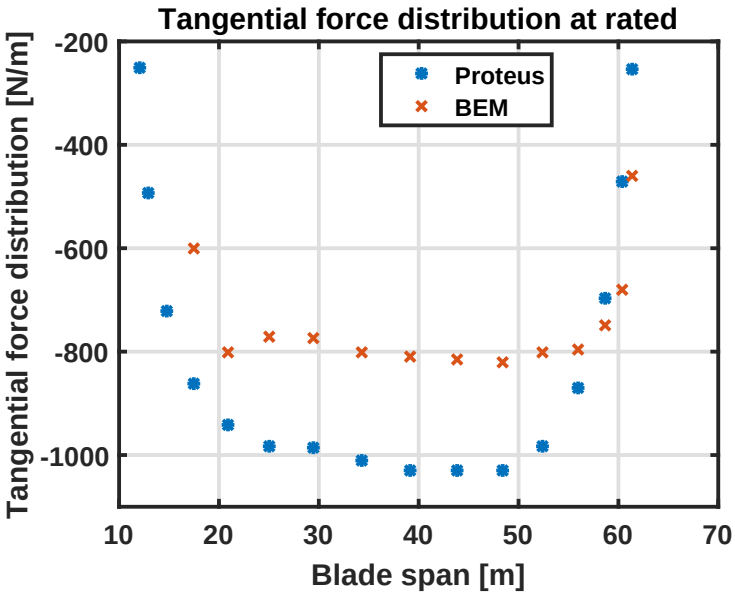

Figure 2.20: Tangential force distribution comparison between BEM and the vortex lattice model in PROTEUS.

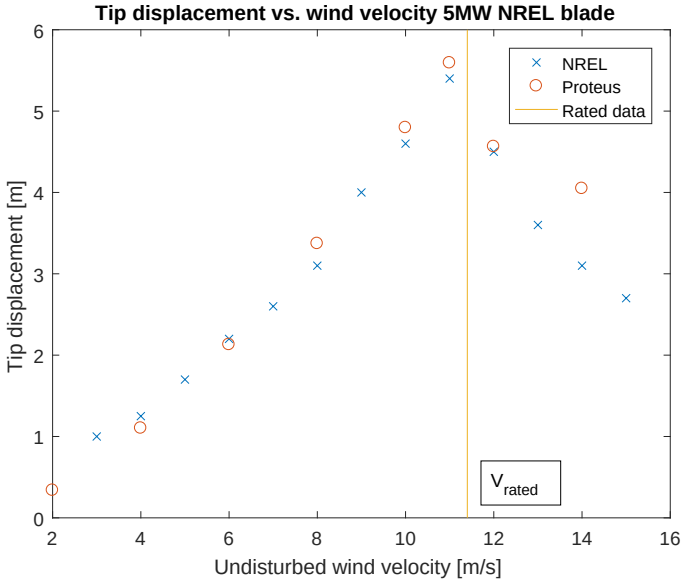

Figure 2.21: Tip deflection as a function of wind velocity for NREL 5MW blade NWP, blade position vertical up.

Table 2.1: Summary of blade twist- and chord distribution as a function of the blade radius for the 5MW NREL reference blade.

Blade radius [m]	Blade twist [deg]	Blade chord [m]	Airfoil type
2.8667	-13.308	3.542	Circular
5.6000	-13.308	3.854	Circular
12.0000	-13.308	4.557	DU35-A17
19.9500	-10.162	4.458	DU35-A17
28.00	-7.795	4.007	DU30-A17
36.35	-5.361	3.502	DU21-A17
44.55	-3.125	3.01	NACA64-A17
52.75	-1.526	2.518	NACA64-A17
56.17	-0.863	2.313	NACA64-A17
58.90	-0.37	2.086	NACA64-A17

pitch should alleviate the blade loading and as such, the power should remain constant. The tip displacement function for the NREL blade is shown in Figure 2.21. Together with Figure 2.22, it is observed that the below-rated power and tip displacements behave properly compared to the baseline NREL blade. Above rated, the power and the tip deflection do not follow the NREL results. This is due to convergence issues in the control algorithm shown in Figure 2.16. For a convergence criterion of $\epsilon = 10^{-2}$ the above-rated power and tip displacements result from the algorithm but are but are questionable. For smaller values for ϵ, convergence is not reached, especially for the wind speeds above 14 m/s. Since the optimisations are carried out slightly below rated, the above-rated behaviour is not an issue for the optimisation point mentioned.

2.6 CONCLUDING REMARKS

The aeroelastic equal fidelity modelling procedure generates aeroelastic solutions that contain the accuracy of both the aerodynamic model and the structural model. Comparable accuracy of the models is based on the idea of transforming a 3D representation of the blade aerodynamics and blade structural behaviour towards a 1D representation of the blade behaviour. The 1D blade representation is used for the aeroelastic analysis. The aerodynamic model and the structural model have been described separately as well as the close coupling between both models to produce aeroelastic results.
Starting with the structural model, it has been pointed out that a sandwich composite model in a simplified form has been implemented correctly within the structural model, including the use of the lamination parameters. Furthermore, the **ABD** matrix of the sandwich composite was coupled to the lamination parameters. Using this **ABD** information of each laminate within the 3D representation of the blade, the blade was transformed to a 1D beam model with preserving the orthotropic behaviour of the sandwich laminates. This resulting section property information served as an input for a Timoshenko beam finite element model of

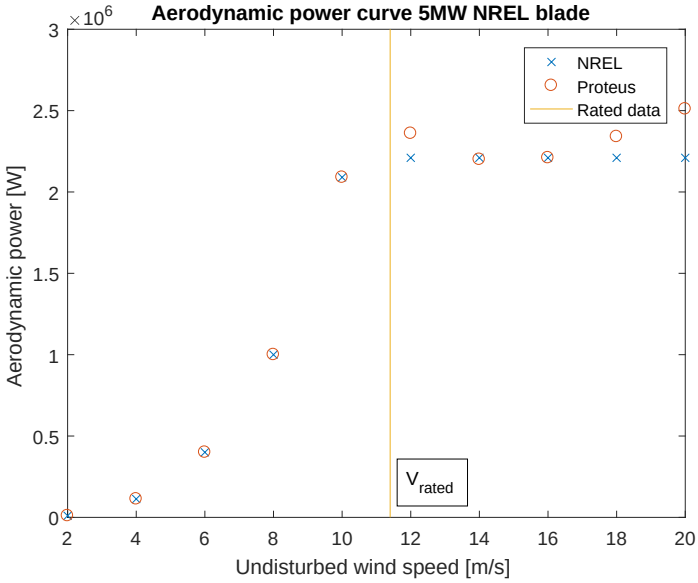

Figure 2.22: Power curve of NREL 5MW blade (vertical up) normal wind profile. Note that this is the power contribution for one blade only, the other blades make the total power generated by the full rotor.

the blade. This beam model assumes linear elastic material behaviour but is embedded in a corotational framework which allows geometric nonlinearities such as large displacements. For the wind turbine blades, it is important to include centrifugal forces as they stiffen the blade and due to large blades rotating through the gravity field, the gravitational force has also been taken into account. Both effects were introduced as external forces on the beam nodes, and the results were verified within this chapter and matched the expectations from the theory.
The aerodynamic model uses the blade and the wake geometry to define the coordinates of the corner points of the vortex panels. From the vortex panels, the aerodynamic forces and moments are calculated for each aerodynamic blade section, for the blade section the blade element approach is used: the local velocities determine the inflow angle and the angle of attack that determine the aerodynamic load distribution across the quarter chord line.
The aeroelastic coupling has been accomplished by using close coupling of the aerodynamic and the structural model. For the structural forces, the aerodynamic forces, and the external forces, the sensitivities with respect to the structural degrees of freedom were determined; the sensitivities were used in the Newton - Raphson root-finding algorithm for the iterative solution of the aeroelastic equations.

It can be concluded that the aeroelastic model behaves as expected, below and at rated wind speed. The above-rated results are questionable due to convergence issues of the pitch control algorithm. This has been concluded from the aerodynamic tangential force, the normal force, the tip displacement as a function of the undisturbed wind velocity and power curve. since they are only carried out slightly below rated. However, the questionable behaviour of the pitch controller does not have consequences for the proposed optimisations in this work.

3

Optimisation procedure

In this chapter, the optimisation framework is explained as well as the position of the cross-sectional modeller and the aeroelastic model within this framework. For the optimisation, the objective function has to be chosen, as well as the appropriate design variables and the constraints. Besides the design variable vector, the sensitivities of the objective and the constraints with respect to the design variables are required. As such, the relation between the objective function and the design variables is described as well as the relation between the constraints and the design variables. While the work of [Werter, 2017] mentions an objective function that considers mass minimisation of pure fibre composite materials, the emphasis in this research is on objective functions considering sandwich composite structural models as mentioned in chapter 2. Furthermore, appropriate load cases are proposed for a static aeroelastic optimisation and the atmospheric wind velocity behaviour significant for the blade loading is discussed. Finally, the impact of a stiffness optimisation on the year power production is discussed.

3.1 Aeroelastic optimisation

As explained in [Liao et al., 2012], the cost of energy is a significant objective. However, this objective has many variables each possessing a different level of significance with respect to the cost of energy objective. To avoid the difficulties mentioned when using the cost of energy as an objective, it was decided to perform

a stiffness optimisation where the blade mass will be minimised. Blade mass is an important indicator of blade costs, especially for increasing blade dimensions. In addition, as an objective function, it contains clearly defined variables, and the number of variables is inherently limited due to the definition of mass. As such, the objective function mass must be formulated with structural parameters available in the model, such as laminate thickness and material density. For a structural optimisation as performed during this research, the most significant constraints are the Tsai-Wu strain factor, the lamination parameters feasibility constraints, panel buckling, tip displacements and a predefined aerodynamic power loss. It has been realised that the tip deflection is dependent on the blade azimuth, however, tip deflection is only an issue for blade - tower passage. As such, the tower clearance case and the highest aerodynamic blade loading do not coincide. The highest blade loading occurs when the blade is in the vertically upward position: the wind velocity is higher in this region. In the vertically downward position tower passage is an issue, however, the wind velocity in this region is lower and the blade loads are lower as well. To be sure that tower clearance is safe, the maximum deflection has been applied together with the case where the aerodynamic loads are highest. Considering the constraints and the objective mentioned above, the stiffness of the blade is controlled such that the constraint functions are not violated during the mass minimisation procedure. The aeroelastic optimisation framework is summarised in Figure 3.1.

Next, the gradient-based optimisation problem is formulated as

$$\begin{aligned} &\min_{\boldsymbol{\xi}} \quad m\left(\boldsymbol{\xi}\right) \\ &\text{subject to} \quad g_i\left(\boldsymbol{\xi}\right) \leq 0, \end{aligned} \tag{3.1}$$

also including the derivatives of the objective function, the mass m, and the constraint functions g_i with respect to the design variables $\boldsymbol{\xi}$:

$$\frac{\partial m}{\partial \boldsymbol{\xi}} \text{ and } \frac{\partial g_i}{\partial \boldsymbol{\xi}}. \tag{3.2}$$

This means that the mass m, dependent on the design variables $\boldsymbol{\xi}$ subject to the constraints g_i that are functions of the design variables $\boldsymbol{\xi}$, is minimised. The gradients take care of the convergence speed of the optimisation, which also depends on the chosen method for handling the gradient. Per sandwich laminate, the design variable vector consists of 8 lamination parameters and 2 thickness parameters for sandwich laminates, t_f and t_c, the face and the core respectively. It is assumed that the upper and the lower face sheets are identical in lay-up and thickness. For the mass optimisation of a sandwich laminate, the mass objective function m depends only on the laminate thickness, width, height, and laminate density. In Table 3.1 the difference is shown between the number of design vari-

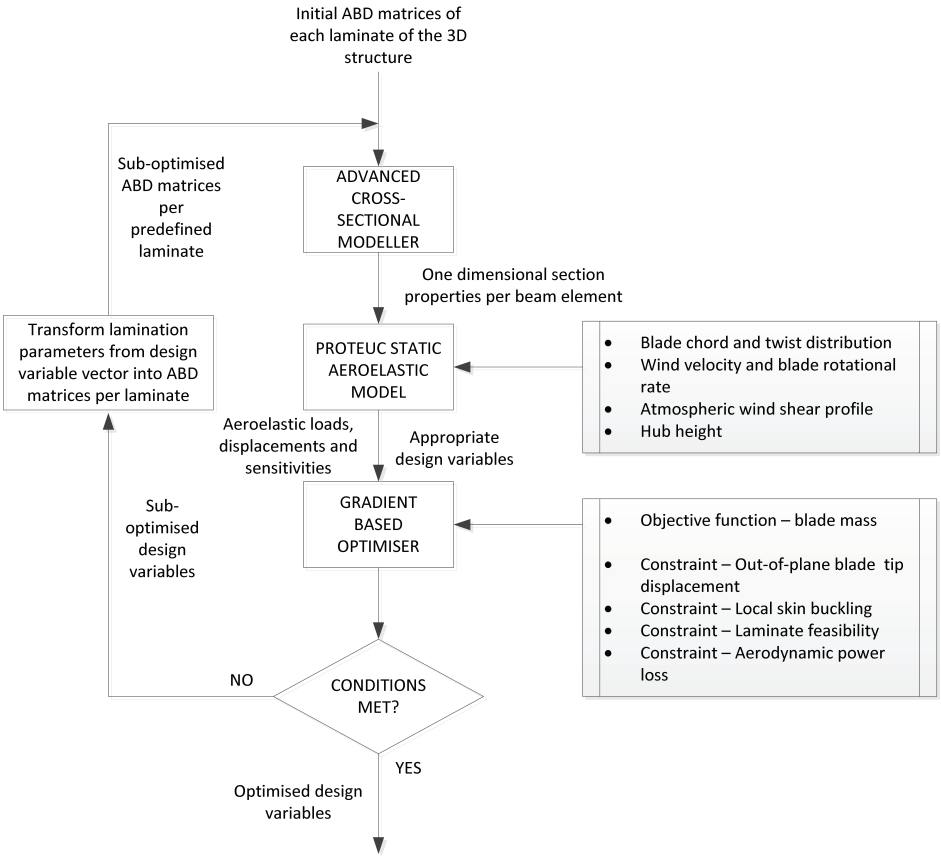

Figure 3.1: The aeroelastic optimisation framework. This flowchart clearly shows the position of the cross-sectional modeller and the aeroelastic model with respect to the optimiser GCMMA. Each iteration step the lamination parameters are conversed to the appropriate ABD matrices of the 3D structure. In this manner, the computational effort is improved.

Table 3.1: Number of design variables per laminate and per cross-section.

	Sandwich laminate		Pure fibre laminate	
	balanced	unbalanced	balanced	unbalanced
# design variables per laminate	6	10	5	9
# laminates per cross-section	8	8	8	8
# design variables per section	48	80	40	72

ables for pure fibre laminates and sandwich laminates per cross-sectional panel for balanced, symmetric laminates and for unbalanced but symmetric laminates.

The sensitivity of the mass is determined by defining a derivative with respect to the thickness of the laminate multiplied by the sensitivity of the thickness with respect to the design variables. For a single blade segment for a pure laminate the mass sensitivity with respect to the design variables is written as:

$$\frac{\partial m_i}{\partial \boldsymbol{\xi}} = \frac{\partial m_i}{\partial t_i}\frac{\partial t_i}{\partial \boldsymbol{\xi}}, \tag{3.3}$$

and gives the direction change of the elemental mass as:

$$\Delta m_i = \frac{\partial m_i}{\partial \boldsymbol{\xi}}\Delta \boldsymbol{\xi}. \tag{3.4}$$

For the case of a sandwich laminate, the thickness of the laminate consists of two faces and a core. From chapter 2 it can be concluded that if the facing sheets consist of symmetric laminates and the sandwich laminate is symmetric as well, the facing sheets are equal in thickness and lay-up. As such, defining the thickness and lamination parameters of only one facing sheet is sufficient, which results in the following thickness vector per laminate:

$$\mathbf{t}_i = \left(t_f \;\; t_c\right)_i, \tag{3.5}$$

and the sensitivity with respect to the design variable vector:

$$\frac{\partial \mathbf{t}_i}{\partial \boldsymbol{\xi}} = \begin{pmatrix} \frac{\partial t_f}{\partial \boldsymbol{\xi}} & \frac{\partial t_c}{\partial \boldsymbol{\xi}} \end{pmatrix}_i, \tag{3.6}$$

which, for the i-th sandwich laminate, results in a sensitivity vector $[(\mathbf{0}\;\;1\;\;0)\;\;(\mathbf{0}\;\;0\;\;1)]$. For the sandwich laminate case, the sensitivity of the elemental mass is defined with respect to the elemental thickness vector and multiplication with this sensitivity matrix $\partial m_i/\partial \mathbf{t}_i$ gives the elemental mass with respect to the design variable vector as shown in expression 3.3. For the gradient-based optimisation, the globally convergent method of moving asymptotes (GCMMA), see [Svanberg, 2002],

is chosen. In aeroelastic optimisation problems is often dealt with complicated response functions with multiple extrema, for the objective function as well as for the constraints. This makes the globally convergent method a well-suited optimiser within this research.

3.2 DESIGN FORMULATION

LOAD CASES

The load cases considered are a limited number of normal cases complemented with a heavy load case: extreme wind shear. It is expected that this selection provides sufficient reflection of all load cases experienced during the lifetime of the wind turbine. The wind turbine environmental design requirements are described in detail in the international standard for design requirements for wind turbines, see [IEC, 2005]. In this research, only static aeroelastic optimisations are carried out. The most suitable load cases for such static cases are the normal wind profile load case (NWP) and the extreme wind shear load case (EWS). The wind profiles as a function of height are sketched in Figure 3.2. Essentially, the extreme wind shear case is not a real static load case, so the largest amplitude possible is considered to mimic a heavier blade loading for a static optimisation. It is expected that the EWS case is the critical case for the optimisations, which will be demonstrated in chapter 4.

For interpreting Figure 3.2, it should be realised that the 5MW, 10MW, and 20MW turbines have different hub heights. Furthermore, according to [IEC, 2005], the velocity profile for normal operation is given as:

$$V(z) = V_{\text{hub}} \left(\frac{z}{z_{\text{hub}}} \right)^{0.2}. \tag{3.7}$$

Since this expression relates the wind velocity to the turbine hub height, it suggests that the velocity profiles are dependent on the power they produce. Of course, this is not true: the intention of expression 3.7 is to estimate the wind shear correctly for the different hub heights. A consequence of this expression is that the plotted velocity profiles are slightly different; one should realize that only the part of the velocity profile is used that is within the rotor swept area. The same is true for the extreme wind shear profiles; they are also based on the normal wind profile. As such, for the extreme wind shear plots, it should be realised as well that only the velocities within the rotor swept area are valid for the load calculations on the blade.

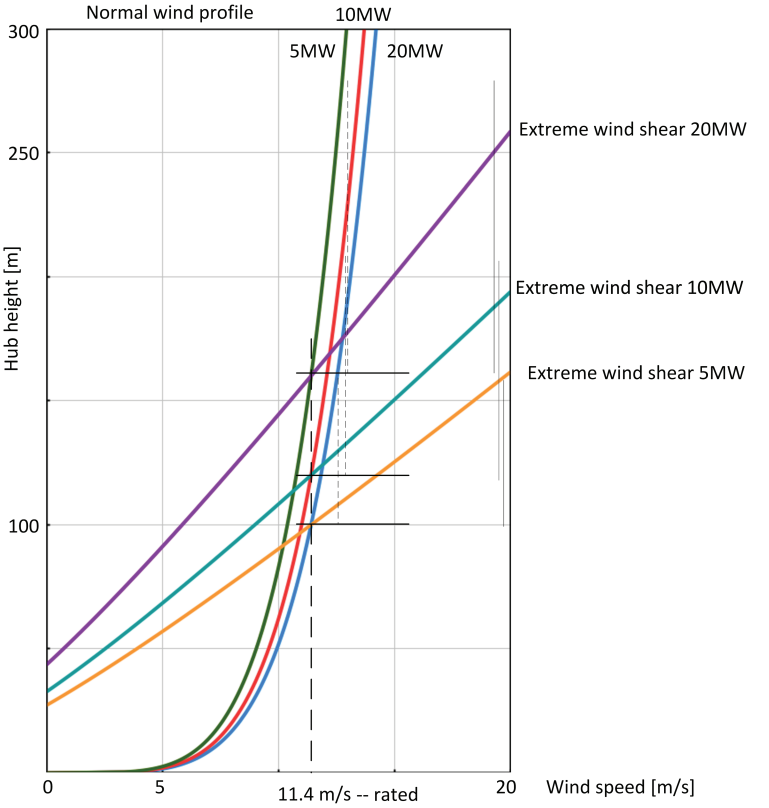

Figure 3.2: Normal wind profile and extreme wind shear profile. For each of the power configurations the normal wind profile, as well as the extreme wind shear profile, is sketched as a function of the height.

Objective

This study searches for a minimum blade mass using the variable stiffness concept. The blade mass is calculated as follows:

$$m = \sum_i \left(2\rho_{f_i} t_{f_i} + \rho_{c_i} t_{c_i}\right) l_i h_i, \tag{3.8}$$

where ρ_f is the facing sheet material density, ρ_c the core material density, t_f the facing sheet thickness, t_c the core thickness, l_i the length of the cross-sectional panel, and the h_i the average height of the cross-sectional panel. From Equation 3.8 it is evident that the mass only contains the thickness variation of the skin and the spars assuming that the segments are constant during the optimisation loop. The objective function contains only the facing sheet thickness and the core thickness as design variables for sandwich blades, while for full fibre laminates the only design variable is the laminate thickness. The stiffness variation resulting from the stacking sequence originates from the constraints.

Design variables

The blades are structurally optimised using the sandwich laminate properties or the pure fibre laminate properties, depending on the desired structural blade design. For the sandwich laminate, this is done by using the lamination parameters of the faces, the thickness of the faces, and the thickness of the core as separate design variables. For pure fibre laminates, the lamination parameters of the laminate together with the thickness of the laminate are the necessary variables for the optimisation procedure. The design variables per laminate are summarised in the vector:

$$\boldsymbol{\xi} = [V_{1\mathbf{A}}, V_{2\mathbf{A}}, V_{3\mathbf{A}}, V_{4\mathbf{A}}, V_{1\mathbf{D}}, V_{2\mathbf{D}}, V_{3\mathbf{D}}, V_{4\mathbf{D}}, t_f, t_c] \tag{3.9}$$

for a symmetric, unbalanced sandwich laminate. For balanced laminates, the lamination parameters $V_{2\mathbf{A}}, V_{4\mathbf{A}}, V_{2\mathbf{D}}, V_{4\mathbf{D}}$ are omitted, which reduces the computational effort significantly. The optimisations will be carried out for a quasi-isotropic case and the symmetric, balanced laminate case. For the quasi-isotropic lay-up, all lamination parameters remain unchanged during the optimisation and only the thickness of the laminate is a variable. For pure fibre laminates, the thickness t_c vanishes from Equation 3.9 because of the absence of a core and the only thickness remaining is t_f, in that case, the laminate thickness.

Constraints

As mentioned in [Chehouri et al., 2015], the choice of constraints is somewhat arbitrary. Within this review, the constraints are roughly divided into geometric, aerodynamic and structural constraints. For the stiffness optimisation, as an aerodynamic constraint, the aerodynamic power loss is considered; furthermore, the geometric and structural constraints determine the stiffness of the laminates. To be more specific, for the wind turbine blades in this research, the most significant constraints are:

- minimum and maximum strain of the skins and the spars;
- skin and spar buckling;
- tip deflection;
- the aerodynamic power loss.

In a gradient-based optimisation not only the gradient of the objective function is important, but the gradients of the constraint functions do also matter as well. Since the design variable vector is defined as $\boldsymbol{\xi}$, the gradients of the constraints functions are determined with respect to this design variable vector. As such, the response sensitivities are found by differentiating the constraint functions with respect to the design variable vector $\boldsymbol{\xi}$. Clearly, for this optimisation problem, the number of constraints is larger than the number of design variables, see Table 3.1, therefore direct sensitivities are used. The differentiation is carried out analytically to be more numerically efficient within the optimisation loop.

Strain: For the strain constraints the procedure from [Werter, 2017] is used. The strain constraints are determined by evaluating the strain responses per structural element. The most critical strain responses for each laminate within the cross-sections are identified by determining the four most critical Tsai-Wu strain factors. Subsequently, those critical strain factors are introduced as constraints. Next, the gradient of the strains with respect to the design variables is considered. The beam strains as mentioned in Equation 2.23 originate from the local composite sectional elements from the 3D blade representation; the cross-sectional modelling technique mentioned in chapter 2 transforms the local strains into 1D beam strains including the sensitivities with respect to the local $\mathbf{A}$ and $\mathbf{D}$ matrices. For the extension strains, as an example for all strains, the response sensitivity is determined as follows:

$$\frac{\partial \epsilon}{\partial \boldsymbol{\xi}} = \frac{\partial \epsilon}{\partial \mathbf{A}} \frac{\partial \mathbf{A}}{\partial \boldsymbol{\xi}} + \frac{\partial \epsilon}{\partial \mathbf{D}} \frac{\partial \mathbf{D}}{\partial \boldsymbol{\xi}} + \frac{\partial \epsilon}{\partial \mathbf{t}} \frac{\partial \mathbf{t}}{\partial \boldsymbol{\xi}} \tag{3.10}$$

The extensional strain sensitivity of the beam element considered, with respect to the full set of design variables on the left-hand side, is also expressed in sensitivities of the beam strain with respect to the local thickness vector $\mathbf{t}$. Finally, the local $\mathbf{A}$ and $\mathbf{D}$ matrices and thickness information is differentiated with respect to the full set of design variables to find the dependence of the local structure with respect to the full blade.

The minimum extensional strain ϵ and the shear strain γ show the same dependence. For each of the constraint functions, the sensitivities of the $\mathbf{ABD}$ matrices with respect to the design variables are determined. The sensitivity formulation as in Equation 3.10 can be used for both full fibre laminates and for sandwich laminated. However, for the correct response sensitivities of sandwich laminates, the required sensitivities are slightly different compared to pure fibre laminates and can be calculated as follows:

$$\frac{\partial \mathbf{A}}{\partial \boldsymbol{\xi}} = 2\frac{\partial \mathbf{A}_f}{\partial \boldsymbol{\xi}} \tag{3.11}$$

and

$$\frac{\partial \mathbf{D}}{\partial \boldsymbol{\xi}} = 2\frac{\partial \mathbf{D}_f}{\partial \boldsymbol{\xi}} + \frac{1}{2}\frac{\partial \mathbf{A}_f}{\partial \boldsymbol{\xi}}(t_f + t_c)^2 + \mathbf{A}_f\,(t_f + t_c)\left(\frac{\partial t_f}{\partial \boldsymbol{\xi}} + \frac{\partial t_c}{\partial \boldsymbol{\xi}}\right) \tag{3.12}$$

Especially from Equation 3.12 it is clear that the sandwich is optimised for core thickness as well, which helps the skin and the spars to prevent buckling. Furthermore, it is noted that for pure fibre laminates only one total laminate thickness t per laminate is defined. For sandwich laminates, the thickness of the laminate involves two facing sheets and a core. This is summarised in a thickness vector $\mathbf{t}$ to indicate the difference between the facing sheet thickness and the core thickness.

BUCKLING: The buckling factor calculation r is explained in chapter 2, and is calculated by solving the eigenvalue problem as described in Equation 2.13. Essentially, the quantity r expresses the ratio between the actual loading of the panel and the local critical buckling load. For limiting the number of buckling constraints, the most critical buckling panels per laminate are used, again following [Werter, 2017]. The buckling factor sensitivity has similar behaviour as the strain sensitivity with respect to the design variables:

$$\frac{\partial r}{\partial \boldsymbol{\xi}} = \frac{\partial r}{\partial \mathbf{A}}\frac{\partial \mathbf{A}}{\partial \boldsymbol{\xi}} + \frac{\partial r}{\partial \mathbf{D}}\frac{\partial \mathbf{D}}{\partial \boldsymbol{\xi}} + \frac{\partial r}{\partial \mathbf{t}}\frac{\partial \mathbf{t}}{\partial \boldsymbol{\xi}}. \tag{3.13}$$

The strains ϵ, γ, and the buckling quantity r result from the cross-sectional modeller. The buckling quantity r is coupled with the full set of design variables using

the local **A** matrix, **D** matrix, and the laminate thickness **t**, because these local quantities determine the mechanical properties of the skin and the spars and as such, the buckling behaviour.

TIP DEFLECTION: The maximum deflection is calculated using the iterative method shown in Figure 2.17; the static equilibrium condition, Equation 2.43, determines the iterated value for deflection distribution of the blade and as such, the tip deflection is a sub set of the displacement vector. For the gradient, the sensitivities of the cross-sectional properties **C** with respect to the **ABD** matrix are required. Furthermore, sensitivity information of the beam degrees of freedom **p** with respect to the cross-sectional properties must be determined, as well as the blade position **x** with respect to the beam degrees of freedom. Subsequently, the response sensitivity of the blade deflection with respect to the design variables is determined as:

$$\frac{\partial \mathbf{x}}{\partial \boldsymbol{\xi}} = \frac{\partial \mathbf{x}}{\partial \mathbf{p}} \left(\frac{\partial \mathbf{p}}{\partial \mathbf{C}} \left(\frac{\partial \mathbf{C}}{\partial \mathbf{A}} \frac{\partial \mathbf{A}}{\partial \boldsymbol{\xi}} + \frac{\partial \mathbf{C}}{\partial \mathbf{D}} \frac{\partial \mathbf{D}}{\partial \boldsymbol{\xi}} \right) + \frac{\partial \mathbf{p}}{\partial \mathbf{t}} \frac{\partial \mathbf{t}}{\partial \boldsymbol{\xi}} \right). \tag{3.14}$$

For the sake of clarity it should be noted that the sensitivities $\partial \mathbf{C}/\partial \mathbf{A}$ and $\partial \mathbf{C}/\partial \mathbf{D}$ contains information about the transformation between the 3 dimensional laminates and the 1 dimensional section properties. The sensitivity $\partial \mathbf{p}/\partial \mathbf{C}$ indicates the relation between a change in beam deformation due to a change in the local section properties and the sensitivity $\partial \mathbf{p}/\partial \mathbf{t}$ contains information about the beam deformation due to a change in local thickness at the beam element location considered.

AERODYNAMIC POWER LOSS: The aerodynamic power is calculated with Equation 2.41. The power calculated must not fall below a predefined minimum value. Since the power of the most critically loaded blade is considered, the minimum power is calculated using the appropriate part of the atmospheric wind profile and a reduction factor is applied to account for the minimum power constraint. This will be explained further during the presentation of the numerical values of the constraints in the next paragraph. The sensitivities are determined using the aerodynamic normal and tangential force derivatives. They originate from the lift and drag force vectors and the convenient components are selected for the contributions in the plane of rotation, in which the normal force and the tangential force are defined. The response sensitivity for the optimisation is written as:

$$\frac{\partial P}{\partial \boldsymbol{\xi}} = \frac{\partial P}{\partial \mathbf{C}} \left(\frac{\partial \mathbf{C}}{\partial \mathbf{A}} \frac{\partial \mathbf{A}}{\partial \boldsymbol{\xi}} + \frac{\partial \mathbf{C}}{\partial \mathbf{D}} \frac{\partial \mathbf{D}}{\partial \boldsymbol{\xi}} \right) + \frac{\partial P}{\partial \mathbf{t}} \frac{\partial \mathbf{t}}{\partial \boldsymbol{\xi}}, \tag{3.15}$$

in which the derivative of the aerodynamic power to the cross-sectional tensor **C** is written as:

$$\frac{\partial P}{\partial \mathbf{C}} = \frac{\partial P}{\partial \mathbf{p}} \frac{\partial \mathbf{p}}{\partial \mathbf{C}}, \tag{3.16}$$

and for the thickness vector $\mathbf{t}$:

$$\frac{\partial P}{\partial \mathbf{t}} = \frac{\partial P}{\partial \mathbf{p}} \frac{\partial \mathbf{p}}{\partial \mathbf{t}}. \tag{3.17}$$

The aerodynamic power change with respect to the beam degrees of freedom is the common sensitivity to be determined, the derivatives of the beam shape with respect to the local cross-sectional properties and thickness already have been described. The derivative $\partial P/\partial \mathbf{p}$ follows from the definition of the aerodynamic power, as defined in expression 2.41. The sensitivity with respect to the beam degrees of freedom then becomes:

$$\frac{\partial P}{\partial \mathbf{p}} = \Omega \sum \left(\left(\frac{\partial \mathbf{L}_i}{\partial \mathbf{p}} + \frac{\partial \mathbf{D}_i}{\partial \mathbf{p}} \right) \cdot \boldsymbol{\mathcal{R}}_0 \mathbf{r}_i + (\mathbf{L}_i + \mathbf{D}_i) \cdot \boldsymbol{\mathcal{R}}_0 \frac{\partial \mathbf{r}_i}{\partial \mathbf{p}} \right). \tag{3.18}$$

Assuming that the blade deformation in spanwise direction is sufficiently small, the sensitivity $\partial \mathbf{r}_i/\partial \mathbf{p}$ is neglected. In this case the resulting velocities are assumed to act at the undeformed blade radial stations and Equation 3.18 reduces to:

$$\frac{\partial P}{\partial \mathbf{p}} = \Omega \sum \left(\frac{\partial \mathbf{L}_i}{\partial \mathbf{p}} + \frac{\partial \mathbf{D}_i}{\partial \mathbf{p}} \right) \cdot \boldsymbol{\mathcal{R}}_0 \mathbf{r}_i. \tag{3.19}$$

The sensitivities as defined above determine the direction of the constraint functions when the design variable vector is altered. As an example, the aerodynamic power moves in a direction as estimated in the following expression:

$$\Delta P = \frac{\partial P}{\partial \boldsymbol{\xi}} \Delta \boldsymbol{\xi}. \tag{3.20}$$

Similar to the objective function direction, the changes in the constraint functions are added to a previous value. As long as the prescribed values for the constraints are not reached, the direction of the design variables vector is on the right track; otherwise, the direction should be changed.

NUMERICAL VALUES OF CONSTRAINTS: The numerical values for the blade constraints are given in Table 3.2 with the remark that the values are valid for the heaviest loaded blade, which is in the vertically upward position acting in a wind field under extreme wind shear conditions. The values for the strain and the

buckling load are relative values and are defined as the ratio between the critical value and the actual value as defined in the work of [Werter, 2017]. The blade tip deflection constraint values are taken from the work of [Ashuri, 2012].

The definition of the power loss constraint is slightly more arbitrary. It is obvious that blade deformation causes some power loss with respect to the basic power curve. It has been decided to allow a certain loss of aerodynamic power instead of including the power as an extra objective function and minimising the power loss simultaneously with the mass optimisation.

Table 3.2: Constraints for wind turbine blade structural optimisation, when the blade is in the vertically upward position and extreme shear is assumed. In this position the blade generates excessive amounts of power.

	5 MW	10 MW	20 MW
strain [-]	1	1	1
buckling [-]	1	1	1
tip deflection [m]	6	7.9	11.9
minimum power [MW]	3.42	7.21	14.1

During the trial optimisation procedure, the power loss constraint appeared to have a significant influence on the optimised blade mass. Moreover, the combination of the constraints tip deflection and power loss is a difficult one, especially when a certain amount of tip deflection is allowed and power loss is not. Because of the reason mentioned above, a power loss constraint has been introduced. The proposed power limits are shown in Table 3.2. These values are based on the fact that for the extreme wind shear case, the vertically upward blade generates approximately 75% of the total turbine power. For normal production, due to aeroelastic tailoring effects, some power loss should be allowed; the question then is: what about the yearly power production?

For the yearly power production, a normal wind profile is assumed. Furthermore, the power loss of 10% is assumed for the extreme wind shear case and might be overestimated for the normal wind profile case. As such, a loss of 5% is assumed for the power production calculation; for the yearly power production, the turbine generates 95% of its rated power. To estimate the year production the probability distribution of the wind speeds is required and the power curve. Using a power production calculation tool of [van Bussel, 2010], assuming a Weibull probability distribution with shape parameter $k = 2$ and the power curve of the NREL 5MW reference machine, the generated results are shown in Figure 3.3. The year production is based on a land site with an average 10m year velocity of 7.4 m/s and a roughness length $z_0 = 0.01$ to approximate a sea climate. From Figure 3.3 one observes a relatively small decrease in production above rated: for a power loss of 5% a yearly power production loss of only 2.6% is determined.

In chapter 4 the production losses are discussed in more detail.

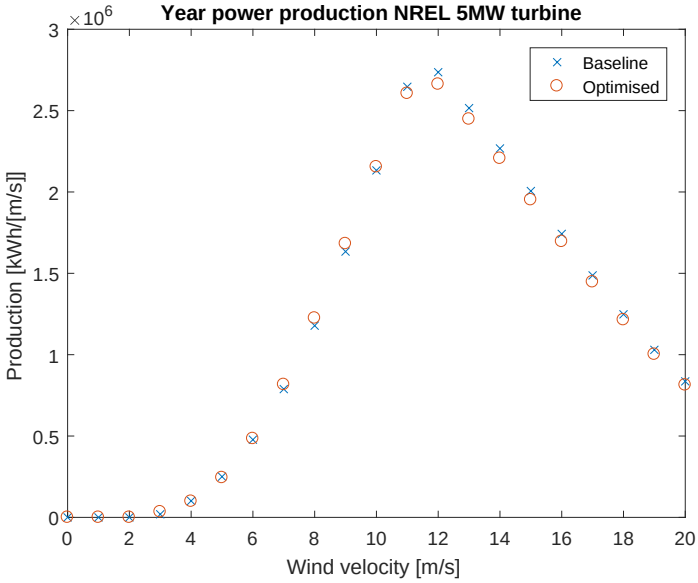

Figure 3.3: Year power production of based on power curve and 95% of the power curve.

LAMINATE FEASIBILITY: As a final note, it should be mentioned that the use of lamination parameters as design variables requires an extra constraint that couples the **A** and the **D** matrix in terms of laminate feasibility. Since lamination parameters are independent parameters within the design variable vector it is important to check whether the **A** and **D** matrix resulting from the lamination parameters generate a feasible laminate. For instance, using lamination parameters could generate laminates that have negative stiffnesses. Since stiffnesses are always positive, an additional constraints should prevent this behaviour. For a feasibile design space, [Hammer et al., 1997] derived a set of closed form expressions in terms of the in-plane, coupling, and bending lamination parameters separately:

$$\begin{aligned} 2{V_1}^2\left(1-V_3\right)+2{V_2}^2\left(1+V_3\right)+{V_3}^2+{V_4}^2-4V_1V_2V_4 &\leq 1 \\ {V_1}^2+{V_2}^2 &\leq 1 \\ -1 \leq V_i &\leq 1. \end{aligned} \tag{3.21}$$

As can be seen from equations 2.4, there is also a relation between the in-plane stiffness and the out-of-plane stiffness of a laminate. So, another constraint should be that the out-of-plane behaviour of the laminate is consistent with the in-plane stiffness behaviour. Such constraints are implemented following the work of [Werter, 2017], including the sensitivities with respect to the design variables.

3.3 THE WIND TURBINE BLADES CONSIDERED

For the study of structurally optimised blade designs, the single blades of a 5MW, 10MW and a 20MW wind turbine are considered. For the aerodynamic load distribution, the chord length and twist angle as a function of the blade radius are used obtained from aerodynamic shape optimisations as found in [Jonkman et al., 2009], which is already visualised in chapter 2. The 10MW blade information is obtained from [Bak et al., 2013]. The blade shape information is summarised in Table 3.3 and a visual representation of the blade is shown in Figure 3.4.

Table 3.3: Blade twist- and chord distribution as a function of the blade radius for the 10MW RISØ reference blade.

Blade radius [m]	Blade twist [deg]	Blade chord [m]	Airfoil type
2.0	-14.5	5.38	Circular
5.4	-14.5	5.38	Circular
17.0	-12.5	6.03	Circular
26.8	-7.5	6.13	FFA-W3-360
32.7	-6.0	5.84	FFA-W3-360
42.1	-4.9	5.16	FFA-W3-301
51.6	-2.5	4.35	FFA-W3-301
60.8	-0.5	3.57	FFA-W3-301
71.7	0.9	2.73	FFA-W3-241
80.0	2.4	2.12	FFA-W3-241
85.1	3.25	1.39	FFA-W3-241
85.7	3.3	1.14	FFA-W3-241

The 20MW data is obtained from [Peeringa et al., 2011] and the shape is summarised in Table 3.4. To get an idea of the blade planform, the visual representation of the blade can be found in Figure 3.5. For the 20MW blade, it can be observed that a third spar has been added to prevent buckling of the trailing skin of the root region of the blade. The prescribed chord, twist, and airfoil distribution are used as input for the blade shape, the optimiser will determine the lay-up and core thickness starting at an initial condition, which in case of thickness is approximated by a linearly decreasing function in tipward direction and a quasi-isotropic lay-up.

AERODYNAMIC CONVERGENCE STUDY OF THE BASELINE BLADE DESIGN

In chapter 2 the discrete aerodynamic modelling procedure was explained. In this paragraph, results are presented about the number of aerodynamic panels on the bound blade surface and in the wake for reliable optimisation results, computed in an efficient way. The number of chordwise panels is of quite some influence on the aerodynamic power, as can be observed from Figure 3.6. The power shows convergence for 8 panels or more. For the use in the aeroelastic model and the

Table 3.4: Summary of blade twist- and chord distribution as a function of the blade radius for the 20MW ECN reference blade.

Blade radius [m]	Blade twist [deg]	Blade chord [m]	Airfoil type
3.0	-13.5	7.084	Circular
13.4	-13.5	7.2068	Circular
25.4	-13.3843	9.1693	DU00-W2-401
39.4	-8.4588	8.4913	DU97-W-300
59.4	-5.054	6.5294	DU93-W-210
79.4	-3.4615	5.3501	NACA64618
95.4	-1.9971	4.6846	NACA64618
107.4	-1.1403	4.0899	NACA64618
119.4	-0.2206	3.2943	NACA64618
126.0	0.0001	0.6725	NACA64618

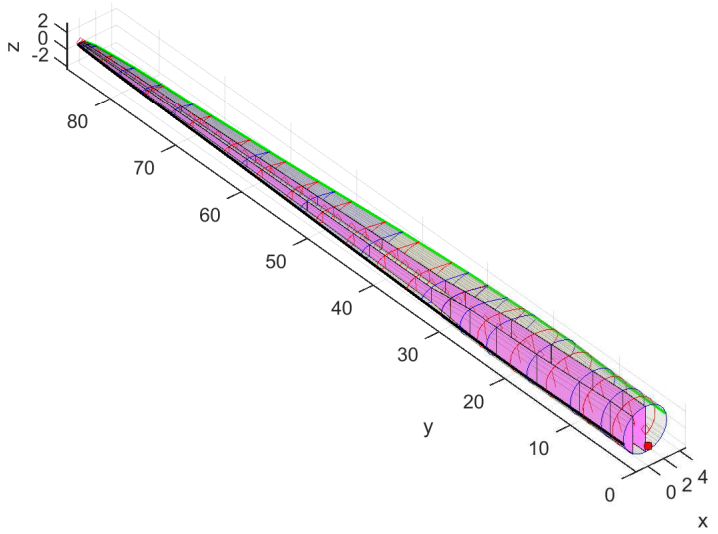

Figure 3.4: Three dimensional representation of the 10MW RISØ blade

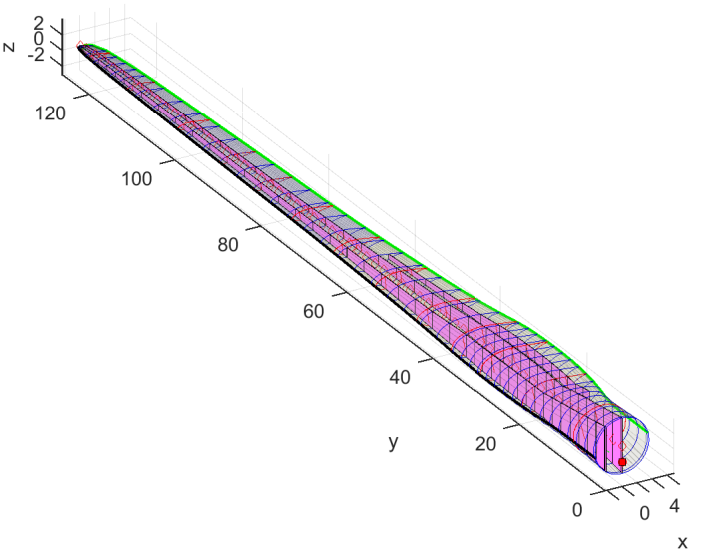

Figure 3.5: Three dimensional representation of the 20MW ECN blade

structural optimisation, 8 chordwise panels take too much computational effort. It has been shown in Figure 2.19 that at least 2 chordwise panels should be used to approximate the normal force results from the blade-element momentum theory. Using multiple panels in the chordwise direction creates the possibility of modelling camber, which improves the result for the normal force. In this research, the minimum amount of 2 panels has been chosen. This choice generates an error of approximately 10%, but for structural layout trend purposes, it is assumed that significant structural behaviour will be observed anyway. Furthermore, it was shown that the aerodynamic power is quite insensitive to the number of panels in spanwise direction; increasing the number of chordwise panels form 8 via 16 to 32 gives less than 1 per cent change in power, see figure 3.6.

The wake has a similar discretisation in spanwise direction but the chordwise wake panel dimension does not necessarily have to be equal to the blade chord dimensions. A convergence study shows that the aerodynamic power approaches a limit when increasing the number of wake rotations by multiples of 2, starting at 1 and ending at 16, see Figure 3.7. One could observe that the step from 4 to 8 and 16, does not add that much to the aerodynamic power.

For this reason, 4 wake rotations were assumed. Together with 8 spanwise panels and 20 azimuthal panels the steady case for constructing the influence coefficients matrix $\mathbf{A}$ is defined.

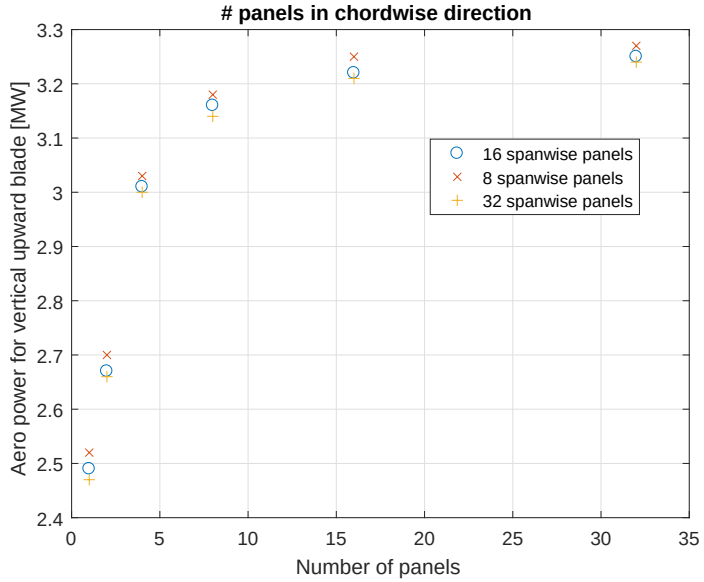

Figure 3.6: Behaviour of aerodynamic blade power as a function of blade span panel distribution and chordwise panel distribution.

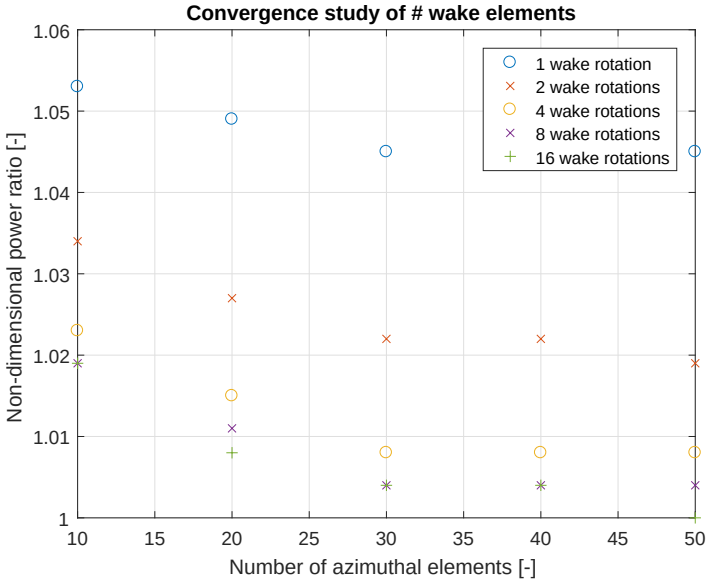

Figure 3.7: Convergence behaviour of number of azimuthal elements and number of wake rotation behind rotor.

3.4 CONCLUDING REMARKS

As preparation for the optimisations, the load cases NWP and EWS have selected as well as the baseline blades. Since the aeroelastic model is designed for the steady aerodynamic case, the selected load cases are chosen to be the normal wind profile and, to account for a more severe load case, the extreme wind shear case. Both cases are considered up to rated power or rated wind speed. The blades were chosen to be the 5MW NREL reference blade as a baseline, the 10MW preliminary design of RISØ, and the preliminary design of the 20MW from ECN. The preliminary designs or reference blades were considered to be the baselines for the 10MW and 20MW respectively.
Then, the optimisation framework was explained. For the stiffness optimisation, where the objective is chosen to be the minimum blade mass, it is essential to define the objective function as a function of the design variables. The design variables are the lamination parameters and laminate thickness for a pure fibre-epoxy laminate. The sandwich laminate design variables are defined by the lamination parameters of the face sheet, the thickness of the face sheet, and the thickness of the core. For the gradient-based optimisation, the GCMMA procedure is selected. As a consequence, the response sensitivity of the objective mass must be defined with respect to the design variables. The selected constraints are strain, skin and spar buckling, laminate feasibility, and aerodynamic power loss of which the numerical values are selected as well. In addition, the response sensitivities of the constraints with respect to the design variables must be found as well, in order to relate the constraints to the design variable vector. Finally, an aerodynamic convergence study on the number of blade and wake panels for the baseline blade design was performed. For finding structural layout trends using a gradient-based optimisation, 2 chordwise blade panels, 8 spanwise blade panels, 20 azimuthal wake panels, and 4 wake rotations were assumed.

4

Aeroelastic optimisation results of 5, 10 and 20MW blades

In this chapter, the static aeroelastic optimisations of several wind turbine blades are performed. First, it is shown that the extreme wind shear load case generates heavier blades compared to the normal wind profile case. Then, using the blade mass as the objective function, the selected constraint variables and the design variables under the extreme wind shear static load case for 5MW, 10MW and 20MW rotor blades are considered for three different structural configurations:

- a full sandwich composite blade;
- a sandwich composite blade except for the spar caps - state-of-the-art design standard;
- a stiffened skin wing box design - besides the spars also inclusion of ribs and a stiffened, pure fibre-epoxy laminate skin.

In Figure 4.1 the structural configurations for the optimisations are summarised.

The optimisations are performed for a quasi-isotropic lay-up for model verification and tailoring is applied using the variable stiffness concept for mass minimisation. Furthermore, the effect of mixed materials in a blade is taken into account. Since

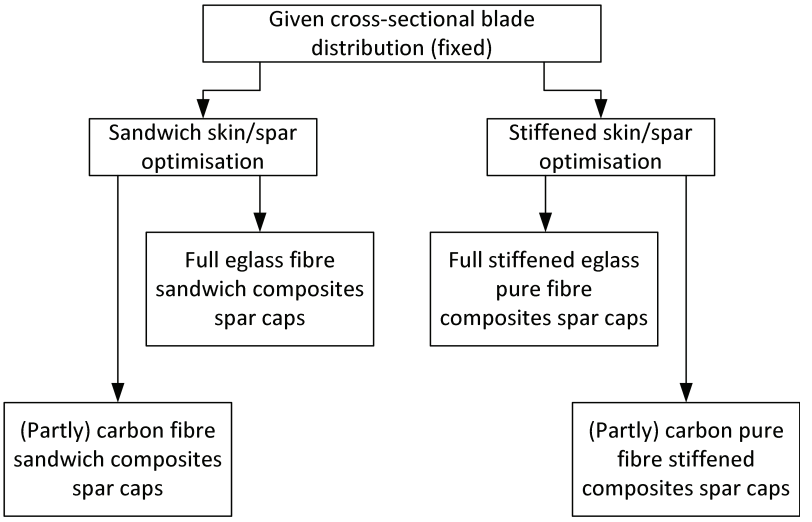

Figure 4.1: Schematic of the structural configurations to be optimised.

it is expected that the highest stress occurs in the spar caps, only this blade part is varied in percentage carbon-epoxy versus eglass fibre-epoxy laminates. The goal of the optimisation is to find possibilities of reducing mass under the given constraints and to discover new trends in the structural layout of the blades: for the different structural solutions, the relation between blade mass and the nominal turbine power is visualised to observe the effect of mass minimisation using the variable stiffness concept for adapting, for instance, the existing upscaling laws. The chapter is structured as follows: first, the sandwich composite blade optimisations are performed, then the skin-stiffened blade optimisations are carried out after which the blade designs are compared in terms of blade mass. The chapter ends with a discussion and conclusions about the trends discovered from the optimisations.

4.1 Sandwich Structural Configuration

In this section, the sandwich composite blade optimisations are performed. For state-of-the-art blades, the leading edge part, trailing edge part and the spars are sandwich panels, the upper and lower spar caps are pure laminates. For the optimisation, however, it is more convenient to model the full skin with sandwich composite material, referred to as the full sandwich blade. For this full sandwich blade, the skin is modelled as a continuous sandwich panel and is divided into three chordwise panels: in this manner, the cross-section is partitioned in a leading

edge part, a box beam part and a trailing edge part. Since the assumption for the sandwich is that the stresses act in the faces of the laminate and not in the core, see chapter 2, the core material will only be of use for buckling sensitive locations, so there probably will be core material in the spar caps. If the optimiser indicates that the laminate is moving towards unidirectional behaviour this means that the optimisation itself is moving in the right direction. Manufacturers can decide to replace the core material by the same unidirectional composites as used for the face sheets, as in the state-of-the-art blades. Since the load is mainly carried by the face sheets and the thickness of the suction spar cap is mainly determined by the buckling behaviour due to compression, this gives a heavier blade which is presented in this chapter for the 5MW sandwich blade. The material mass and stiffness properties for the sandwich blade are given in Table 4.1:

Table 4.1: Material mass and stiffness properties sandwich blade

material	E_{11} [GPa]	E_{22} [GPa]	G_{12} [GPa]	ν -	mass [kg/m^3]
eglass (face sheet)	40	8.33	4.20	0.27	1850
Carbon (face sheet)	83	8.5	4.14	0.35	1452
foam (core)	0.256	0.256	0.022	0.3	200

The material allowables are given in Table 4.2:

Table 4.2: Material allowables sandwich blade

material	X_t [MPa]	X_c [Mpa]	Y_t [MPa]	Y_c [MPa]	S [MPa]
eglass (face sheet)	392	300	40	62	41
Carbon (face sheet)	2280	1725	57	228	76

4.1.1 5MW Blades

Results of full sandwich laminates

Before performing the optimisations for the static aeroelastic case, the critical load case must be selected. During this research the focus was the normal operation interval just below rated power, to avoid triggering the blade collective pitch mechanism. On the other hand, when a collective pitch action might occur due to a slightly above-rated wind velocity, the aerodynamic loading and the power generated are still physically correct, so no problems arise in the optimisation procedure. Furthermore, the optimisation has been carried out for the eglass sandwich composite blade since the focus is proving that the EWS load case is critical, using a different material is of no significance yet.

Loadcase I: Normal Wind Profile (NWP): The stiffness and thickness plots in Figures 4.2, 4.3 and 4.4 show results for the normal wind profile case. Specific-

ally, for the 5WM blade, the normal wind profile has been selected as an optimisation case for comparison with the extreme wind shear case to verify whether this extreme load case indeed shows a significant increase in blade mass. From Figure 4.2 the thickness of the suction skin clearly shows the critical buckling locations, while the pressure skin only is loaded in tension and shear. The spar cap stiffness distribution shows the same: the lay-up has transformed towards nearly unidirectional. The suction side leading part of the skin resists torsional deformations and some buckling, but from the thickness distributions, it can be concluded that leading edge parts are not as critical as the load carrying spar caps. The trailing edge part stiffness distribution is also meant to resist buckling in the interval between 0 and 30 meters blade span. This buckling sensitivity is indeed shown by purple colours in the suction skin; purple indicates a significant thickness value indicating this increased skin buckling sensitivity.

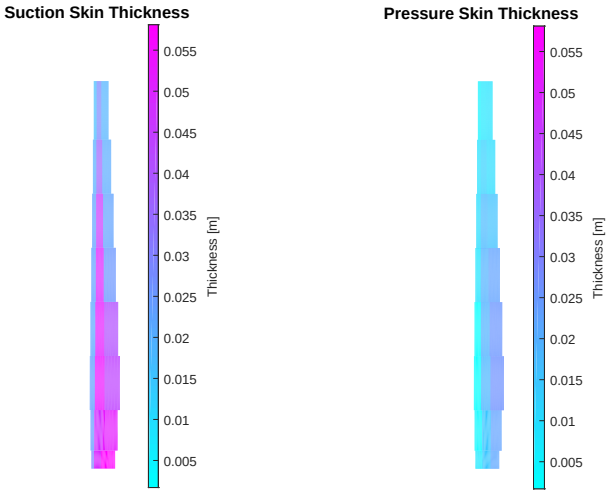

(a) Suction skin **(b)** Pressure skin

Figure 4.2: Tailored skin thickness distribution of the 5MW eglass blade for the NWP case.

The pressure side of the blade is clearly loaded in tension due to the unidirectional stiffness distribution across the blade span in the leading edge part and the spar cap, which can be read from Figure 4.3. It should be noted that the leading edge stiffness plots have a little contribution in the chordwise direction, thus, lose some of the unidirectional behaviour to account for torsional loading as well. The trailing part is loaded in a different way, which has its result in the optimum lay-up for resisting shear more than tension. As a final note, the pressure side thicknesses are in general less than the top skin values. The suction side is more

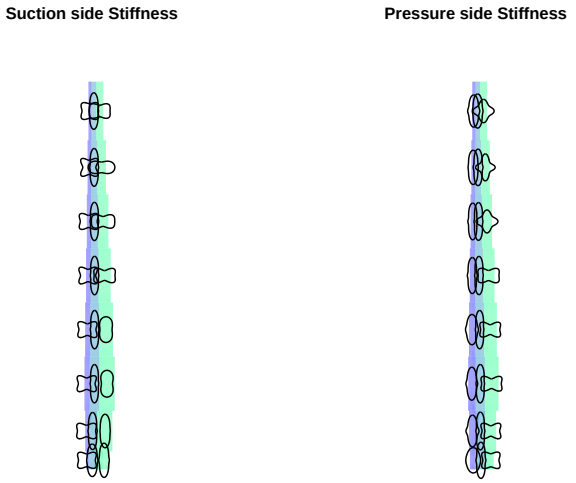

(a) Suction skin **(b)** Pressure skin

Figure 4.3: Tailored skin stiffness distribution of the 5MW eglass blade for the NWP case.

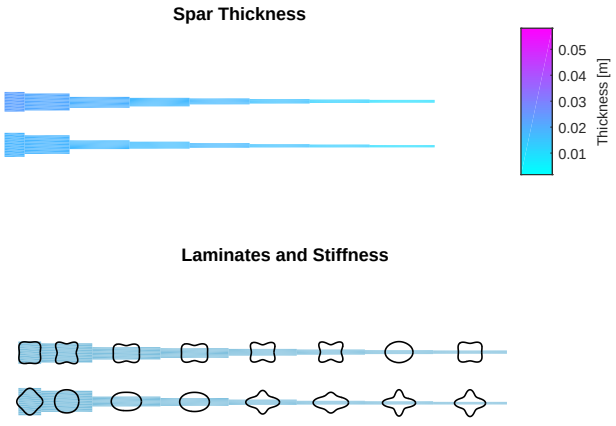

Figure 4.4: Spar thickness and stiffness distribution of the 5MW eglass blade for the NWP case. Upper: spar thickness distribution, lower: spar stiffness distribution.

sensitive to buckling which requires a higher thickness, the tensile stresses in the pressure side are not a problem for the sandwich composite skin resulting in lower overall thickness.

The front and rear spar lay-ups are generally shear resistant solutions, see Figure 4.4. The stiffness distribution has been optimised towards a typical shear loaded case for the front spar; the rear spar solutions move towards principal directions, following the blade axis. The spar thickness distributions for the front or rear location are similar, which is not uncommon when realizing that the elastic axis approximately coincides with the centre line of the narrow box spar. It should be noted, however, that the rear spar tends to a slightly thinner thickness distribution.

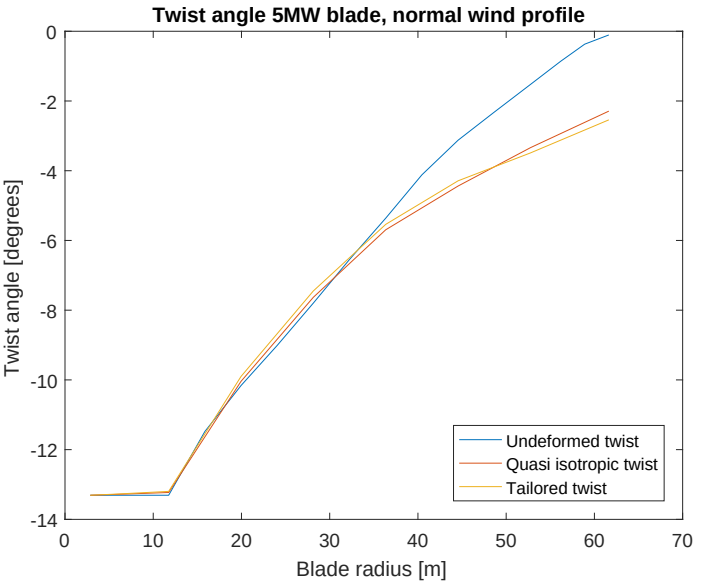

Figure 4.5: Twist distribution for the 5MW blade for the NWP load case at a wind speed of 11.4 m/s. The fully tailored blade is compared with the quasi isotropic lay-up discussed in Chapter 2. and the undeformed blade.

As a result of the optimisations, the elastic twist deformation of the beam representation of the blade is compared to the undeformed blade twist or the so-called built-in twist. From Figure 4.5 this comparison shows that the quasi-isotropic optimisation, a validation case that has been discussed in Chapter 2, and the fully tailored blade show a similar twist distribution which indicates that the torsional stiffness of the tailored design has not changed significantly. With the constraint on the tip displacement, the flapwise stiffness distribution change is limited as well. Since the anisotropic lay-up could introduce twist due to bending, but this bend-twist coupling is limited by the tip displacement constraint.

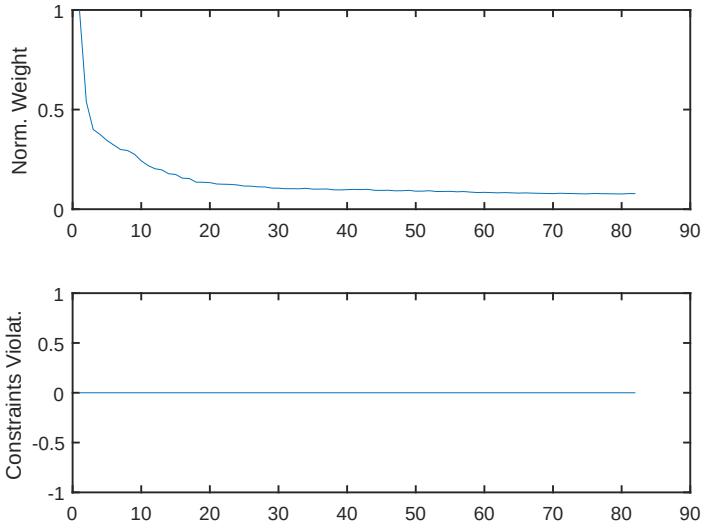

Figure 4.6: Objective and constraints against number of outer iterations of eglass 5MW blade for the NWP case.

For the NWP load case, the optimum blade mass is 7900 kg, the convergence history has been plotted in Figure 4.6, together with the constraints violations. The iteration loop is ended when the convergence criterion has been reached and the maximum strain or the maximum buckling have reached the value of approximately 1 or if the constraints have converged to a lower value. The blade mass sensitivity approaches zero and the optimization stopped since the mass approaches its converged value. It should be noted that a quasi-isotropic lay-up resulted in an optimised mass of 12100 kg. This mass is significantly below the baseline blade design mass of 17700 kg, which already indicates that the normal wind profile generates a blade that probably fails in extreme load cases.

LOADCASE II: EXTREME WIND SHEAR (EWS) The extreme wind shear case generates a similar lay-up distribution across the blade span for the suction and pressure skin and both the spar webs, comparing Figures 4.10 and 4.12 to Figures 4.3 and4.4. The difference is to be found in the thickness distribution as shown in Figures 4.7 and 4.8. For the suction side spar caps, it is curious that the maximum thickness is lower for the quasi-isotropic lay-up, as compared to the tailored blade. On the other hand, this higher thickness is present for the spar cap and the leading edge part of the quasi-isotropic case, while the tailored case shows the high thicknesses for the spar caps only. Furthermore, high thicknesses are observed at the trailing part of the blade between the root and 33% of the

span due to buckling constraints.

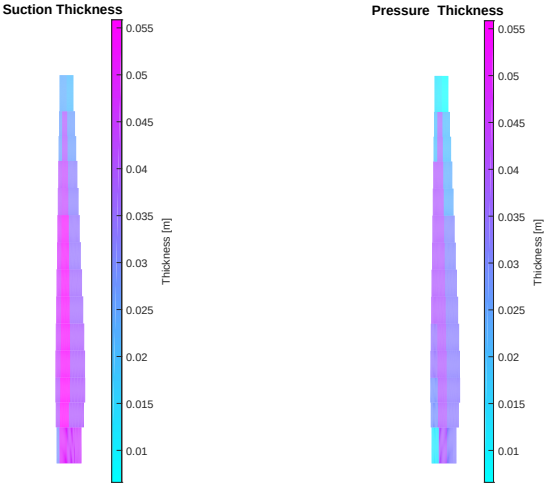

(a) Suction skin. **(b)** Pressure skin.

Figure 4.7: Skin thickness distribution of quasi-isotropic lay-up for the 5MW eglass blade for the EWS case.

From Figure 4.13, it can be observed that the quasi-isotropic lay-up and the fully tailored case show similar twist angle distributions which indicates that the torsional stiffness has not changed significantly as a consequence of tailoring. However, compared with the normal wind profile a slight increase in the elastic twist is detected, which could be an effect of the more severe extreme wind shear load case. It could also be that this extreme load case introduces more coupling between bending and twisting.

The converged solution shows a minimised blade mass of 9400 kg of the full tailored blade, which is significantly higher than the results from the normal wind case; this is an increase towards the design mass of the NREL 5MW rotor blade of 17700 kg. This again indicates that the aerodynamic modelling has been implemented correctly and the optimisation behaviour, Figure 4.14, is sound as well. Compared to the normal wind profile, the extreme wind shear is clearly the heaviest load case. Further optimisations are performed using the EWS case.

Note that Figure 4.8 and Figure 4.9 show the optimisation results of the total skin thickness only. Therefore, it is important to consider the structure of the sandwich laminates, especially for the spar caps because they determine a significant part of the blade mass. Remembering that the sandwich composite has been assumed for the complete blade skin and spars, as such, the spar caps also could contain

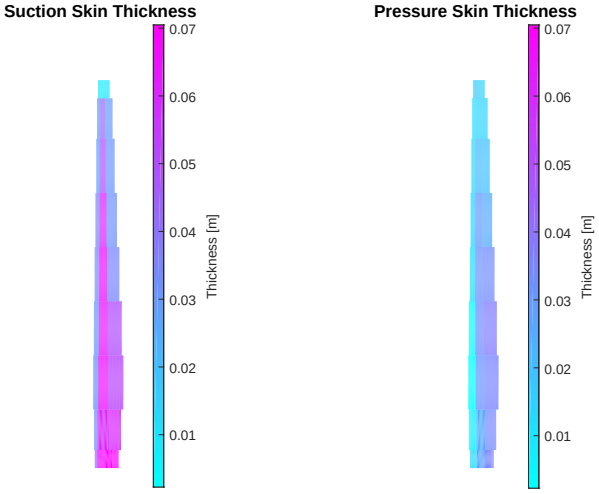

(a) Suction skin. **(b)** Pressure skin.

Figure 4.8: Skin thickness distribution tailored for the 5MW eglass blade for the EWS case.

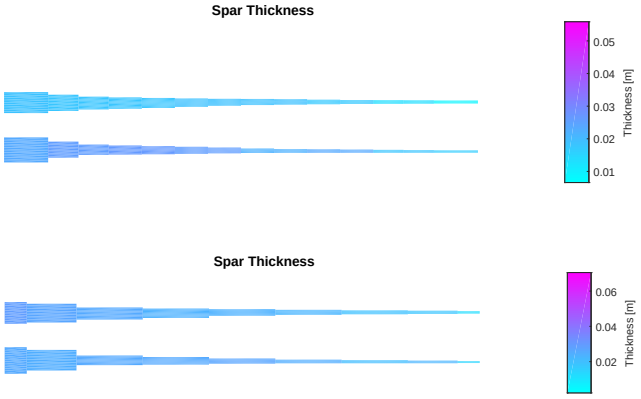

Figure 4.9: Spar thickness distribution of the 5MW eglass blade for the EWS case. Upper: quasi-isotropic, lower: tailored.

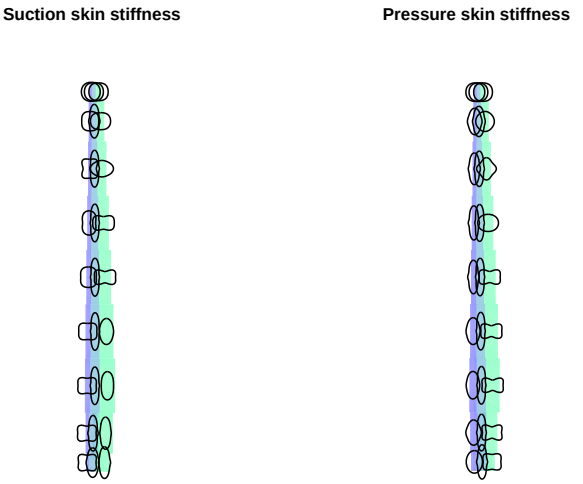

(a) Suction skin **(b)** Pressure skin

Figure 4.10: In-plane skin stiffness distribution of the 5MW blade for the EWS case.

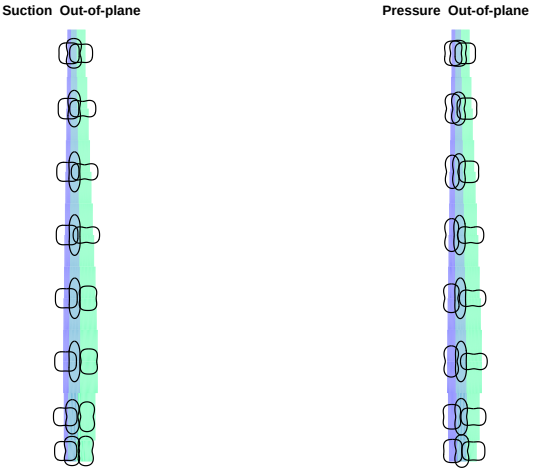

(a) Suction skin **(b)** Pressure skin

Figure 4.11: Out-of-plane skin stiffness distribution of the 5MW eglass blade for the EWS case.

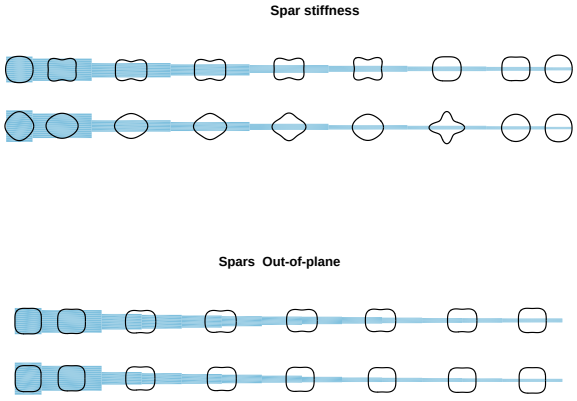

Figure 4.12: Spar stiffness distribution of the 5MW eglass blade for the EWS case. Upper: in-plane stiffness distribution, lower: out-of-plane stiffness distribution.

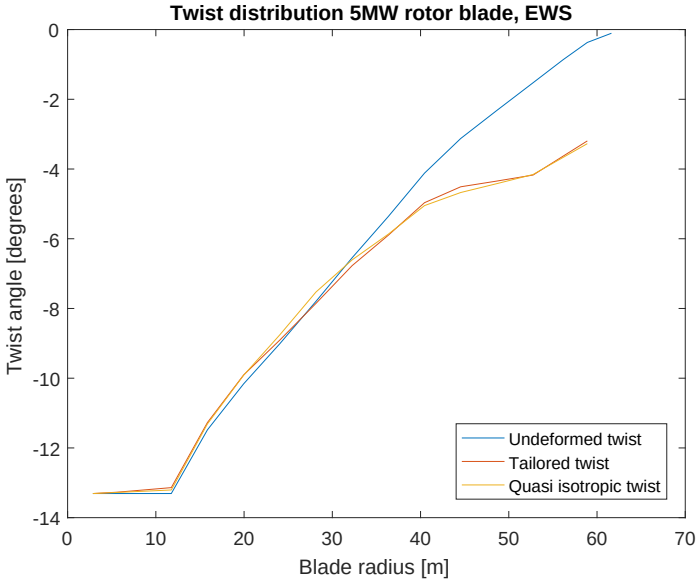

Figure 4.13: Twist distribution for the 5MW blade for the EWS load case.

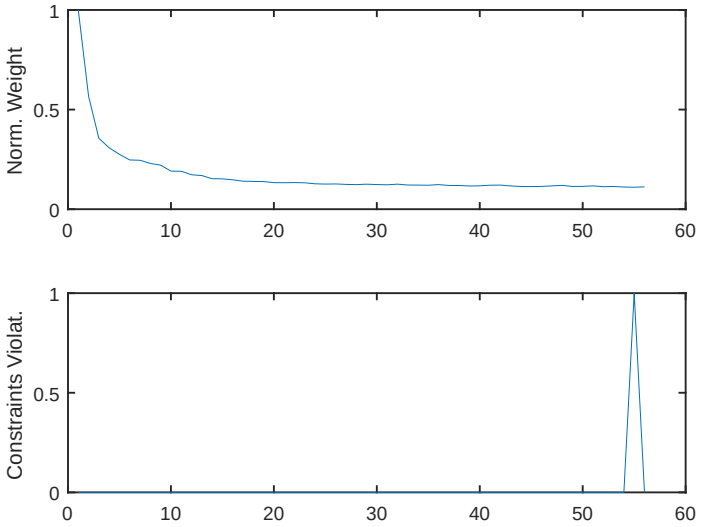

Figure 4.14: Objective and constraints against number of outer iterations of the 5MW eglass blade for the EWS case.

core material. The optimiser shows a significant amount of core material in the suction skin while the core material presence is reduced to almost zero in the pressure side of the blade. Since the spars and the suction side of the blade are subjected to buckling as well, the core material prevents buckling due to the simplified stress-strain formulation of the sandwich laminates. Figures 4.15, 4.16, and 4.17 show the ratio between the face sheets and the core and the total spar cap thickness distribution respectively.

RESULTS PARTIAL USE OF SANDWICH LAMINATES

Considering Figure 4.7 and Figure 4.9 again, it should be realised that the optimisation results of the total skin thickness only are presented. The total sandwich laminate thickness shown can be decomposed in two facing sheet thicknesses and a core thickness. The suction side thickness distribution shows similarities with results from [Ferede, 2016] with the difference that for the spar caps only face sheets were assumed. Replacing the core material of the spar caps by pure fibre laminates results in a heavier blade design but approximates the baseline blade design thickness and lay-up distribution. Replacing the core material with glass fibre epoxy sheets would increase the mass significantly because the core thickness is necessary to account for local buckling. An optimisation where the core thickness of the suction skin is forced to approximately zero gives the following

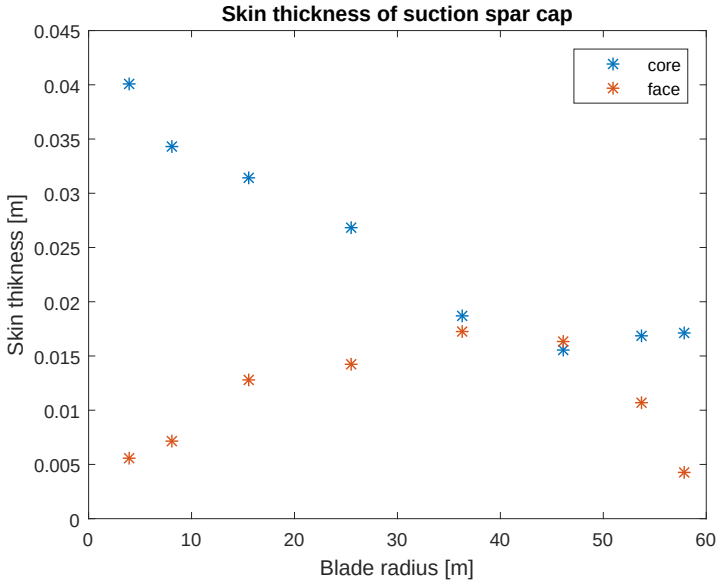

Figure 4.15: Suction skin thickness structure of the 5MW eglass blade for the EWS case. Spar cap core material thickness not constrained.

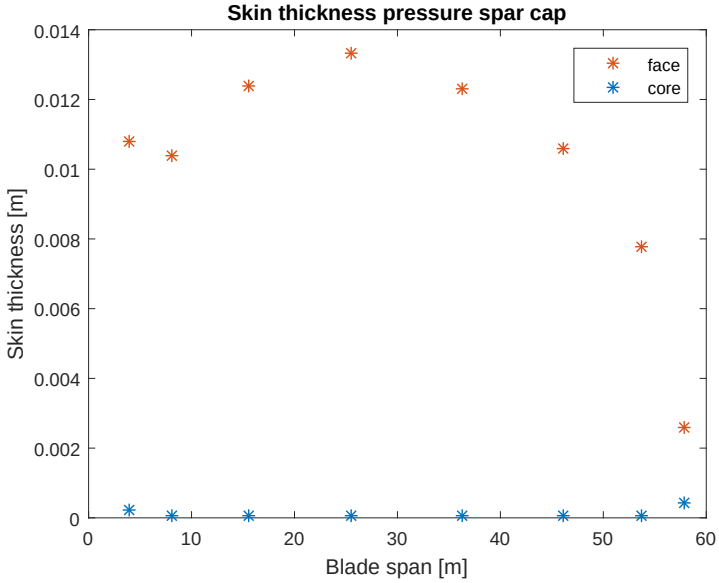

Figure 4.16: Pressure skin thickness structure of the 5MW eglass blade for the EWS case. Spar cap core material thickness not constrained.

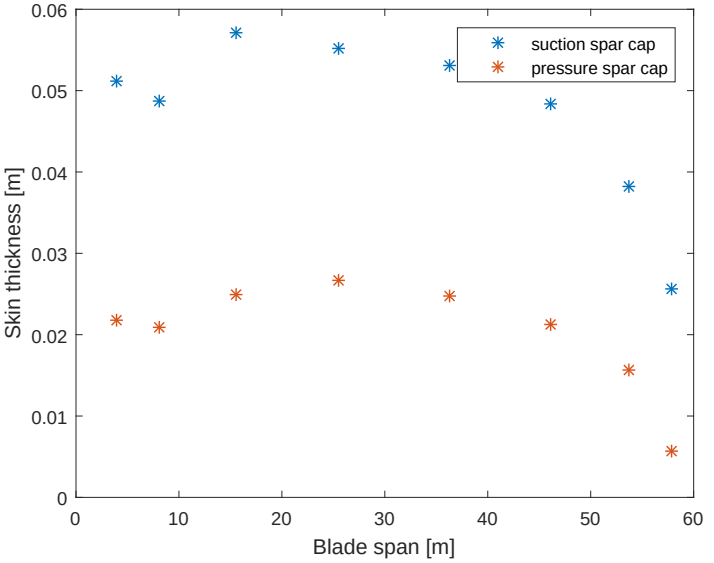

Figure 4.17: Total spar cap thickness distribution of the 5MW eglass blade for the EWS case. Spar cap core material thickness not constrained.

spar cap structure as shown in Figures 4.18, 4.19, and 4.20.

In addition, the Figures 4.18, 4.19, and 4.20 indicate that the suction side spar cap shows a similar thickness distribution as the case where the core material is present within the spar cap. The pressure spar cap face sheets become slightly thinner which gives a relative increase in the core material, still, the amount of core material can be considered not significant: the optimiser does not treat the core differently if the amount core material is forced to a minimum in the suction spar cap. Compared to a state-of-the-art blade, meaning that the spars consist of pure fibre composites in the spar caps, the total blade mass saving is 26%. Note that this percentage is based on two optimised designs: sandwich spar caps against pure fibre spar caps. This difference occurs only in the suction side spar cap due to buckling constraints. The pressure side spar cap still approximates a pure fibre laminate because buckling constraints are not active in this region.

4.1.2 10MW BLADES

Next, the 10MW blades are subject to a structural optimisation. Since the blade span is approximately 20 meters larger than the 5MW blade, it is expected that higher stresses occur in the laminates. In addition, the blade will be more sensitive to skin buckling. As such, higher skin thicknesses are expected, especially for the

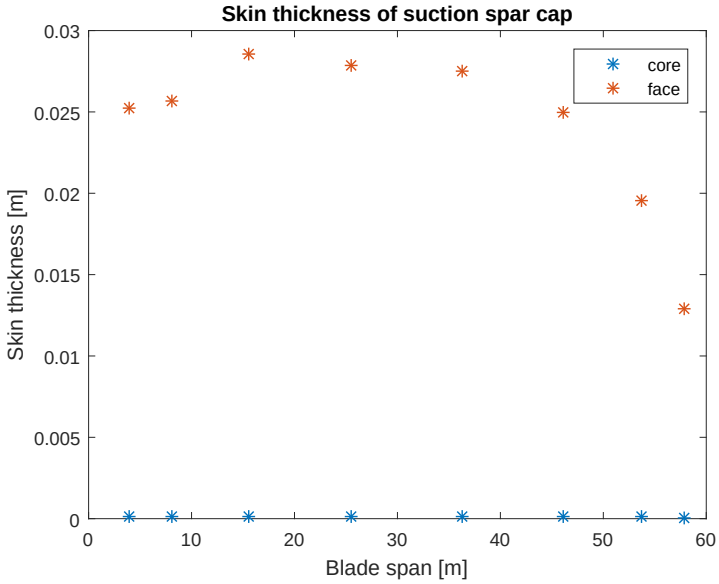

Figure 4.18: Suction skin thickness structure of the 5MW eglass blade for the EWS case. Spar cap core material thickness constrained towards approximately zero.

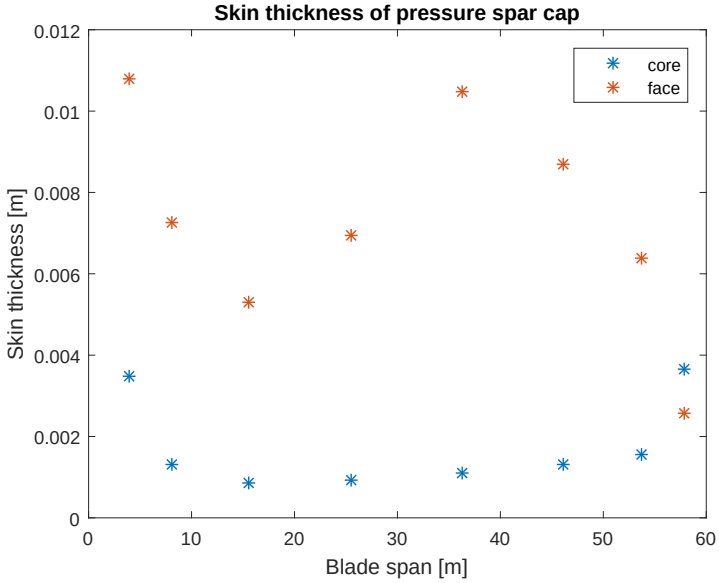

Figure 4.19: Pressure skin thickness structure of the 5MW eglass blade for the EWS case. Spar cap core material thickness not constrained.

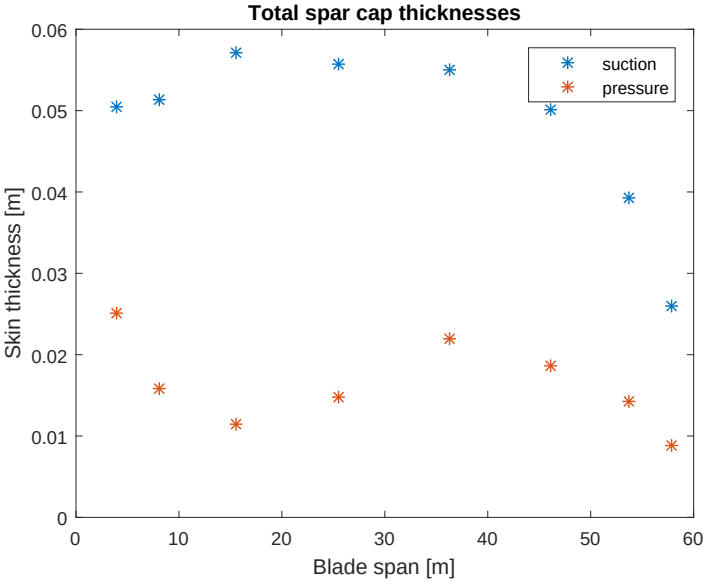

Figure 4.20: Total spar cap thickness distribution of the 5MW eglass blade for the EWS case. Suction skin core material thickness constrained towards approximately zero.

suction spar cap. In this section, the 10MW results are presented. First, the quasi-isotropic lay-up is compared with the tailored version for the EWS load case.

As observed in Figures 4.21, 4.22, and 4.23, the quasi-isotropic lay-up gives the overall highest thickness distribution. When tailoring is applied, the highest thickness reduces with approximately 10% with respect to the maximum quasi-isotropic thickness. Since this reduction has been accomplished across half the blade span, this gives a significant mass reduction compared to the quasi-isotropic lay-up. The lay-up is similar to the 5MW blade. The upper and lower spar caps show mainly unidirectional lay-up, while the leading edge and trailing edge parts of the suction and pressure sides show a variation of stiffness across the span, as shown in Figures 4.24 and 4.25.

Considering the spar cap layout, consisting of sandwich composites or full fibre composites, it is expected for the 10MW turbine blade to save additional mass as well. By choosing the same spar cap structure as the for the 5MW blade, an extra optimisation was performed with full-fibre spar caps. Optimisation results show a decrease of 14% in mass with respect to the state-of-the-art spar cap design due to the absence of core material. When sandwich composites are allowed for the spar caps, the optimiser adds some core material in the suction spar caps to account for local buckling and saves mass in comparison with the state-of-the-

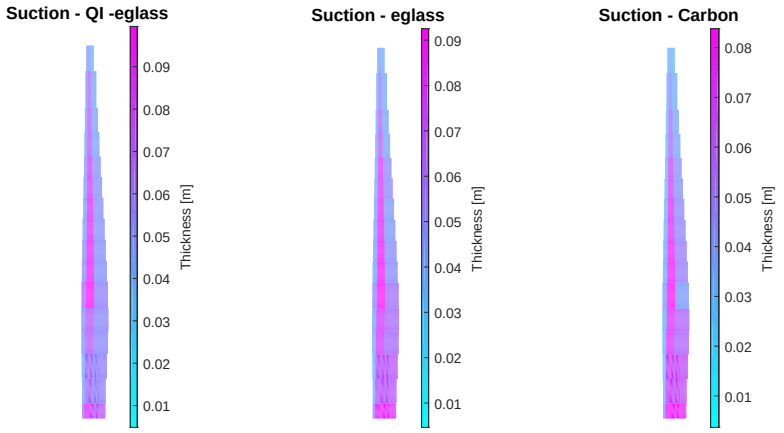

Figure 4.21: Skin thickness distribution suction side for 10MW blade. Left: quasi-isotropic eglass, centre: tailored eglass, right: tailored with carbon fibre spar cap.

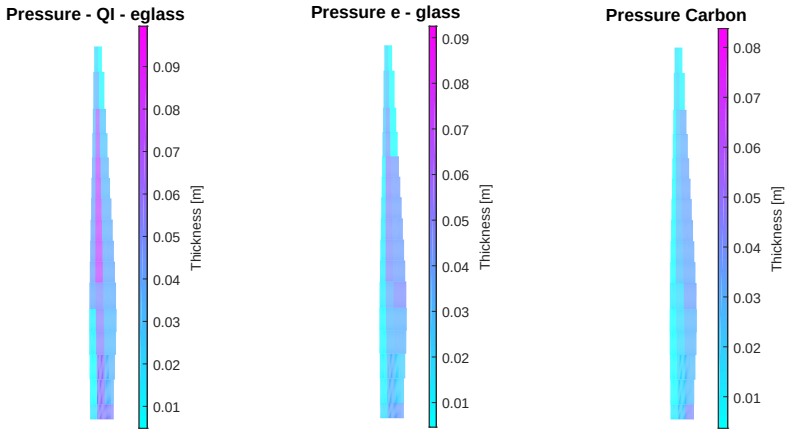

Figure 4.22: Skin thickness distribution presuure side for 10MW blade. Left: quasi-isotropic eglass, centre: tailored eglass, right: tailored with carbon fibre spar cap.

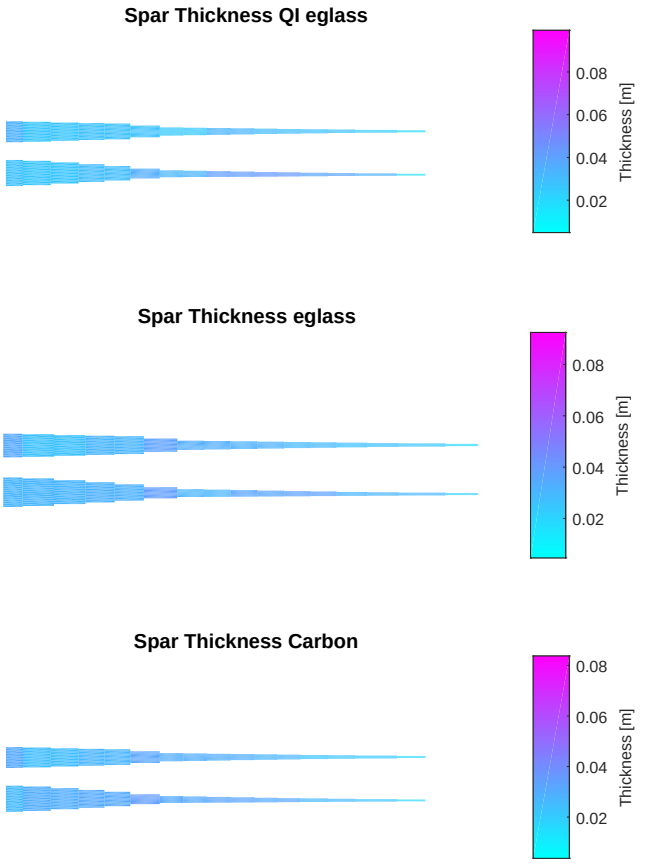

Figure 4.23: Spar thickness distribution for 10MW blade. Upper: quasi-isotropic eglass, centre: tailored eglass, right: tailored with carbon fibre spar cap.

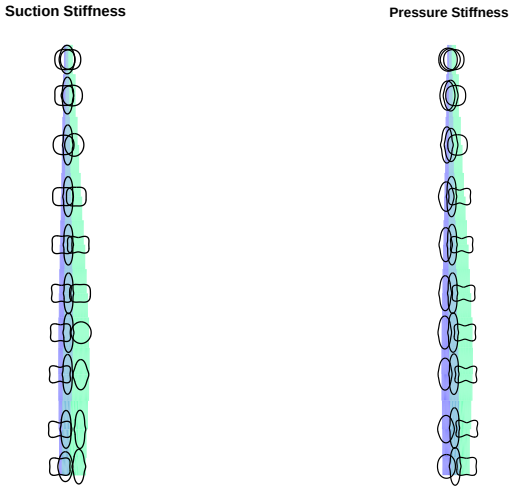

(a) Suction skin **(b)** Pressure skin

Figure 4.24: Tailored skin in-plane stiffness distribution for 10MW blade for eglass.

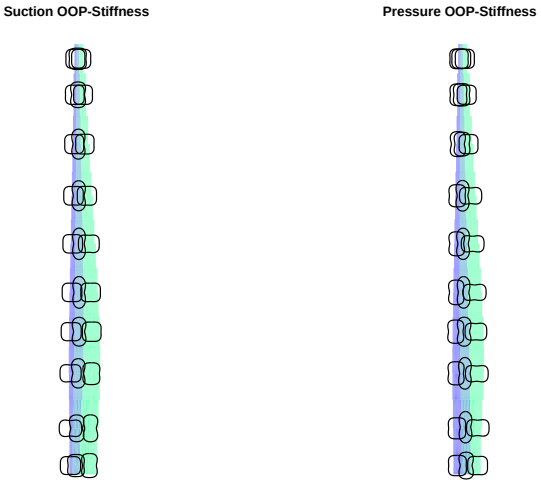

(a) Suction skin **(b)** Pressure skin

Figure 4.25: Tailored skin out-of-plane stiffness distribution for 10MW blade for eglass.

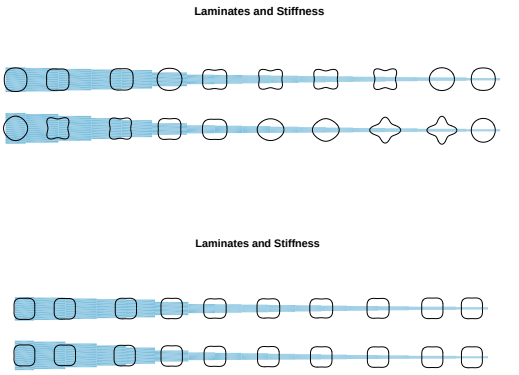

Figure 4.26: Tailored spar stiffness distribution for 10MW blade for eglass. Upper: in-plane, lower: out-of-plane.

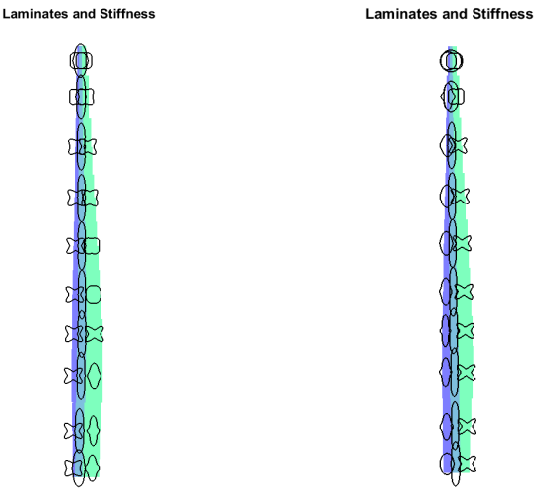

(a) Suction skin **(b)** Pressure skin

Figure 4.27: Tailored in-plane stiffness distribution of the suction and the pressure skin, for carbon spar caps, 10MW blade.

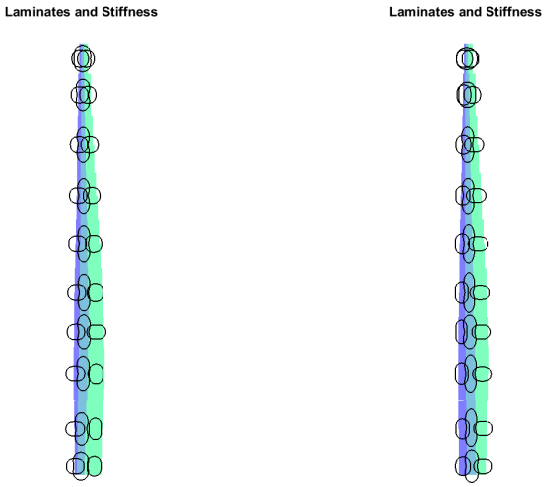

(a) Suction skin **(b)** Pressure skin

Figure 4.28: Tailored out-of-plane plane stiffness distribution of the suction and the pressure skin, for carbon spar caps, 10MW blade.

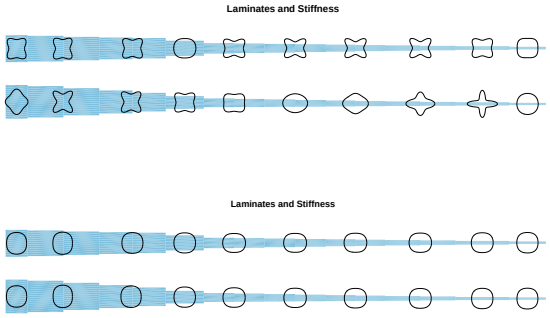

Figure 4.29: Tailored spar stiffness distribution for 10MW blade with carbon spar caps. Upper: in-plane stiffness, lower: out-of-plane stiffness.

art design methodology, which was also the case for the 5MW blade. Since the increased mass saving and the suction spar cap sandwich composite behaviour is observed for the 5MW blades as well as the 10MW blades, it is proposed to include sandwich composites within the suction side spar cap to save significant amounts of mass. Furthermore, Figure 4.30 shows the increase in twist angle in

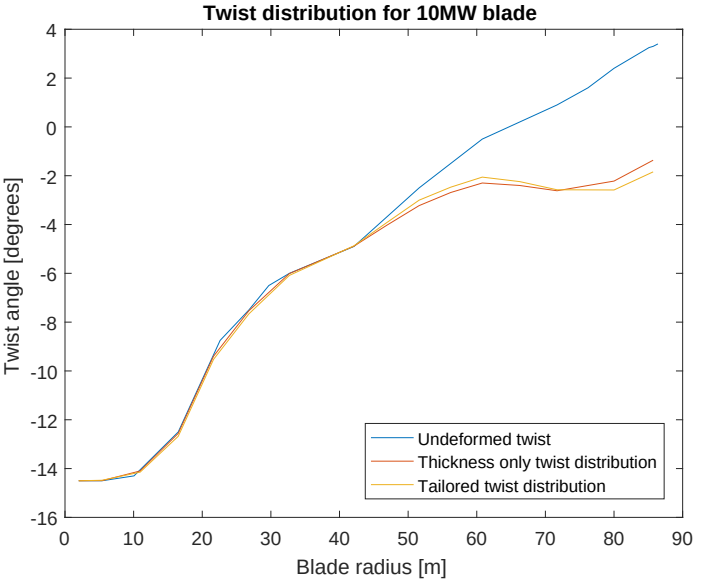

Figure 4.30: Twist distribution for the 10MW blade for the EWS load case.

the blade tip region, which indicates that the power constraint has become active. Furthermore, the differences in twist angle distribution for the quasi-isotropic design and for the tailored design observed do not look significant. However, some bend-twist coupling could have been introduced due to the anisotropic lay-up that lowers the torsional stiffness but still limits the twist angle.

4.1.3 20MW BLADES

From the quasi-isotropic analysis results, it is noted that around 55% of the blade span, the optimiser has difficulties to reduce the skin thickness of the blade because of high normal stresses. Since tailoring is not allowed in this case, the skin thickness has relatively high values which give a high blade mass optimisation result. This indicates the main problem of 20MW blades, as also appeared during the study carried out by [Castillo Capponi et al., 2011]. Due to the high blade span and restriction of blade material, tip deflection, and prevention of buckling of the suction skin, an efficient structural design is hard to achieve. Tailoring gives the possibility to reduce the skin thickness, and especially around this 55% blade span tailoring shows to be very efficient because the skin thickness is significantly reduced.

Considering the optimisation results for the full eglass epoxy, see Figures 4.31 and 4.32, the critical section is still present around 55% of the blade span and extends

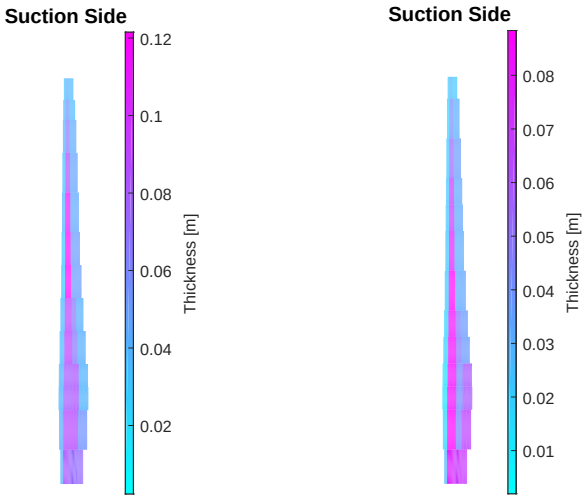

(a) Suction skin eglass spar cap **(b)** Suction skin carbon spar cap

Figure 4.31: Suction skin thickness for a 20MW blade

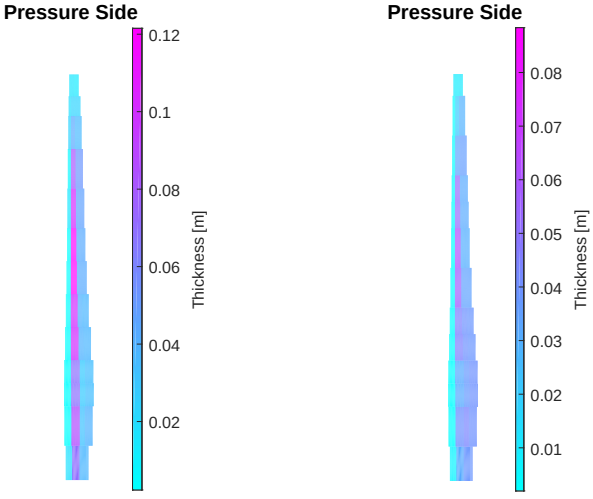

(a) Pressure skin eglass spar cap **(b)** Pressure skin carbon spar cap

Figure 4.32: Pressure skin thickness for a 20MW blade

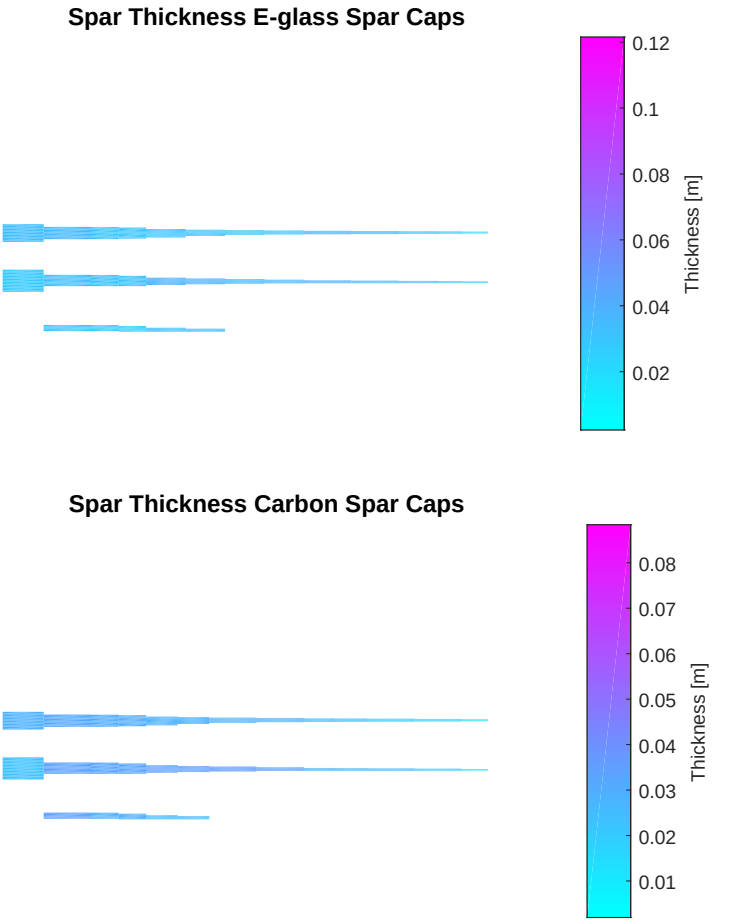

Figure 4.33: Tailored spar thickness distribution for 20MW blade. Upper: eglass spar caps, lower: carbon spar caps.

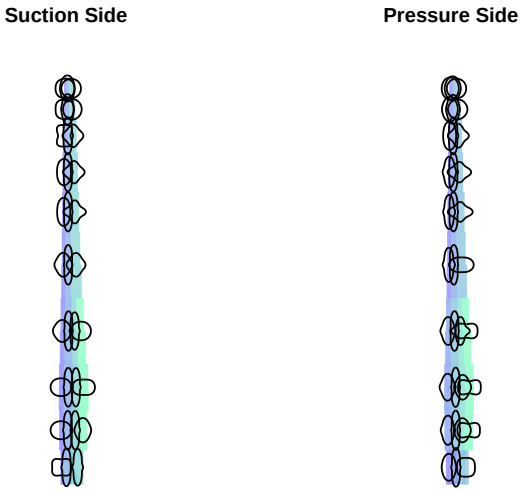

(a) Suction skin. **(b)** Pressure skin.

Figure 4.34: Tailored skin in-plane stiffness distribution for a 20MW eglass blade.

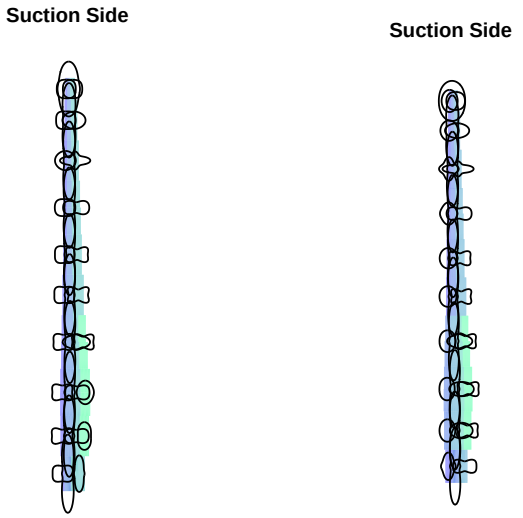

(a) Suction skin. **(b)** Pressure skin.

Figure 4.35: Tailored skin in-plane stiffness distribution for 20MW blade with carbon spar caps.

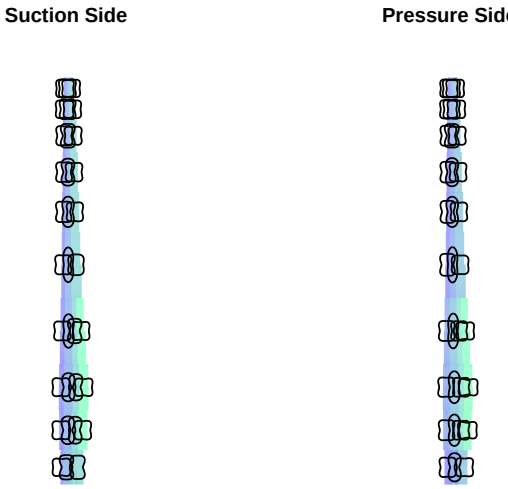

(a) Suction skin **(b)** Pressure skin

Figure 4.36: Tailored skin out-of-plane stiffness distribution for the eglass 20MW blade.

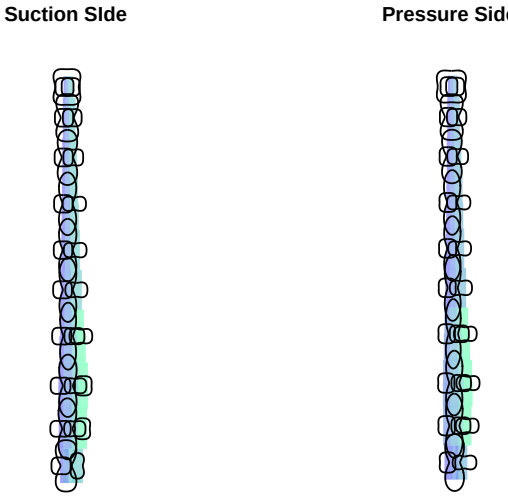

(a) Suction skin **(b)** Pressure skin

Figure 4.37: Tailored skin out-of-plane stiffness distribution for 20MW blade, with carbon spar caps.

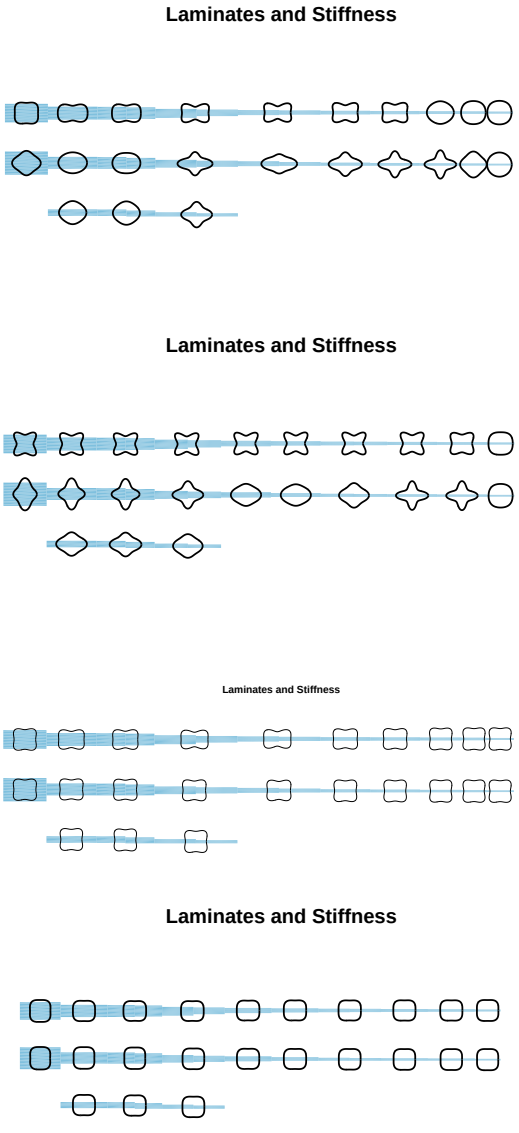

Figure 4.38: Tailored spar stiffness distribution for 20MW blade. Top to bottom: eglass in-plane, carbon in-plane, eglass out-of-plane, and carbon out-of-plane.

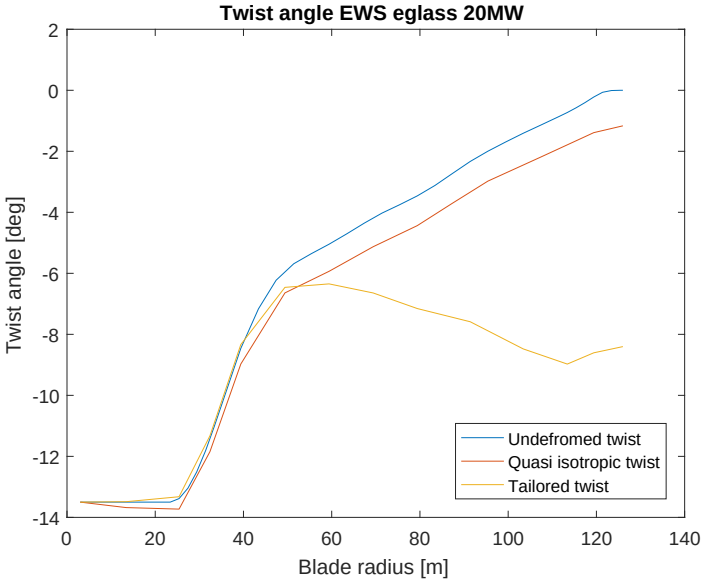

Figure 4.39: Twist distribution for the 20MW blade for the EWS load case.

in blade root direction for quite a few meters. Because of tailoring, it is possible to reduce the spar cap thickness of the suction skin to 12 centimetres. An interesting issue is that the local sandwich composite is mainly existing of face sheets and the core material is 60 times thinner than a face sheet. This is another sign that failure stresses are more critical around this blade section. For some stress relieve, one could replace the eglass fibres by carbon fibres and see what this gains in terms of mass saving. It is expected that the use of carbon fibre composites generates a different thickness distribution and stiffness distribution, which is discussed in the next section in which mixed material blades are considered.

4.1.4 MIXED MATERIAL SOLUTIONS

To gain more mass saving, it is suggested to build the blade spar caps of carbon fibre-epoxy. Carbon fibre reinforced composites possess better mechanical properties as, for instance, specific strength and Young's modulus, than eglass. For the 5MW, 10MW, and the 20MW blades, optimisations have been performed to observe the blade structural behaviour for different amounts of carbon-epoxy composites in the blade. Furthermore, only the mixed materials are applied within the spar caps, because they are the main load carrying path. To show the differences between a mixed material blade and a full eglass blade, the results from Figure 4.31, Figure 4.32, and Figure 4.33 are compared. The results show the

blade thicknesses of the 10MW and the 20MW blades respectively and contain a tailored blade that includes full carbon spar caps as well. It is observed that a significant reduction in skin thickness has been achieved. For the 10MW blade, a 10% thickness reduction has been accomplished with respect to the quasi-isotropic result. This indicates that tailoring with eglass still is interesting in comparison with a carbon fibre spar cap that generates a 20% thickness reduction compared to the quasi-isotropic eglass result. For the 20MW blade, eglass gives a maximum thickness of 12 cm, while applying a carbon spar cap tailoring drives towards a maximum thickness of 8 cm. This thickness reduction of 33% with respect to the tailored eglass result indicates a significant mass saving. Next, it is important to analyse the build-up of the sandwich composite in terms of face sheet and core thickness. This build-up is shown at the critical positions, expressed in percentage of the blade span. The locations considered are 35% for the 10MW blade and 55% for the 20MW blade. The results are summarised in Table 4.3.

Table 4.3: Sandwich composite build-up for the 10MW and 20MW blade at critical span

	t_f	t_c	t_f/t_c		t_f	t_c	t_f/t_c
10 MW	[m]	[m]	-	20 MW	[m]	[m]	-
eglass	0.0255	0.0354	0.72	eglass	0.0601	0.0014	42.9
Carbon	0.0151	0.0621	0.24	Carbon	0.0322	0.0159	2.02

The locations chosen are considered critical because of the face-core ratio t_f/t_c. If the ratio is low, the sandwich core is efficient to resist buckling and the facing sheets carry the load. When the face-core ratio is high, this means that the core has practically vanished and the sandwich composite has almost transformed into a pure fibre laminate. In mass saving terms, this is inefficient. It is favourable to create thickness using a low-density material to resist buckling and use the high-density facing sheet to carry the load. As such, the facing sheets should be as thin as possible. For the 10MW blade, both the eglass and the carbon spar cap, see Table 4.3 show a less critical face-core ratio than the eglass spar cap for the 20MW blade. This indicates that for the 10MW blade buckling is more critical, while the 20MW blade encounters both buckling and strain critical solutions. A carbon spar cap relieves the strain constraint significantly, which is indicated by the reduced face sheet thickness and the increased core thickness. It is suggested to use a partial or complete carbon spar cap for this 20MW blade.

From Figure 4.39 it follows that the full eglass blade, including spar caps, cannot be optimised to a feasible design if one considers the quasi-isotropic lay-up. The optimiser encounters problems with the quasi-isotropic case because of the material properties of eglass; since lay-up is not included in the quasi-isotropic optimisation the thickness cannot be decreased more to stay below the material allowable constraints, which are mainly the maximum allowable loads. As a consequence, the resulting local thickness reaches a minimum value to cope with the stresses but the blade mass is not feasible as well as the skin thicknesses at the critical locations. This results in high masses and stiffnesses in the outer part of

the blade, which is pointed out in Figure 4.39. The twist distribution in the outer part is only 1 degree lower and follows the undeformed twist distribution. This indicates a very high torsional stiffness in this region which gives the infeasible blade design. Furthermore, still for the quasi-isotropic case, using the carbon material for only 60% of the spar caps this gives a clear picture of the effect on the total blade. From root to approximately 60% of the blade span the power constraint becomes active, which can be seen from the change in elastic twist angle. For spar cap locations consisting of eglass, the thickness is a problem and causes high stiffnesses again, as can be concluded from the twist angle distribution. However, allowing tailoring, one observes a significant increase in twist angle in the outer blade section, resulting from decreasing thickness due to tailoring. Again, this twist angle distribution is a combination of reduced torsional stiffness and bend-twist coupling terms that limit the twist angles due to the decreased torsional stiffness.

From the stiffness plots, see Figures 4.35, 4.37, and 4.38 together with the twist distribution plots, it can be deduced that the carbon spar caps give significant improvements in the mass optimisation results. Because of the favourable stiffness and the stress allowables of the carbon epoxy laminate, the torsional stiffness of the outer blade section decreases due to the aerodynamic power constraint that has been triggered. In conclusion: the main problem occurs beyond 35% of the blade span for the 10MW and 20MW eglass blades. The mixed material solutions are mainly suggested for those cases. Especially for the 20MW blade, the critical stress location is around 55% of the blade span but the favourable mechanical properties of the carbon composite allow more tailoring, which delivers a thickness reduction in the critical area as well. A tailored blade, including full carbon spar caps, gives the highest mass and thickness reduction. However, from a cost point of view, a mixed spar cap with partial carbon and partial eglass will also give significant mass savings as will be elaborated in section 4.4.

4.2 Stiffened Skin Blade Layout

In the previous section, the sandwich skin blade optimisation results were shown. The results showed quite some potential for blade mass reduction by altering the spar cap layout. In this section, a different structural layout is proposed: the stiffened skin layout used in aircraft wings is applied to a wind turbine blade. These aircraft wing designs include ribs, spars and skin stiffeners instead of core material used in sandwich laminates. This means that the skin exists of pure laminates and the skin stiffeners as well. The dimensions of the spar buckling panels are determined by the rib spacing while the skin buckling panels are determined by the rib spacing and the stringer pitch together. Furthermore, different composite materials are used for the same structural layout; the blades are optimised for eglass-epoxy and carbon-epoxy unidirectional laminates, similar to the sandwich

skin investigation. The material stiffness properties used are shown in Table 4.4 and the material allowables are given in Table 4.5.

Table 4.4: Material mass and stiffness properties skin-stiffened blade

material	E_{11} [GPa]	E_{22} [GPa]	G_{12} [GPa]	ν -	density [kg/m^3]
eglass	40	8.33	4.20	0.27	1850
carbon	83	8.5	4.14	0.35	1452

Table 4.5: Material allowables skin-stiffened blade

material	X_t [MPa]	X_c [Mpa]	Y_t [MPa]	Y_c [MPa]	S [MPa]
eglass	392	300	40	62	41
carbon	2280	1725	57	228	76

For a convenient structural layout, the stringer pitch, rib spacing, and spar spacing are chosen. The structural layout of the blade to be optimised is summarised in Table 4.6 and is used for the stiffness optimisations:

Table 4.6: Structural lay-out of skin-stiffened blade

Blade span	0-20 [m]	20-40 [m]	40-61.63 [m]
Stringer pitch	0.3 [m]	0.15 [m]	0.075 [m]
Rib pitch	0.5 [m]	0.5 [m]	0.5 [m]
Spar pitch	0.89 [m]	0.89 [m]	0.89 [m]

For the blade optimisation, the exact same constraints are used for the sandwich blade: skin/spar buckling, strain, maximum tip deflection and minimum power loss. It was already concluded in section 4.1 that the extreme wind shear load case was critical: that means that the conventionally skin stiffened blades are only optimized for EWS. Finally, the stiffener properties must be defined and it is decided that the stiffeners are of the same material as the skin. The root section, midsection and tip section locations are defined in Table 4.6, and the longitudinal stiffener material properties are summarized in Table 4.7.

4.2.1 Full eglass blade results

The optimisations are performed for the 5MW, 10MW, and 20MW wind turbines for comparison with the sandwich blades. The 5MW and 10MW thickness and stiffness distributions are shown for the full eglass blades, to get an impression of the thickness and stiffness distribution differences between stiffened skin layout and sandwich layout. The main goal is to obtain optimum blade mass results for the stiffened skin blade designs and compare the thickness distributions and the stiffness distributions. The mass comparison will be performed in section 4.4.

Table 4.7: Longitudinal stiffener material properties

	Root section		Mid section		Tip section	
	EA [N]	mA [kg/m]	EA [N]	mA [kg/m]	EA [N]	mA [kg/m]
eglass	45,400,000	2.10	13,612,000	0.63	6,544,000	0.30
carbon	94,205,000	1.65	28,244,900	0.49	13,578,800	0.24

5MW BLADES The skin thickness for the changed structural design is shown in the Figures 4.40 below. Results show that the skin is indeed thinner than the sandwich designs; especially for the spar caps, where the stringers are included as well. Using longitudinal stiffeners instead of a sandwich skin gives an increase in optimized mass, but is still significantly lower than the baseline. Note that ribs are also included in the optimised mass since ribs are significantly present within the skin stiffened lay-out. The spar cap thickness in comparison with the leading edge and the trailing edge skin shows a more significant difference, which is different in the sandwich designs. The sandwich designs show a less pronounced spar cap thickness, especially at the suction side. The suction and pressure skins show a very similar behaviour in optimised lay-up considering the stiffness distribution in the spanwise and chordwise direction in comparison with the sandwich version, see Figures 4.41 and 4.42. The spar thickness distribution, however, shows some differences compared to the sandwich blades; the thickness is reduced, especially the rear spar.

A similar behaviour is observed for the stiffness distribution of the spars as shown in Figure 4.43: the spar cap lay-up tends to evolve towards the spanwise direction, due to the load carrying nature. The front spar evolves to a lay-up $\pm 30°$ and the rear spar shows converges to a lay-up of $0/90°$. The optimisation result shows a $9,6\%$ higher blade mass for the stiffened skin layout compared to the sandwich blade layout, but is still significantly lower, 22.6%, than the baseline mass of 17700 kg. An extensive mass comparison will be done in section 4.4, so the exact values are omitted here. The optimization behaviour is shown in Figure 4.44, which shows the break-off after 80 iterations. More important is, that this result of the stiffened skin design is heavier than the optimised sandwich blade. In terms of minimised mass, the sandwich blade is clearly in favour.

10MW BLADES The stiffness distribution of the 10MW blade is very similar to that of the 5MW case, as shown in Figures 4.46, 4.47, and 4.48.

For the 10MW blade, see Figures 4.45, a clear spar cap thickness is observed for the pressure skin as well as for the 5MW blade. The suction skin shows some increased thickness in the trailing edge root section because of buckling issues. The suction spar cap thickness blends more in the structure as observed for the pressure skin. An increase in overall thickness was expected but the optimised blade mass, including the rib mass of 3400 kg, approaches the sandwich result

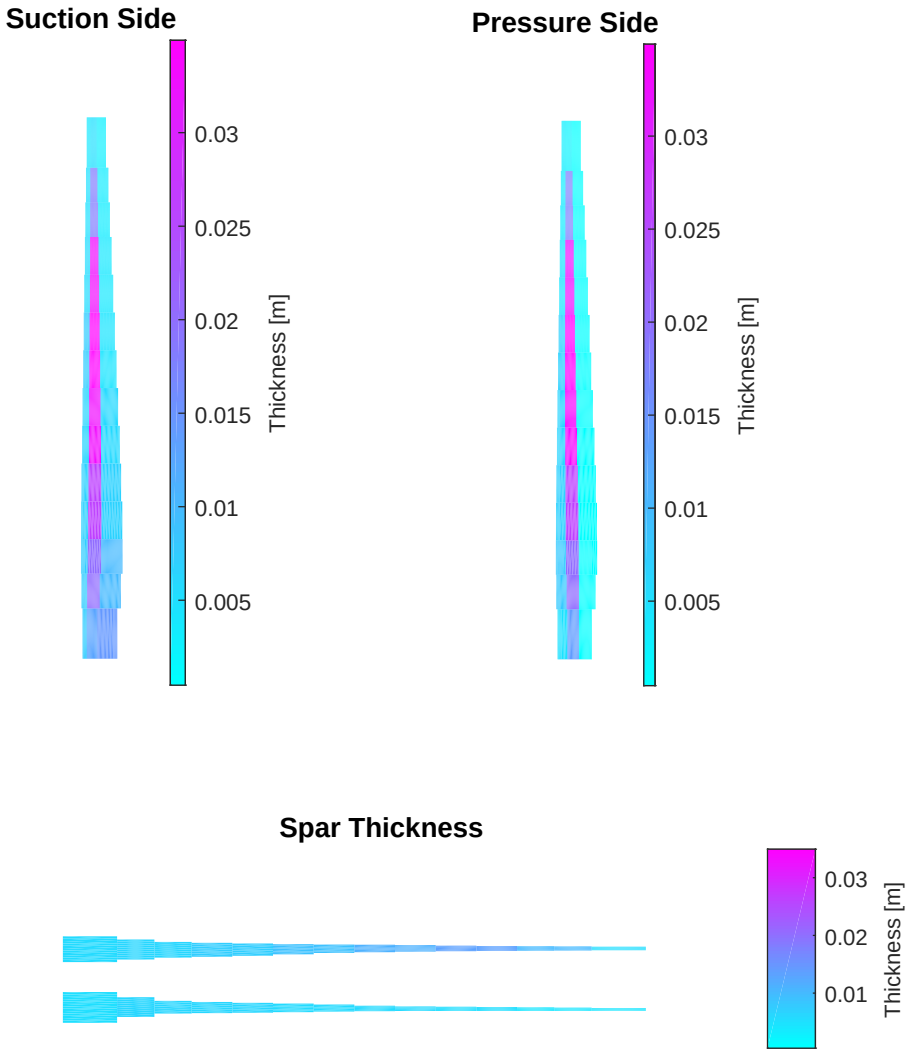

Figure 4.40: Skin thickness distribution eglass 5MW stiffened skin blade, EWS case. Left: suction side, right: pressure side, lower: spars.

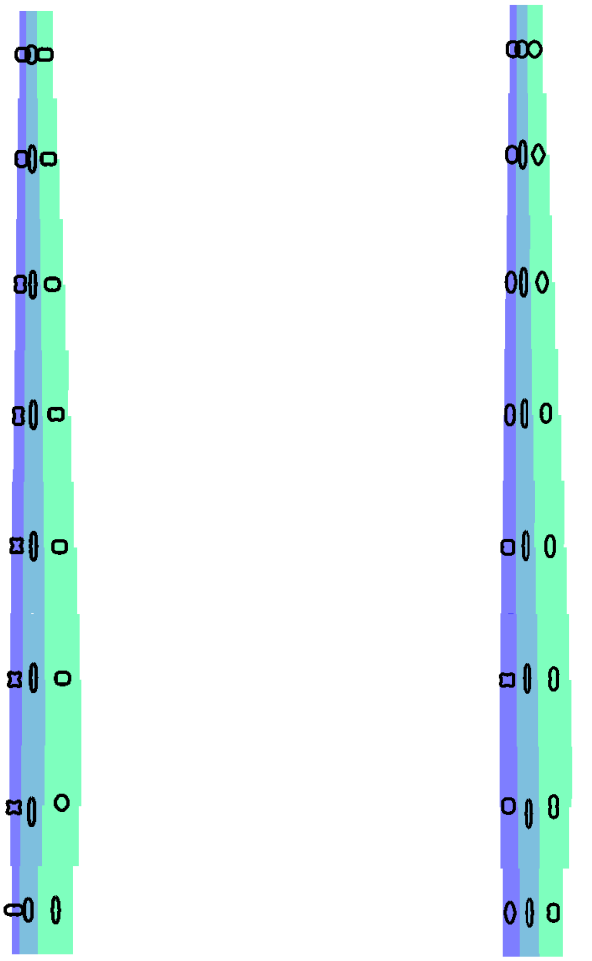

(a) Suction skin **(b)** Pressure skin

Figure 4.41: In-plane stiffness distribution eglass 5MW stiffened skin blade.

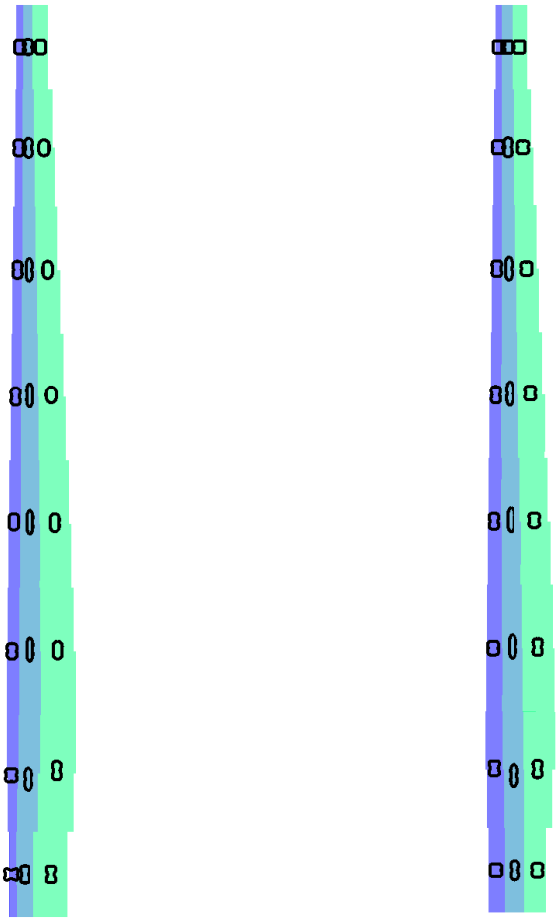

(a) Suction skin **(b)** Pressure skin

Figure 4.42: Out-of-plane stiffness distribution eglass 5MW stiffened skin blade.

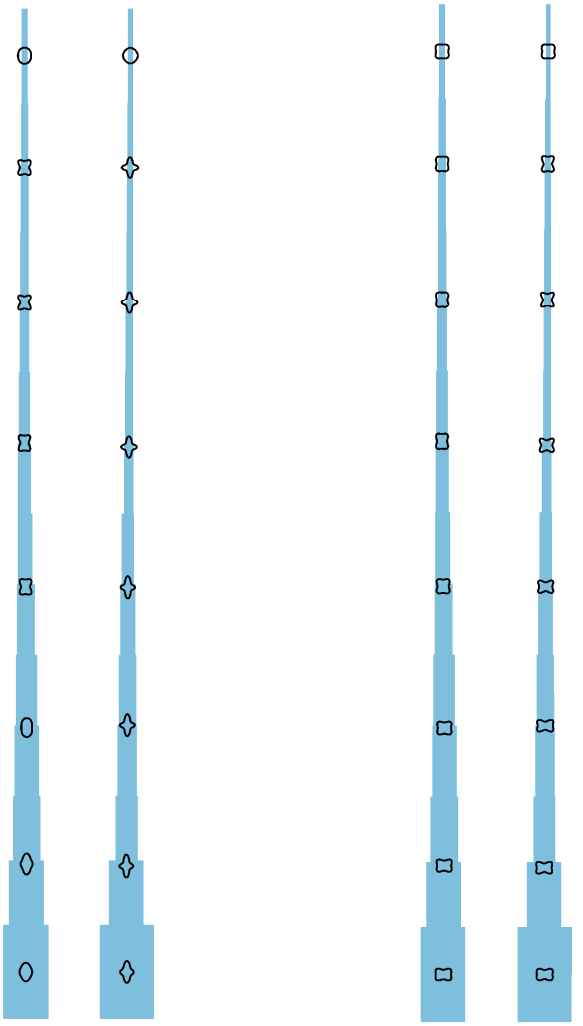

(a) In-plane stiffness distribution. Front spar (left) and rear spar (right)

(b) Out-of-plane stiffness distribution. Front spar (left) and rear spar (right).

Figure 4.43: Stiffness distribution of spars of eglass 5MW stiffened skin blade.

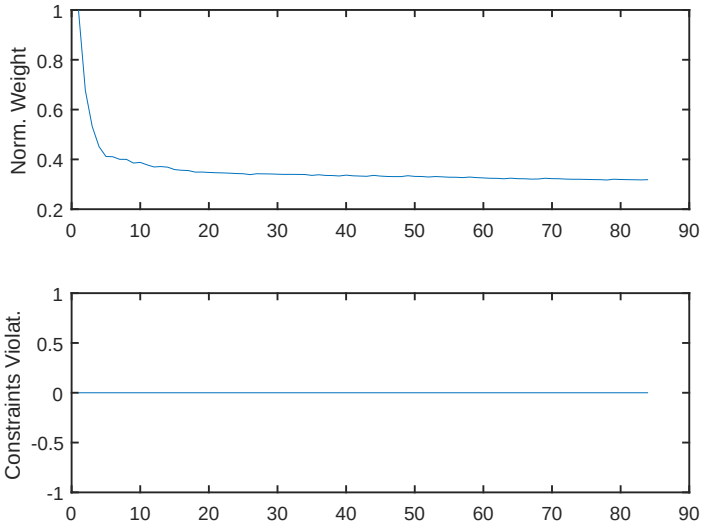

Figure 4.44: Objective and constraints against number of outer iterations for stiffened skin 5MW eglass blade

very closely. When comparing this result to the sandwich case, the stiffened skin design ended up 5.3% lighter.

4.2.2 Mixed material blade results

For comparison with the sandwich, the spar cap material is varied for the stiffened skin layout as well in the same manner: starting with 100% eglass and ending in 100% carbon with steps of 25%, for the 5MW, 10MW, and 20MW blades. To get an idea of the stiffness and thickness changes within the eglass and carbon laminates without presenting extensive stiffness and thickness plots, the lay-up is very similar to that of the presented results for the full eglass blades of the 5 and 10MW blades. The difference appears mainly in the spar caps which show higher stiffness because of the favourable mechanical properties of carbon-epoxy laminates but still show a unidirectional lay-up in the optimised design. For the case of 100% carbon spar caps, the thickness distribution in spanwise direction is similar to the eglass for both conventional stiffening or sandwich structure, except that the skin thickness maximum of the mixed material skin has been reduced by 14.3% with respect to the full eglass skin. The behaviour of the twist angle distribution for this stiffened skin case, including mixed material spar caps, is shown in Figure 4.50. Compared to the sandwich blade, the stiffened skin

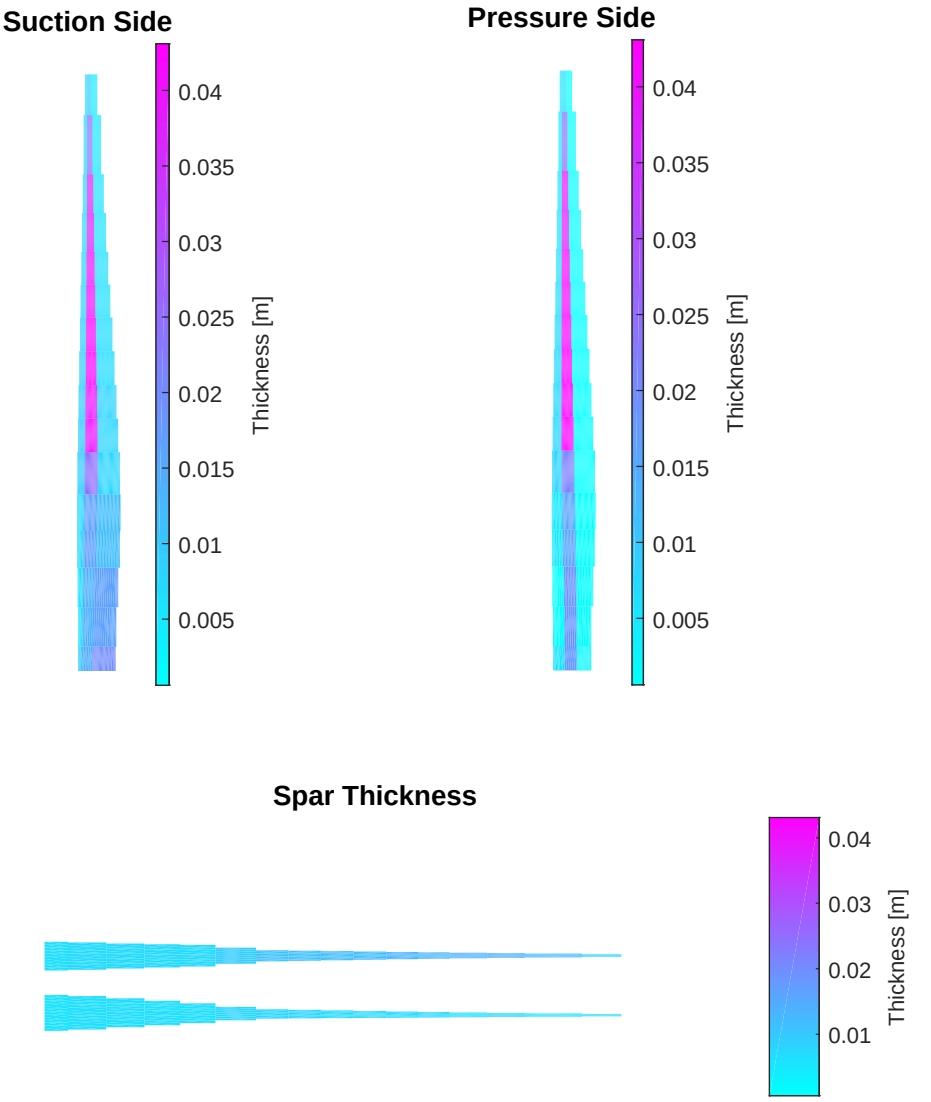

Figure 4.45: Skin thickness distribution eglass 10MW stiffened skin blade in the EWS case. Front and rear spar.

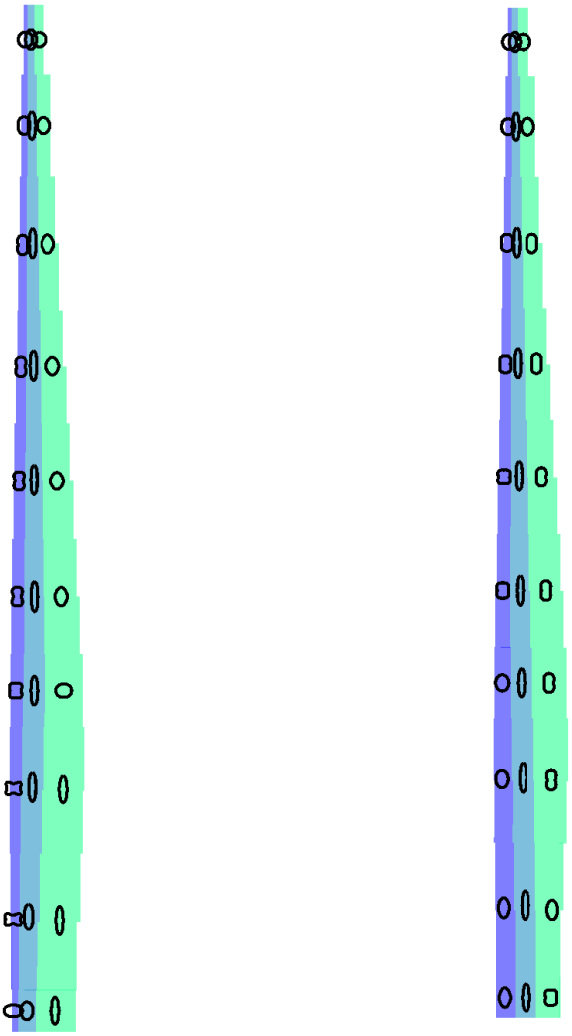

(a) Suction skin **(b)** Pressure skin

Figure 4.46: In-plane stiffness distribution eglass 10MW stiffened skin blade.

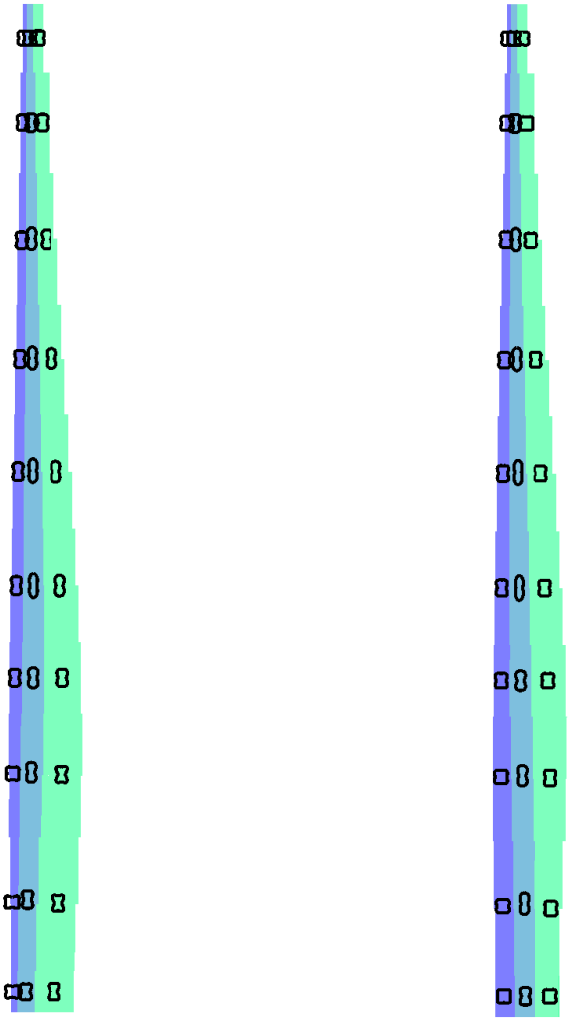

(a) Suction skin **(b)** Pressure skin

Figure 4.47: Out-of-plane stiffness distribution eglass 10MW stiffened skin blade.

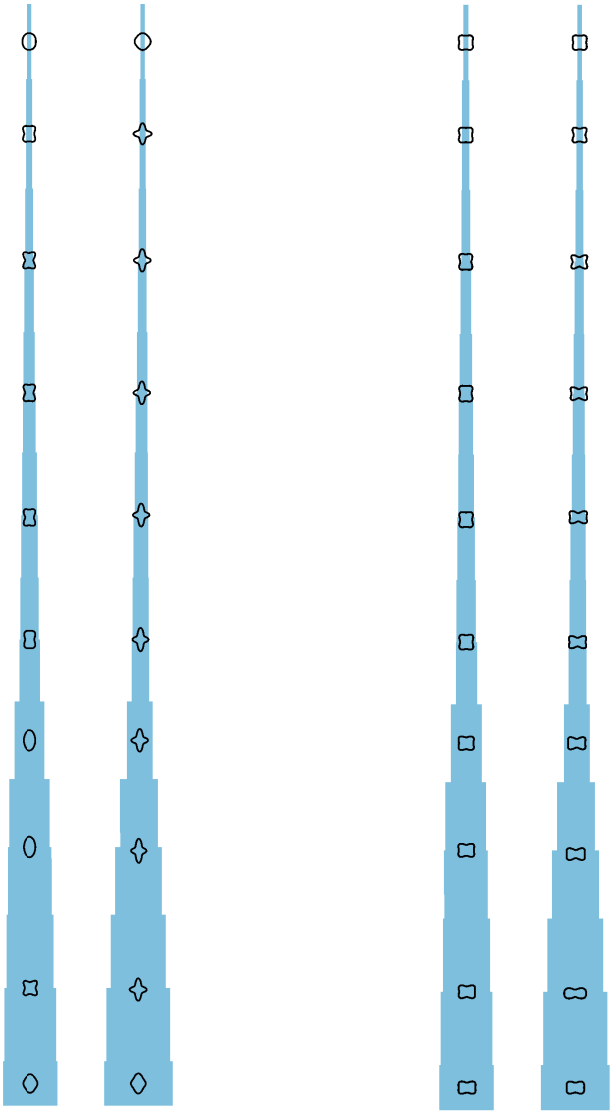

(a) In-plane stiffness distribution. Front spar (left) and rear spar (right)

(b) Out-of-plane stiffness distribution. Front spar (left) and rear spar (right).

Figure 4.48: Stiffness distribution of spars of eglass 10MW stiffened skin blade.

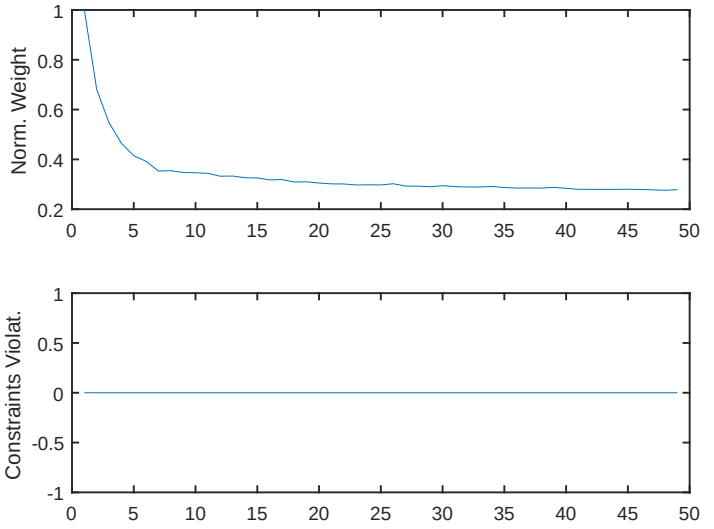

Figure 4.49: Objective and constraints against number of outer iterations stiffened skin 10MW blade eglass.

layout allows less torsional deformation which indicates higher stiffnesses in the tip regions. This effect is also noticed during stiffened skin blade optimisations with different percentages carbon within the spar caps: the minimum power constraint never became active.The reduced twist angles could be an effect of a different behaviour in the bend-twist interaction for the stiffened skin designs.

As observed form the optimisation results, the blade mass results drop with the increase of carbon fibres in the spar caps, which is not surprising. It is interesting to see that in some cases the conventional stiffened skin approach is in favour, while in most cases the full sandwich case is in favour. This will be discussed in detail in section 4.4.

4.3 IMPACT OF AEROELASTIC OPTIMISATION ON YEARLY POWER PRODUCTION

As already pointed out during the discussion about the power constraint in Chapter 3, the actual yearly power production is discussed in this section. The production part has not been implemented in the optimisation framework. The production losses are analysed using the optimisation results as a post-processing step. For the yearly power production, the power curves of the 5MW, 10MW,

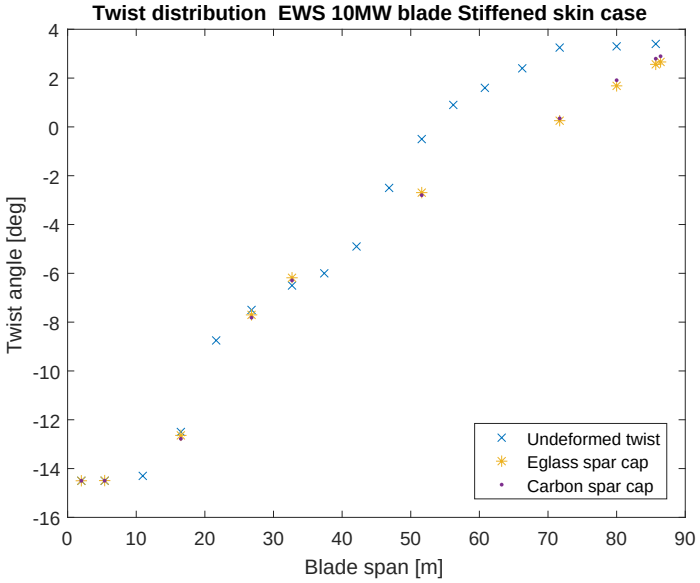

Figure 4.50: Twist distribution for the stiffened skin blade. The eglass and mixed material, in terms of a full carbon spar cap, are shown in the graph.

and the 20MW machines were constructed purely based on the optimised blade. From the power curves shown in the Figures 4.51, 4.52, and 4.53, one observes the decrease of aerodynamic power for the optimised blade. This power loss is caused because the collective blade pitch angle is not changed, due to the fact that control actions are not taken into account in this research.

The power curves serve as an input for the yearly power production. These power production results are an indication for the production loss due to structural blade optimisation. The production is determined following [van Bussel, 2010] and the accompanying graphs are shown in Figures 4.54, 4.55, and 4.56. This sheet uses the theory as explained in [Troen and Lundtang Petersen, 1989] and some aspects are mentioned next. The graphs are base on the Weibull distributed wind velocities for turbines that are in an area with a roughness length of $z_0 = 0.01$ m, which was used in chapter 3 as well. The hub height wind velocities for the different turbines are given in Table 4.8.

Table 4.8: Hub height conditions for yearly power production

	hub height	average wind velocity
5MW turbine	100 m	10.25 m/s
10MW turbine	120 m	10.45 m/s
20MW turbine	160 m	10.77 m/s

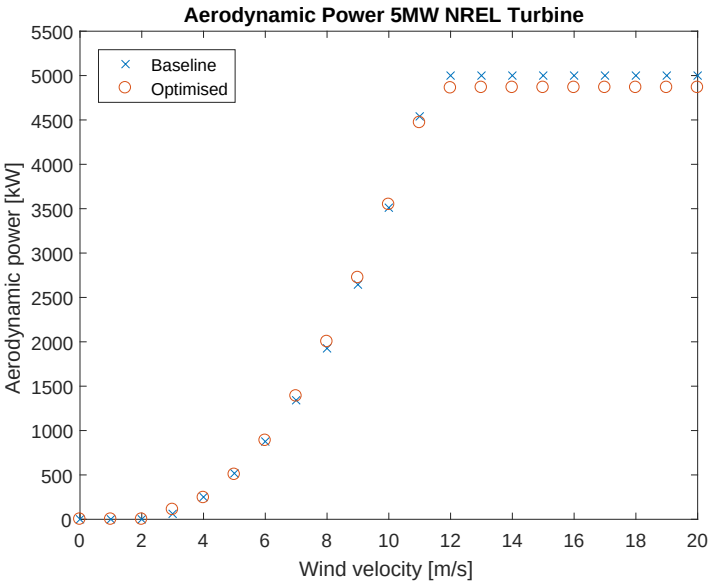

Figure 4.51: Power curve of 5MW turbine for the reference blade and for the optimised blade.

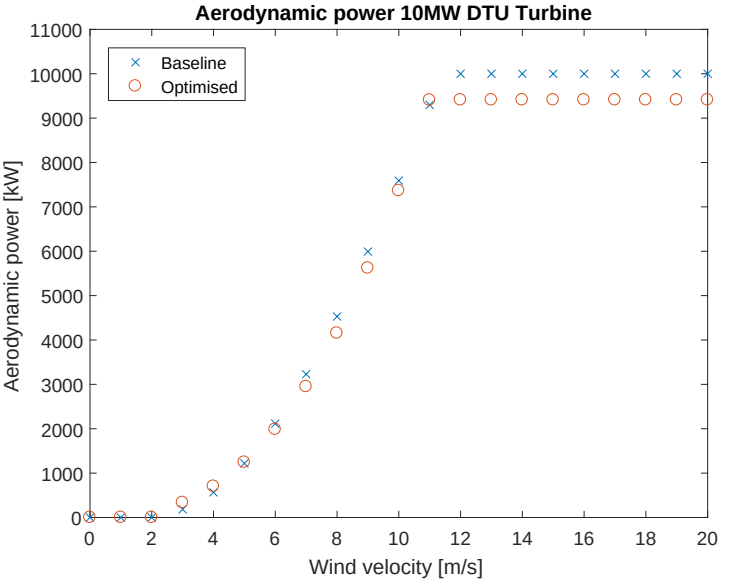

Figure 4.52: Power curve of 10MW turbine for the reference blade and for the optimised blade.

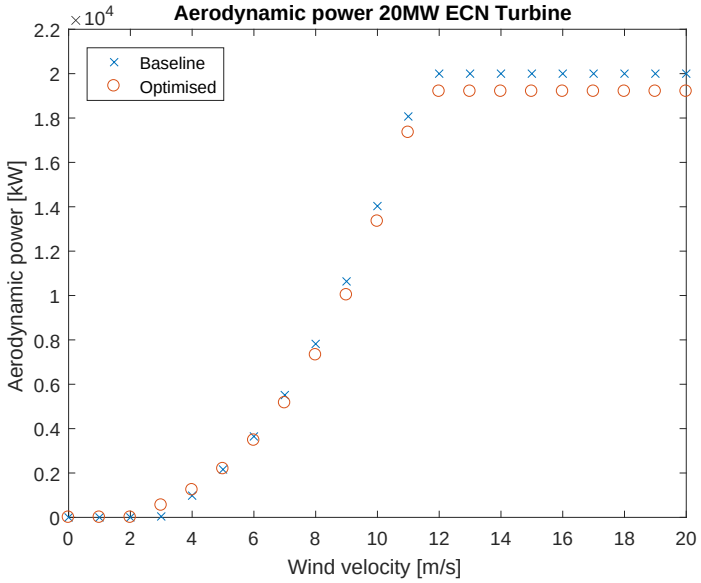

Figure 4.53: Power curve of 20MW turbine for the reference blade and for the optimised blade.

The power curves show that the most significant loss is at rated power and beyond. Considering the yearly power production, it might be that the production loss is not as significant as the power curves suggest. From the power production curves, the total production per year is calculated and presented in Table 4.9.

Table 4.9: Yearly power production for the 5MW, 10MW and 20MW.

	Production/m^2 $[\frac{kWh}{m^2 yr}]$ Reference blade	Production/m^2 $[(\frac{kWh}{m^2 yr}]$ Optimised blade	Loss [%]
5MW turbine	1764	1745	1.1
10MW turbine	1978	1884	4.6
20MW turbine	1767	1693	4.2

From Table 4.9 the relative production losses are around 1% for the 5MW turbine, however, for the 10MW and the 20MW turbines losses are around 4.5%. This is a significant loss but can possibly be compensated with an increased life cycle when using optimised blades where mass has been reduced significantly. Furthermore, lighter blades require less material and the handling during installation might become easier, which all results in a cheaper blade.

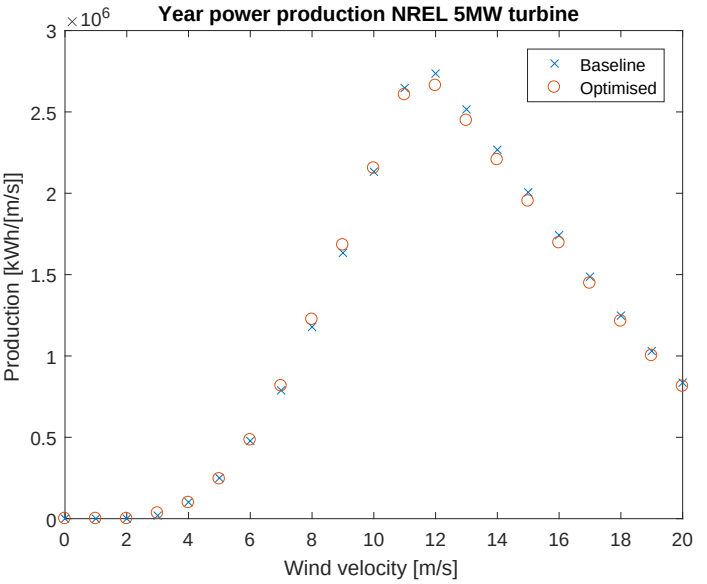

Figure 4.54: Power production of 5MW turbine for the reference blade and for the optimised blade.

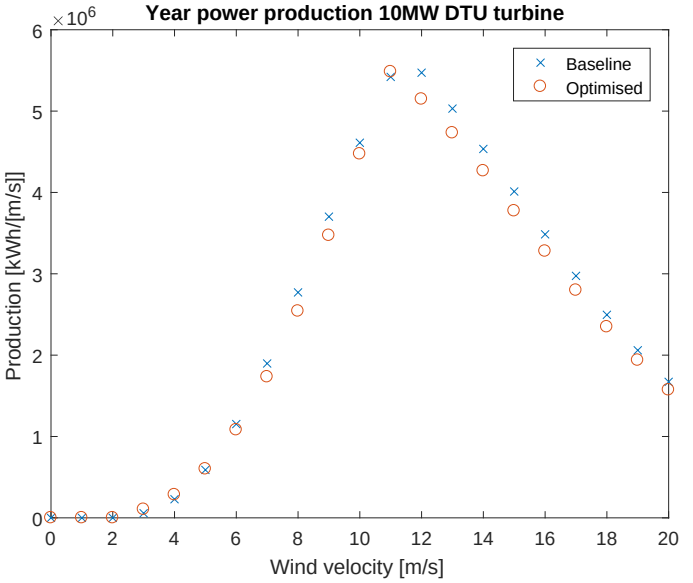

Figure 4.55: Power production of 10MW turbine for the reference blade and for the optimised blade.

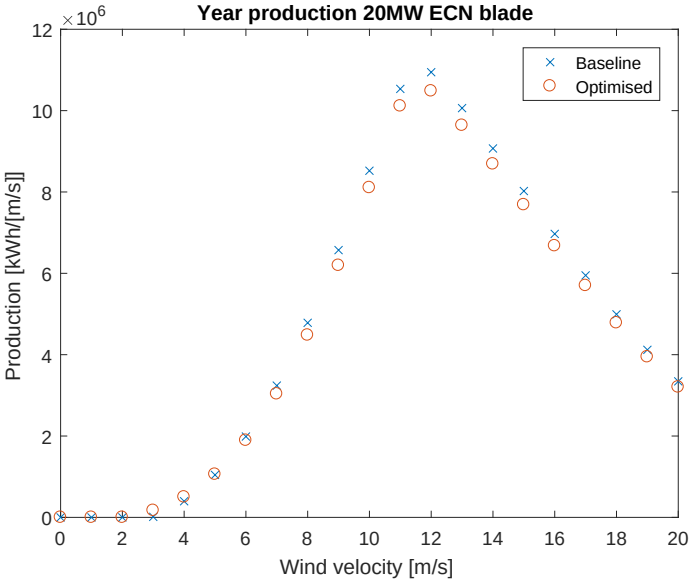

Figure 4.56: Power production of 20MW turbine for the reference blade and for the optimised blade.

4.4 Discussion

Optimised blades

The stiffened skin layout requires ribs to avoid local skin buckling. For the sandwich layout, ribs are not necessary because of the additional terms in the **D** matrix. This means some additional rib mass for the stiffened skin case, 858 kg for the 5MW blade, 3400 kg for the 10MW and 6000 kg for the 20MW blade. The results are included in the final optimisation results.

Table 4.10: Static aeroelastic optimised blade mass for different rotor blades

	5 MW	10MW	20 MW
Quasi isotropic sandwich blade	18,700 kg	43,000 kg	189,000 kg
Quasi isotropic stiffened skin blade	19,200 kg	55,500 kg	218,000 kg
Tailored sandwich blade	12,500 kg	35,800 kg	126,000 kg
Tailored stiffened skin blade	13,600kg	33,900 kg	118,000 kg

In Table 4.10, the converged results are shown. For the 10MW and 20MW case, the stiffened skin configuration shows lower optimised mass than the sandwich structural layout. The 5MW turbine blade optimisation shows a slight advantage for the sandwich structural layout. The results seem to show that there is some

break-even point between a 5 and a 10 MW turbine, considering the skin-stiffened structural layout. In fact, the results show a 5% mass reduction when using the skin stiffened lay-out for the 10MW blade, for the full eglass skin. For a 20MW turbine, there is even 6% mass reduction with respect to the sandwich layout, also for the eglass skin. With increasing blade dimensions, it is better to use a mixed material blade, for instance, the spar caps are of carbon-epoxy material and the remainder of the blade is made of eglass-epoxy material. Because of the favourable allowables and stiffness properties of carbon fibres, one can save several tons. The costs, however, will be higher. In the following tables is shown what mass savings could be achieved if only the eglass spar caps fibres are replaced by carbon fibres, starting at 0% to 100% using steps of 25%.

Table 4.11: Static aeroelastic optimised blade mass for different rotor blades, with 20% carbon spar caps

	5 MW	10MW	20 MW
Quasi isotropic sandwich blade	14,500 kg	40,100 kg	175,000kg
Quasi isotropic stiffened skin blade	18,200 kg	51,500 kg	201,000 kg
Tailored sandwich blade	9,900 kg	27,500 kg	92,000 kg
Tailored stiffened skin blade	12,000 kg	31,200 kg	104,000 kg

Table 4.12: Static aeroelastic optimised blade mass for different rotor blades, with 50% carbon spar caps

	5 MW	10MW	20 MW
Quasi isotropic sandwich blade	11,000 kg	33,000 kg	131,000 kg
Quasi isotropic stiffened skin blade	16,100 kg	40,900 kg	164,000 kg
Tailored sandwich blade	8,650 kg	22,000 kg	82,000 kg
Tailored stiffened skin blade	10,500 kg	27,500 kg	99,000 kg

Table 4.13: Static aeroelastic optimised blade mass for different rotor blades, with 100% carbon spar caps

	5 MW	10MW	20 MW
Quasi isotropic sandwich blade	10,000 kg	28,000 kg	100,000 kg
Quasi isotropic stiffened skin blade	13,000 kg	31,500 kg	154,000 kg
Tailored sandwich blade	6,150 kg	19,000 kg	61,000 kg
Tailored stiffened skin blade	9,290 kg	25,000 kg	68,000 kg

It is not completely valid to compare the sandwich designs to the stiffened skin designs. The core within the sandwich panels is a design variable that determines the out-of-plane terms in the **ABD** matrix and as such, the buckling behaviour of the panels. This core thickness can be seen as a smeared thickness of a certain stiffener distribution across the cross-section, apart from the rib pitch. In a way, the cross-section is partly optimised as well for the sandwich design. For the stiffened skin design, however, the stiffener distribution and stiffener dimensions across the cross-section are not in the optimisation. For the stiffened skin optimisation procedure, the thickness and the fibre angles of the laminate are

within the design variable vector. Realising that the stiffener distribution may not be the optimum for the stiffened skin layout, it may be concluded that for this configuration the optimisations could give lighter blade designs.
With this restriction in mind, the results are still very interesting. Considering the optimised blade mass of all 5MW configurations it is clear that aeroelastic tailoring can save a significant amount of mass with respect to the baseline of 17,700 kg, even when the proposed stiffness distributions of the skins and spars are not exactly applied in during manufacturing. One observes that for the full eglass blade, the sandwich design is still favourable for the 5MW blade, compared to the stiffened skin version. The differences even increase when parts of the spar caps are replaced by carbon epoxy composite: the sandwich design becomes even more favourable. This could be due to a non-optimum stiffener distribution over the cross-section for the stiffened skin design. The Figures 4.57, 4.58 and 4.59, show the relation between the optimised blade mass and the amount of carbon-epoxy fibre in the spar caps. The general behaviour is that the optimised blade mass shows convergence when the amount of carbon fibre in the spar caps approaches 100%. This is a clear indication that it is not efficient to replace the remaining structural eglass parts with carbon.

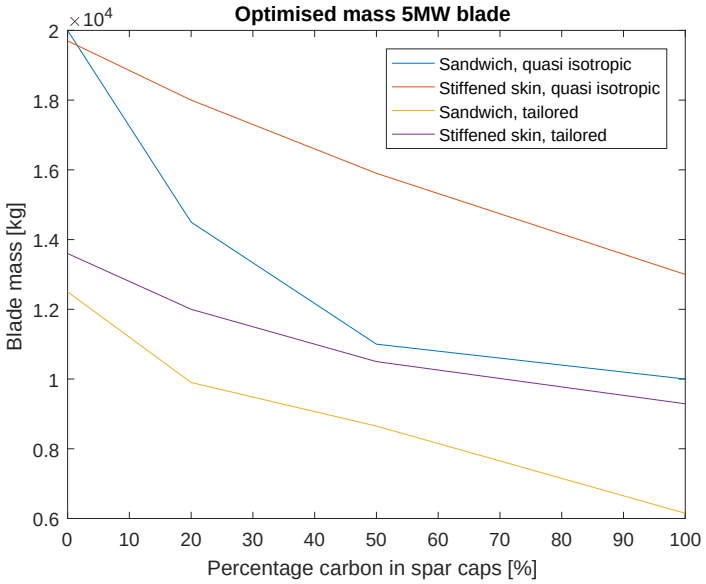

Figure 4.57: Optimised blade mass for different percentage of carbon laminates in spar caps 5MW

Altogether, for the full eglass skin, aeroelastic tailoring results in a mass saving with respect to the baseline, 29.3% for the sandwich design and in 23.2% for the stiffened skin design. The 10MW blade shows different behaviour. Again, the

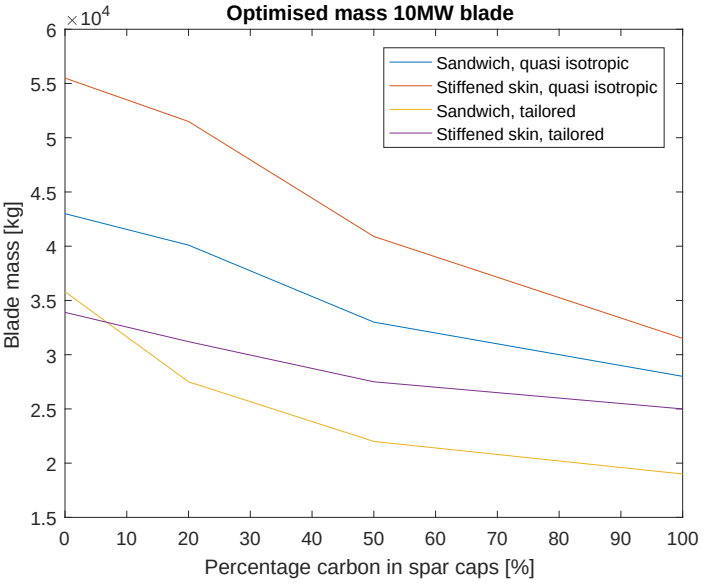

Figure 4.58: Optimised blade mass for different percentage of carbon laminates in spar caps 10MW

quasi-isotropic optimisations of the blade give a higher mass than the baseline from RISØ, [Bak et al., 2013], due to the sub-optimised design. Besides this observation, the stiffened skin design of the full eglass blade is in favour compared to the sandwich design, when aeroelastic tailoring is applied: a mass saving of 5.3% can be accomplished comparing both the optimised sandwich and stiffened skin layout. The saving of the stiffened skin blade with respect to the baseline, assuming 41 tons per blade, is 17.3% per blade. In comparison, the sandwich tailoring result converges towards as mass saving of 12.7% with respect to the baseline. The combination with carbon epoxy material is not favourable for the stiffened skin design; the sandwich lay-out outperforms the proposed stiffened skin approach. When the amount of carbon-epoxy composite increases, the stiffened skin structural layout arrives at a higher optimised mass compared to the sandwich layout.

Finally, the 20MW blade is an interesting case to explain in more detail. Firstly, the quasi-isotropic result for both the sandwich as the stiffened skin design gives too high results, with respect to the baseline of 160 tons. This is due to the fact that the baseline, [Peeringa et al., 2011], is, in fact, a sub-optimised design; a certain lay-up is already applied for the skins and the spars, as well as for the thicknesses. Since the stresses in the 20MW are very high, also due to the load case considered, the optimiser finds a heavier design compared to the baseline. The differences are quite significant: for the sandwich and for the stiffened skin

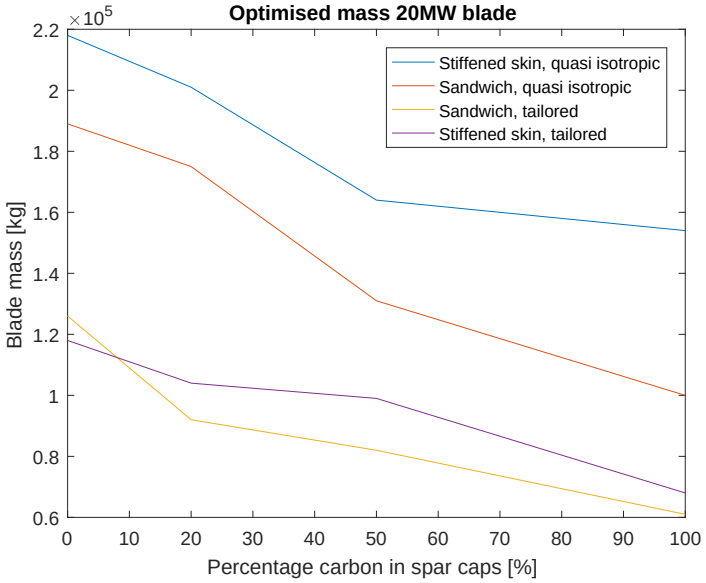

Figure 4.59: Optimised blade mass for different percentage of carbon laminates in spar caps 20MW

design 8.8% and 36.3% respectively. The deviation for the stiffened skin case could be due to the non-optimum stiffener distribution and dimensions across the cross-section. Again, it is interesting to observe that the tailored stiffened skin design converges to a lower mass than the sandwich design. With respect to the baseline, for a full eglass blade, the savings are 21.3% tons for the sandwich version and 26.3% for the stiffened skin design. There is even a difference of 6.3% between the sandwich and the stiffened skin structural layout, where the skin stiffened design is in favour. For the mixed material blade, carbon spar caps and eglass skin, spars and stiffeners, the sandwich outperforms the stiffened skin version. According to the results from Tables 4.11, 4.12 and, 4.13, the optimised mass keeps decreasing because of inclusion of carbon fibres within the spar caps, which is favourable for the total blade mass.

Considering the mass saving difference between the stiffened skin layout and the sandwich layout, it should be noted that the sandwich optimisations include sandwich composite in the spar caps, as pointed out in chapter 3. The optimisation shows the presence of core material in the suction side spar cap, while the pressure side spar cap core thickness was almost reduced to zero. Of course, the core material within the suction spar cap prevents local buckling together with a significant mass reduction: according to Table 4.1 the core material density is only 200 kg/m^3 compared to the glass epoxy material density of 1850 kg/m^3. This comparison is interesting because spar caps are generally built of fibre epoxy material

only; using the sandwich concept in the suction spar caps causes a significant mass saving. Since core material is required, the cost aspect remains an issue. On the other hand, a lighter blade generates less loading within the blades and other structural parts of the turbine, which is favourable for the life cycle of the complete turbine. In terms of mass saving one could choose for including sandwich material in the spar caps which requires some alterations to the manufacturing process of the blade or one could decide to rigorously change the structural design in a stiffened skin design which requires a significant change in the manufacturing process, resulting in increased costs.

UP-SCALING

Upscaling laws proposed by [Chaviaropoulos, 2007] have been used for preliminary, sub-optimised designs of wind turbine blades for 10MW or 20MW wind turbines. Besides the fact that this upscaling is performed assuming a predefined lay-up and thickness distribution, the scaling laws are subjected to change as well: due to technology improvements or change in insights on blade design, such laws are only valid for a certain design era. As can be observed from the optimisations in the previous sections, a significant amount of mass can be saved by applying aeroelastic tailoring. Considering the sandwich designs, it is obvious that allowing tailoring for the sandwich skin and spar give significant mass savings for all designs. Even the pure eglass design gives a saving varying between 20% and 30% with respect to the baselines. The mixed material designs save more mass by means of applying a carbon epoxy laminate for part of the spar caps or the full spar caps. In this research, carbon spar caps are chosen only because of the load carrying nature of the box beam. The remaining part of the blade is of eglass-epoxy, which is perfectly able to resist shear and the buckling loads, in the leading or trailing edge parts of the skins. For the same reason, the spar webs are of eglass epoxy material as well, the shear-resisting nature of these structural parts is sufficient.

Some typical scaling rules for the blade mass are, according to [Fingersh et al., 2006] and [Chaviaropoulos, 2007]:

$$m = 0.1452R^{2.9158} \tag{4.1}$$

for *baseline technology* [sic] [Fingersh et al., 2006], but for *advanced application of technology* [sic] [Fingersh et al., 2006] the law changes in:

$$m = 0.4948R^{2.53}. \tag{4.2}$$

From Table 4.10, it appears that the quasi-isotropic mass optimisation values are not in line with the scaling laws. According to [Peeringa et al., 2011] the blade

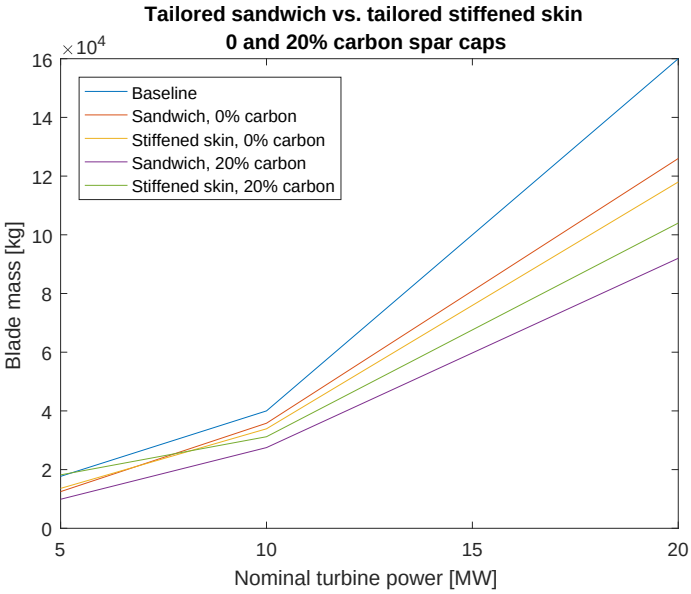

Figure 4.60: Optimised blade mass as a function of wind turbine power

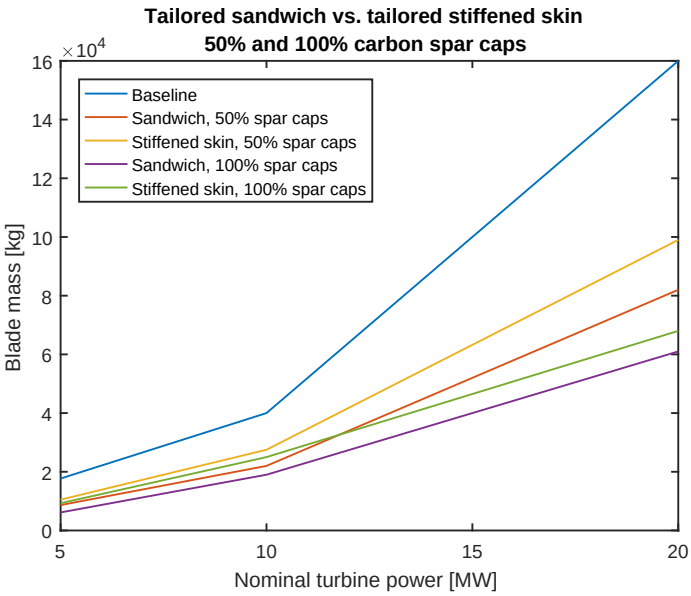

Figure 4.61: Optimised blade mass as a function of wind turbine power

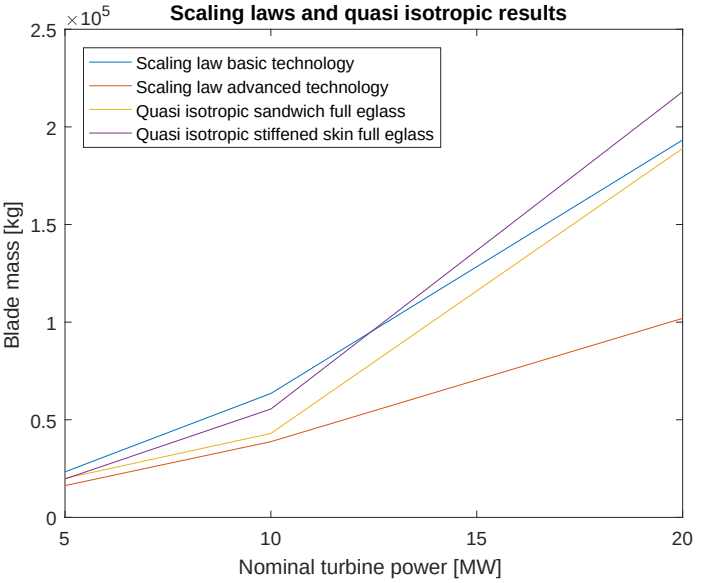

Figure 4.62: Up-scaling laws versus the quasi isotropic optimisation results

design mass arrives at 160 tons while the scaling law predicted 140 tons. The 10MW blade, however, [Bak et al., 2013], comes up with 40 tons per blade, while the performed optimisations within this research arrive at a quasi-steady result of 43 tons, which is a promising result. Those differences could be caused by the effects of a scaling law which is not applicable in every case. In the Figures 4.60 and 4.61, the blade mass as a function of the nominal wind turbine power is sketched, showing the baseline mass result and the optimisation mass results.

The quasi isotropic designs and the baseline designs are comparable up to a nominal power of 10MW, the 20MW designs are not. This indicates that the scaling laws used might not be up to date. From Figure 4.60, it is observed that the eglass quasi isotropic optimised mass results, as a function of nominal power, first follow the advanced technology scaling law, and for the 20MW blades, jump to the basic technology scaling law. This is curious, since the structural design concept was not changed. A nonlinear scaling law is more suitable as proposed by [Castillo Capponi et al., 2011], for up-scaling of a 5MW turbine to large turbines with nominal power of 20MW. From [Castillo Capponi et al., 2011], the result for a 20MW blade is about 200 tons, and is close to the quasi isotropic design 189 tons found during the presented research. The scaling law of [Chaviaropoulos, 2007] is sketched in Figure 4.62, together with the quasi isotropic optimisation of the eglass sandwich blade, and it is clear that this law is not suitable for up-scaling up to 20MW turbines. Lastly, it is observed that all optimised blade masses are

lower than the masses resulting from the basic technology law, and that inclusion of carbon in the spar caps drives the optimised masses towards the advanced technology results.

4.5 Concluding remarks

The quasi-isotropic optimisation results of the 5MW eglass blade approximate the baseline blade mass very closely. This indicates a correct critical load case selection and a further proof of correct aerodynamic and structural blade modelling. A significant result from the quasi-isotropic optimisations is that the 20MW rotor blade does not meet the blade mass of the baseline design. This is caused by the material properties of the eglass composite material: the material properties are not sufficient for a feasible 20MW design. It was also found that with a quasi-isotropic optimisation, where the spar cap material was replaced by carbon epoxy composite material, this material property problem of eglass became less significant because of the more favourable mechanical properties of carbon. For the 10MW blade, no problems were detected during the optimisations. The quasi-isotropic results of the full eglass blade were comparable to the mass of the 10MW baseline from RISØ.

The tailored 5MW NREL rotor blade mass for the critical load case EWS converges to a value of 12,500 kg. The NWP load case had been considered as well but resulted in a significantly lower mass, 7900 kg. For further optimisations, the EWS load case was used as a critical load case. The optimised blade mass results for the 10MW blade is about 35,000 kg and 118,000 kg for the 20MW blade for both full eglass blades. For the full carbon sandwich composite spar cap versions of the 10MW and 20MW blades, the optimised masses become 19,000 kg and 61,000 kg, respectively. One observes a significant drop in blade mass for the 20MW blade, compared to the quasi-isotropic case.

For both the NWP and the EWS load cases, the stiffness distribution is similar. The spar webs show a shear-resisting lay-up, while the suction and pressure side spar caps are optimised towards a unidirectional lay-up. The skin parts that form the remainder of the torsion box exhibit different behaviour. Especially the suction skin is critical for the buckling constraints. The lower skin leading edge shows some unidirectional behaviour, which indicates that the leading edge and spars are the load carrying part while the remaining leading edge and the trailing edge loading are significantly different, mainly shear resisting. The twist distributions show that the twist deformation becomes effective at the outer blade section due to higher aerodynamic loading and lower torsional stiffness. For the sandwich blades, the aerodynamic power constraint is active in all tailoring sessions which means that the twist angles for the quasi-isotropic case and the full tailored case are approximately equal. The tip deflection constraint assures that the out-of-plane bending stiffness is kept within range.

A further analysis of the results shows that it is favourable to apply sandwich spar caps in the suction spar caps of the sandwich blade and that this structural layout is a better choice than constructing the skin with a longitudinal stiffeners attached to a full fibre skin where the buckling panels are limited by the spars, the ribs and, the longerons. Still, this structural layout of a skin-stiffened blade is in favour of the state-of-the-art sandwich blades, because of applying the variable stiffness concept.
As a last important finding, the optimised blade mass as a function of the aerodynamic wind turbine power does not follow the scaling laws that were used to design the reference 10MW and 20MW blades.

5

Conclusions and recommendations

Within this research, a stiffness optimisation was performed which has as objective the minimisation of blade mass. For this purpose, an equal fidelity static aeroelastic analysis code was developed and integrated within an optimisation framework. Using this optimisation framework, optimum structural blade results were generated. This chapter summarizes the conclusions drawn throughout the thesis that answer to the main research goal as formulated in chapter 1:

Find an optimum structural and material layout for large wind turbine blades using an equal fidelity aeroelastic analysis code suitable for optimisation purposes.

5.1 Conclusions

Equal fidelity aeroelastic modelling

The aeroelastic model developed in this research was developed for efficient optimisation purposes. The computational effort within the model was, amongst others, improved by using a cross-sectional modeller that converts a full 3D blade model to a 1D Timoshenko beam element embedded in a corotational framework while preserving the orthotropic behaviour of the composite skin and spar parts. Before

this transformation, a check from a comparison of **ABD** matrices of pure laminates and sandwich laminates showed the expected behaviour, i.e. the elements in the **A** and **D** matrices for the sandwich laminates have increased with approximately a factor 2 with respect to the pure fibre laminates. This indicates that the sandwich laminates are properly modelled. Furthermore, the aerodynamic model chosen is a non-planar vortex panel model which may cause computational effort problems because of the cylindrical wake. To describe the cylindrical wake properly, the number of wake panels is significantly higher compared to a flat fixed wing wake. However, supported by efficient coding techniques, the helical wake did not cause time problems for the chordwise integrated aerodynamic force and moment calculations that follow from multiple vortex panels. The aerodynamic loads were obtained from a multi-panel vortex method on the blade and in the wake and transformed to an aerodynamic load distribution across the blade span in the local quarter chord position. According to the definition of model fidelity in chapter 1, this model can be referred to as a medium fidelity aerodynamic model. Eventually, both the structural loads and the aerodynamic loads were defined over a single line of equal fidelity and served as an input to the aeroelastic analysis. For the aerodynamic loads and structural loads, the sensitivities with respect to the blade structural degrees of freedom were obtained analytically. This accomplished the close coupling within the aeroelastic analysis. The structural solution found is geometrically nonlinear because beam elements are embedded in a co-rotational framework.

For the validation of the aeroelastic code, the normal force distribution and the tangential force distribution was used to check the aerodynamic part; the aeroelastic behaviour was checked by considering the tip displacement and the aerodynamic power. From the validation results presented in chapter 2 it followed that the normal force distribution is almost equal to the results from the validated FAST code, which means that, up to rated, the aerodynamics was implemented in a sufficient way. For the aeroelastic results, the tip displacement as a function of the velocity follows the behaviour of the NREL reference blade very close up to a wind velocity of 12 m/s the difference beyond 12 m/s is due to a different, not so accurate, pitch control algorithm. This did not generate problems because the optimisations were performed 3% below rated. Yet, the blade power curve was shown, and it was observed that some variation above rated due to the inaccurate modelling of the pitch controller is present. However, the aeroelastic code proved to behave such that it can be used for optimisation purposes up to rated. The optimisation results were to be used for blade design purposes.

STRUCTURAL OPTIMISATION PROCEDURE

The optimisations were performed for a sandwich skin but also for a stiffened skin configuration where the blade consists of ribs and longitudinal stiffeners on the suction and pressure skin. Next, the structural optimisations required the

following design variables. For the sandwich structural layout, the lamination parameters were coupled to a sandwich laminate by defining only the lamination parameters for the faces that actually contain the fibres. It was also assumed that both faces have the same lay-up and thickness such that the lamination parameters of only one face sheet have to be defined. Furthermore, the thickness of the sandwich core was added to the design variable vector to fully define the sandwich laminate.
The optimisation was carried out using the Extreme Wind Shear load case to arrive at results that produce useable results for an actual blade structural design. To verify whether the extreme wind shear is a heavier load case than the normal wind profile, a comparison between those load case was done. Thickness plots and stiffness plots showed that extreme wind shear is indeed a more severe load case, especially the maximum thickness is increased by 27% while the thickness distribution shows similar behaviour compared to the normal wind profile case.
As a reference for the optimiser and also an extra check, quasi-isotropic optimisation cases were carried out. For instance, the quasi-isotropic results generated a 3% higher flap stiffness distribution than the actually chosen baseline. Because the baselines already are sub-optimised using the fibre orientation, the stiffness distributions and the blade masses will differ. Still, a 3% higher out-of-plane bending stiffness distribution and an 11% higher in-plane bending distribution are promising results. For the thickness distribution it was found that the 5MW blade (8% higher than baseline mass) and 10MW blade (7.5% higher than baseline mass) were comparable to the actual baseline designs masses but the 20MW blade (18 % higher than baseline mass) was not able to converge to a feasible thickness distribution due to high stresses around 55% of the blade span. To solve this issue for the 20MW blade, a mixed material solution was introduced. Within this solution, the eglass-epoxy laminates of the spar caps were replaced by carbon-epoxy laminates such that the laminate can handle the stresses in a 20MW blade.

Tailored blade results

The tailored blade results, for the sandwich as well as the stiffened skin configuration, showed a significant mass reduction compared to the baseline designs using the variable stiffness concept. On the other hand, it was observed that the stiffened skin configuration did not show significant advantages compared to the sandwich skin configuration; this became even more distinct when the mixed-material, where the eglass material of some structural parts is replaced by carbon material, was introduced within the spar caps. This behaviour was due to the fact that the stiffener pitch has not been optimised; the stiffener pitch was kept constant during the optimisation procedure.
Both configurations showed significant mass savings compared to the baseline designs. And the savings increase with increasing aerodynamic power. For the 10MW and 20MW blades, up-scaling based on the 5MW machines is applied. It

appeared that, especially in the 20MW case, the blade design became infeasible. Furthermore, a relation between blade mass and amount of carbon fibre in the design showed that using carbon for other parts than spar caps will not give a further significant reduction of the mass.
The graphs of optimised mass against aerodynamic power are kind of upscaling graphs as well. From those graphs it can be concluded that the baseline designs show a steeper gradient than the optimised designs; the amount of carbon in the designs reduces the gradient even further. It was observed that switching materials from eglass to carbon for a approximately 30% of the baseline structure, in this case, the full spar caps, saved about 50% blade mass with respect to the baseline.

The stiffened skin designs showed higher masses than the sandwich designs. The differences between the two configurations were most prominent for the 5MW turbine. For the 10MW and 20MW blades, the differences were less because the skin stiffening was not varied for the stiffened skin configuration. Since the sandwich core thickness was part of the optimisation procedure, the comparison is not completely fair. The sandwich core thickness can be seen as some smeared thickness of stiffeners and influences skin buckling, which is controlled with stiffener pitch and dimension in the stiffened skin designs. Since the stiffened skin layout was not optimised for stiffener pitch, it can be assumed that the conventional designs can become lighter. An additional explanation for the mass difference between the sandwich design and the conventional design originates in assuming sandwich composite in the spar caps. Especially in the suction spar cap, the optimiser assumed significant amounts of core material to prevent the skin from buckling locally, resulting in mass savings of 26% for 5MW blades and 14% for 10MW blades with respect to pure fibre laminate spar caps. The state-of-the-art blades do not use sandwich laminates in the spar caps. Allowing sandwich composites in the spar caps is a significant cause of the substantial mass savings. The stiffened skin design and the sandwich design, including suction spar cap and eglass only, gave significant mass savings with respect to the baseline designs, varying between 23% and 29% for the 5MW blade, where the sandwich was favourable. For the 10MW blade, a saving between 12% and 17% was accomplished, where the stiffened skin layout is favourable, and, mass savings between 21% and 26% were found for the 20MW blade, where the stiffened skin layout was in favour as well. For the mixed material cases, the sandwich layout became favourable in all cases, and the mass savings with respect to the baseline are even better: for full carbon spar caps, mass savings of 50% with respect to the baseline were observed.

From this research, it can be concluded that the aeroelastic model makes it possible to perform a complete blade optimisation for different wind turbine blades from which it is possible to extract new design rules or adapt previous ones. It seems that the classical power laws used for upscaling of the blades are not consistent in estimating blade masses for the 10MW and 20MW blades. This was observed for the quasi-isotropic blade as well as for the tailored blade. Further-

more, significant mass savings can be achieved provided that the variable stiffness concept is used. Both the sandwich or the stiffened skin configuration give blade mass values that stay significantly below the baseline designs.

5.2 Recommendations

Equal fidelity aeroelastic model

Since the present research only considers static aeroelastic results, it is of importance to consider dynamic aeroelastic results as well to be sure that the static design is also resisting dynamic loads. Optimisations including dynamic and fatigue loads should be performed, however, the turbine blade still must be subjected to some extreme gusts to see whether the blade is resisting those loads. This means that an unsteady aerodynamic model should be implemented. For a full dynamic aeroelastic analysis, a structural dynamics model must be implemented as well.
Another issue considering the aerodynamics is the cylindrical wake. Physically, the wake behind the wind turbine rotor shows expansion which causes some reduction of the aerodynamic loading. It is suggested to implement an iterative algorithm that runs together with the aeroelastic iteration. This means that during each load iteration the aerodynamic influence coefficients are not only evaluated due to the blade deformation but also due to the change in shape of the wake. The underlying mechanism is to alter the wake vorticity until the wake is force-free, which is not the case for the cylindrical wake assumption.
During this research, the blade is assumed to remain in aerodynamic conditions in which the flow over the blade stays attached. For a more practical vortex distribution in the blade root section, a static stall model has to be implemented, and the vortex model exchanges information with the airfoil tables by means of another Newton-Raphson root finding algorithm for quick convergence, to assure the efficient computational effort of the aeroelastic model.

Optimisation

As concluded in this research, the stiffened skin blade structural configuration gives higher mass results than the sandwich blades. Due to the fixed skin stiffening properties as stringer pitch and stringer shape, the skin is not fully optimised for buckling. The stringer pitch has to be included in the optimisation as well, just as the sandwich core is a design variable for the sandwich blade. A problem could arise here, namely that the computational effort might not be an advantage even considering the aeroelastic model. Due to the differences between the sandwich layout and the stiffened skin layout, it is suggested to redo the optimisations choosing a different objective function that includes the cost aspect to see which

structural layout is most favourable.
All optimisations are performed by assuming balanced laminates. To find out whether increased mass saving can be accomplished, an investigation with unbalanced laminates has to be carried out. Also, unsymmetric laminates have to be a subject of future studies on structural blade mass minimisation when out of autoclave curing happens.

Outlook

The main conclusion of this work is, that variable stiffness multi-material composite blades with sandwich spar caps are promising for future large wind turbines. One of the challenges is to get the variable stiffness blade concept within the certification procedures of wind turbines. This means that a lot of research has to be done on building and testing such blades and to formulate valid certification rules for safe use of such blades.

A

CLASSICAL LAMINATE THEORY FORMULAE

A short overview is given on stacking sequence, constructing the **ABD** matrices and the relation with lamination parameters, since lamination parameters are defined as the design variables in the optimisations during this thesis. The axis system used for the laminate is shown in A.1.

The stress-strain relation of a rotated single composite layer can be written as:

$$\begin{pmatrix} \sigma_x \\ \sigma_y \\ \tau_{xy} \end{pmatrix}_k = \overline{\mathbf{Q}}_k \begin{pmatrix} \epsilon_x \\ \epsilon_y \\ \gamma_{xy} \end{pmatrix}_k \tag{A.1}$$

The rotated stiffness matrix $\overline{\mathbf{Q}}_k$ exists of the original stiffness matrix $\mathbf{Q}_k$ that is altered by a co-ordinate transformation matrix $\mathbf{T}$ and a transformation matrix $\mathbf{R}$ to compensate the difference between the tensorial shear strain and the engineering shear strain. The matrices $\mathbf{T}$ and $\mathbf{R}$ are written as:

$$\mathbf{T} = \begin{pmatrix} \cos^2\theta & \sin^2\theta & 2\cos\theta\sin\theta \\ \sin^2\theta & \cos^2\theta & -2\cos\theta\sin\theta \\ -\cos\theta\sin\theta & \cos\theta\sin\theta & \cos^2\theta - \sin^2\theta \end{pmatrix} \tag{A.2}$$

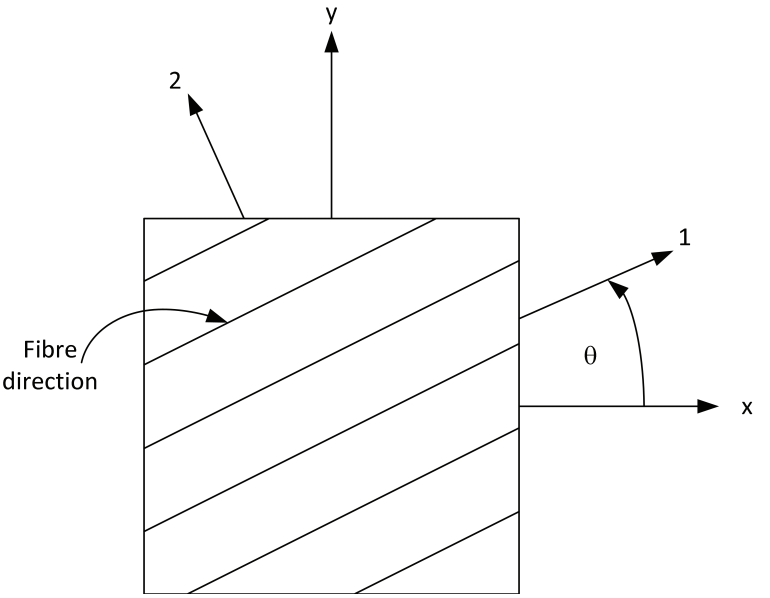

Figure A.1: Axis system for a laminate

and

$$\mathbf{R} = \begin{pmatrix} 1 & 0 & 0 \\ 0 & 1 & 0 \\ 0 & 0 & 2 \end{pmatrix} \tag{A.3}$$

.

The relation between $\mathbf{Q}_k$ and the rotated stiffness matrix $\overline{\mathbf{Q}}_k$ is eventually written as:

$$\overline{\mathbf{Q}} = \mathbf{T}^{-1}\mathbf{Q}\mathbf{R}\mathbf{T}\mathbf{R}^{-1} \tag{A.4}$$

where $\mathbf{Q}$ is the local, non-rotated, stiffness matrix of a single layer in 12 direction:

$$\mathbf{Q} = \begin{pmatrix} Q_{11} & Q_{12} & 0 \\ Q_{12} & Q_{22} & 0 \\ 0 & 0 & Q_{66} \end{pmatrix} \tag{A.5}$$

and the single elements of the $\mathbf{Q}$ read:

$$
\begin{aligned}
Q_{11} &= \tfrac{E_1}{1-\nu_{12}\nu_{21}}, \\
Q_{22} &= \tfrac{E_2}{1-\nu_{12}\nu_{21}}, \\
Q_{12} &= \tfrac{\nu_{12}E_2}{1-\nu_{12}\nu_{21}} = \tfrac{\nu_{21}E_1}{1-\nu_{12}\nu_{12}}, \\
Q_{66} &= G_{12}.
\end{aligned}
\tag{A.6}
$$

B

STRAIN AND BUCKLING OF OPTIMISED DESIGNS

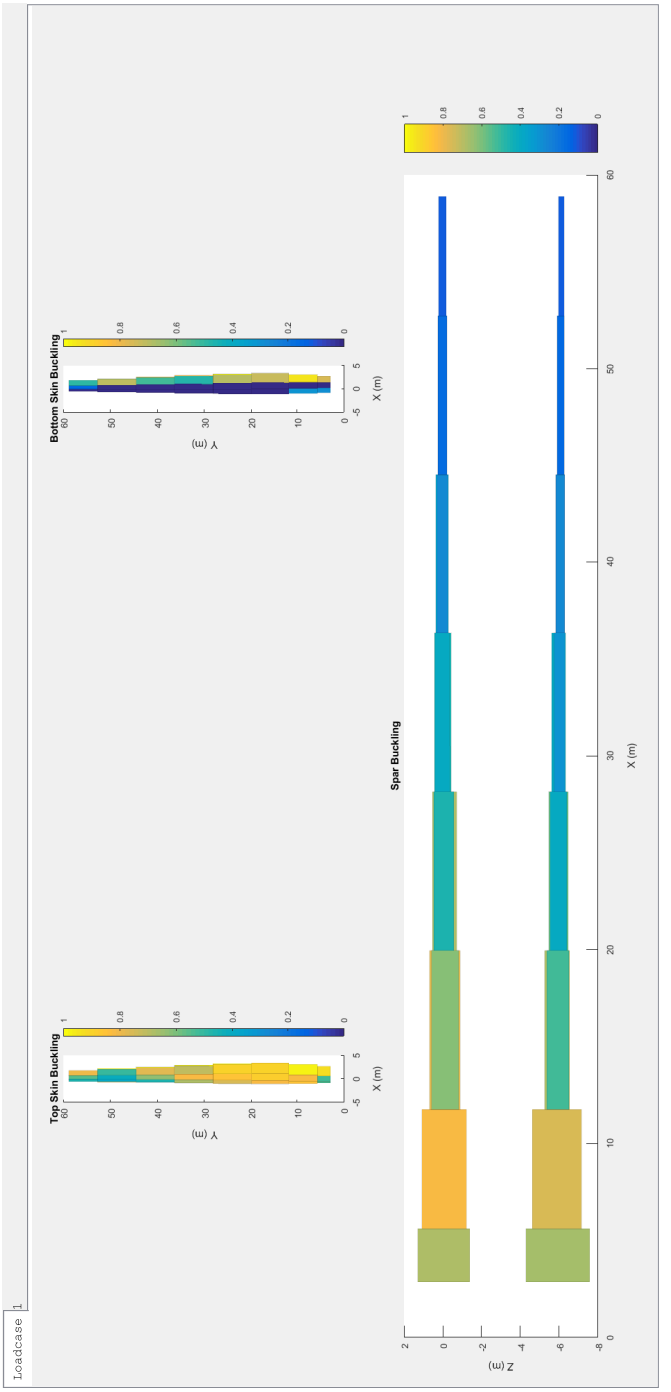

Figure B.1: Buckling constraints of 5MW sandwich blade for EWS at 11.4 m/s.

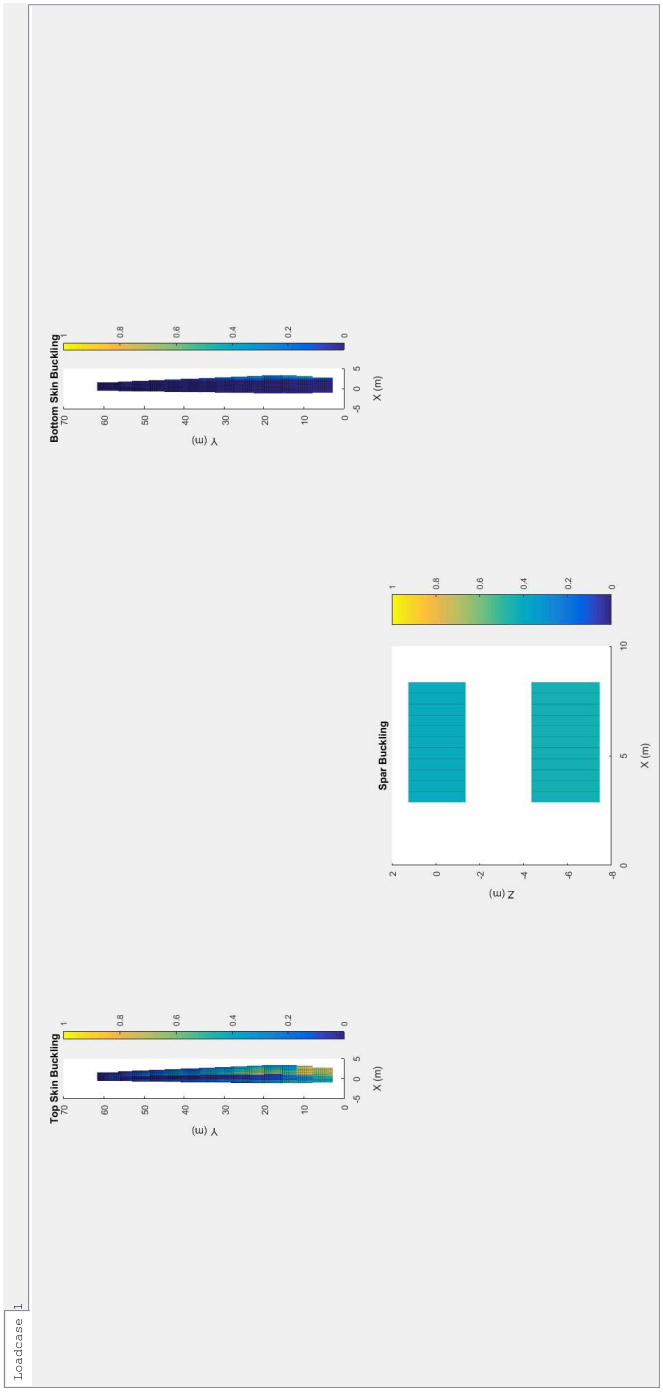

Figure B.2: Buckling constraints of 5MW stiffened skin blade for EWS at 11.4 m/s.

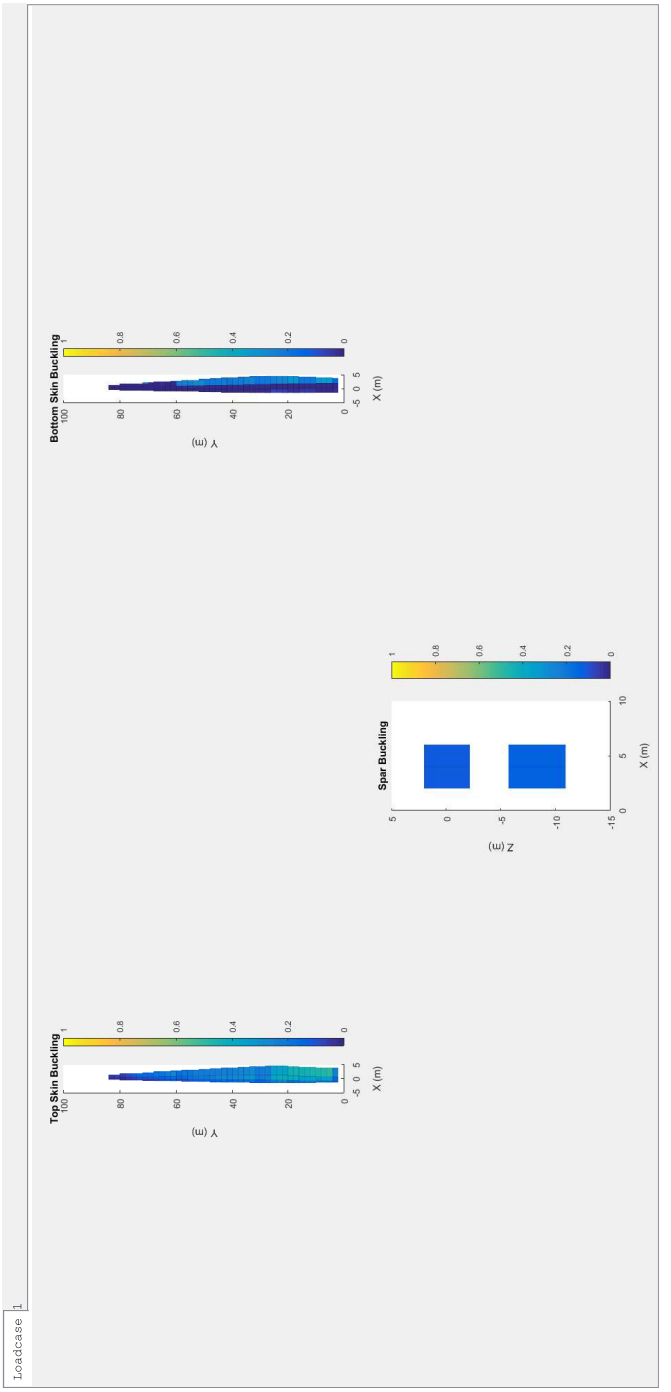

Figure B.3: Buckling constraints of 10MW sandwich blade for EWS at 11.4 m/s.

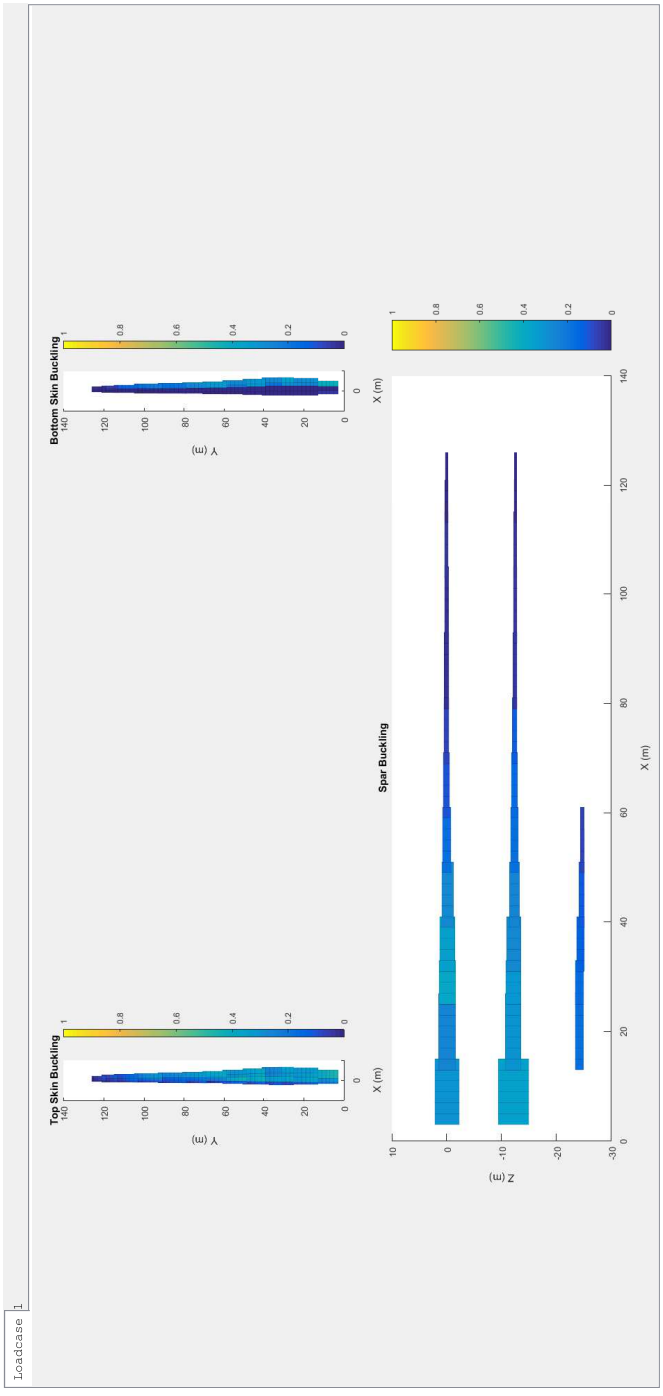

Figure B.4: Buckling constraints of 20MW sandwich blade for EWS at 11.4 m/s.

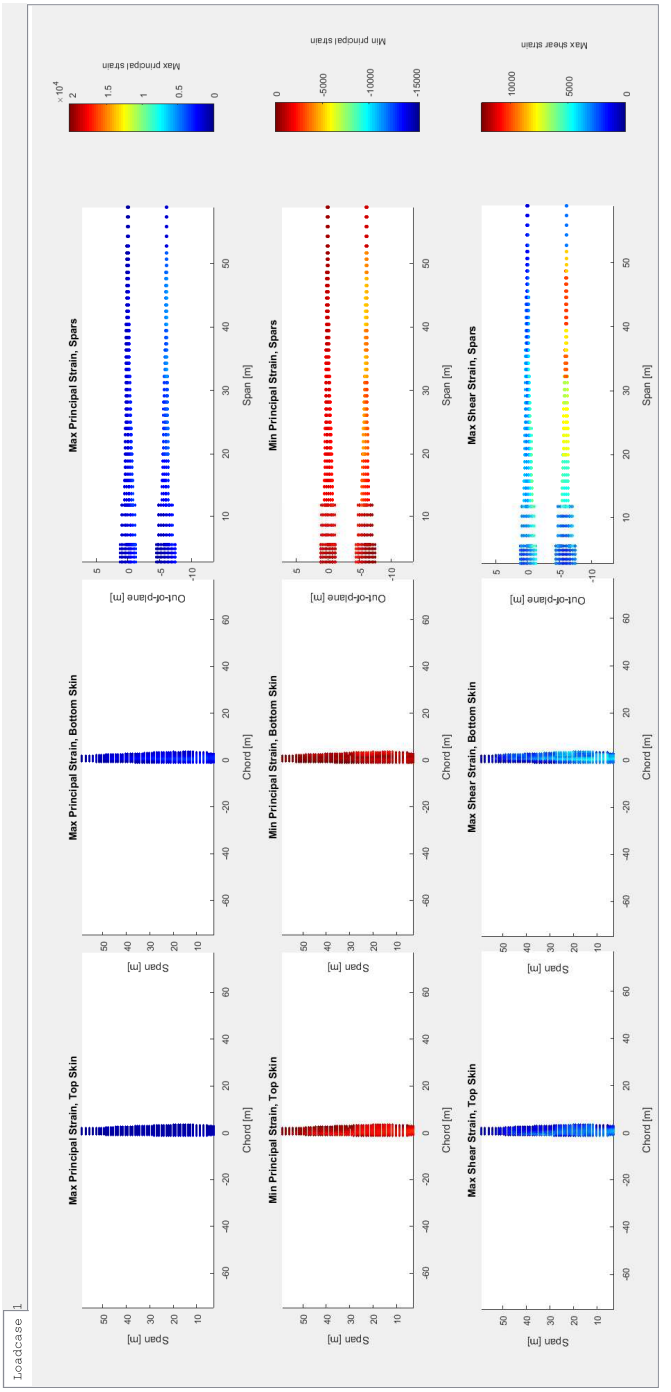

Figure B.5: Strain constraints of 5MW sandwich blade for EWS at 11.4 m/s.

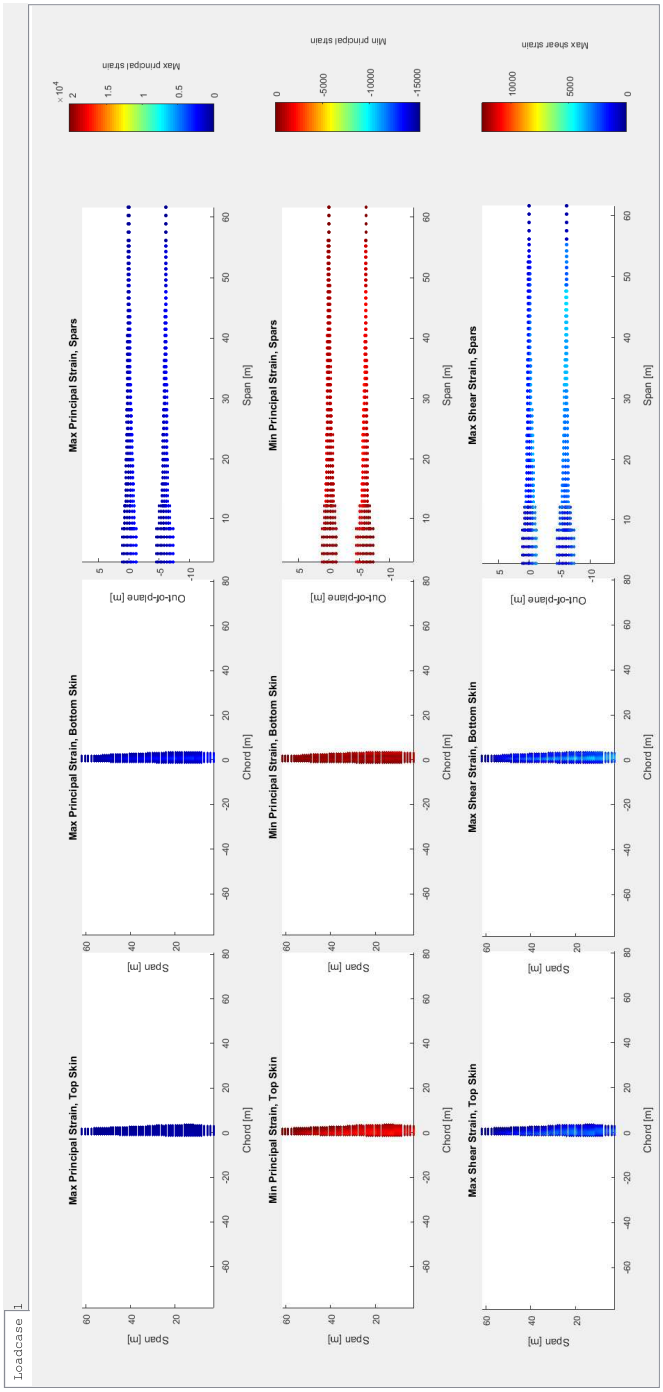

Figure B.6: Strain constraints of 5MW stiffened skin blade for EWS at 11.4 m/s.

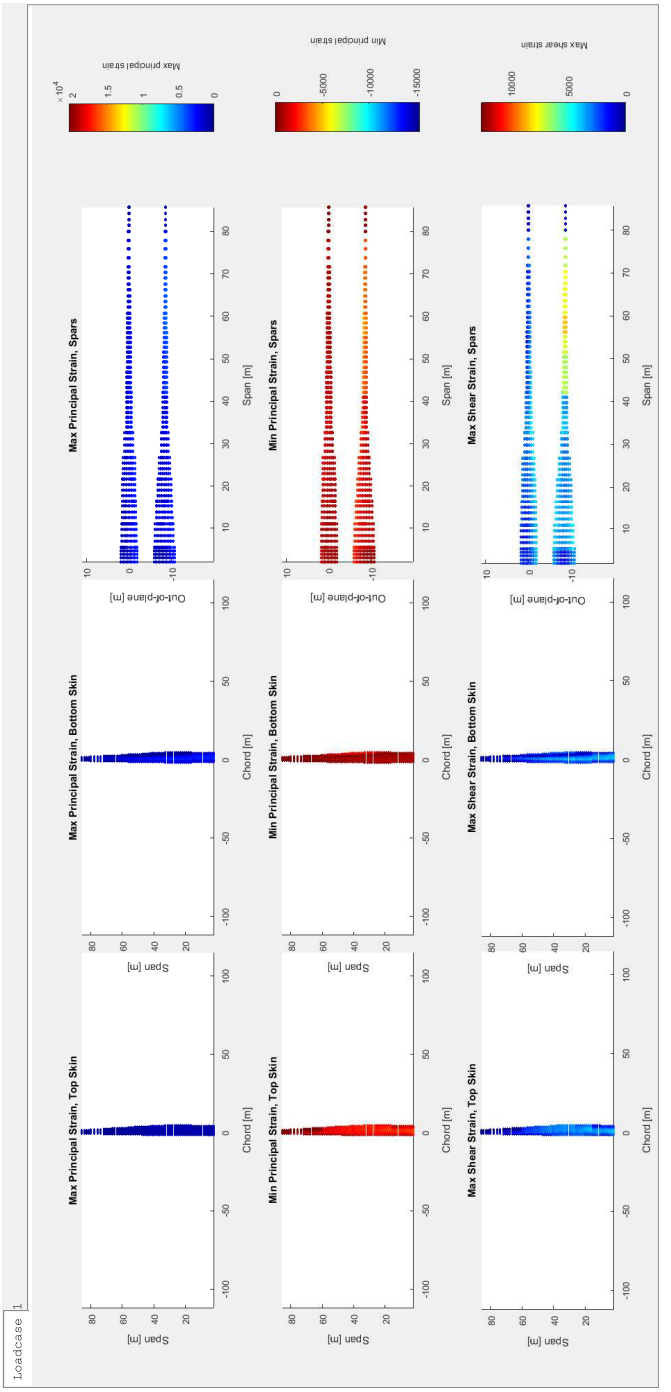

Figure B.7: Strain constraints of 10MW sandwich blade for EWS at 11.4 m/s.

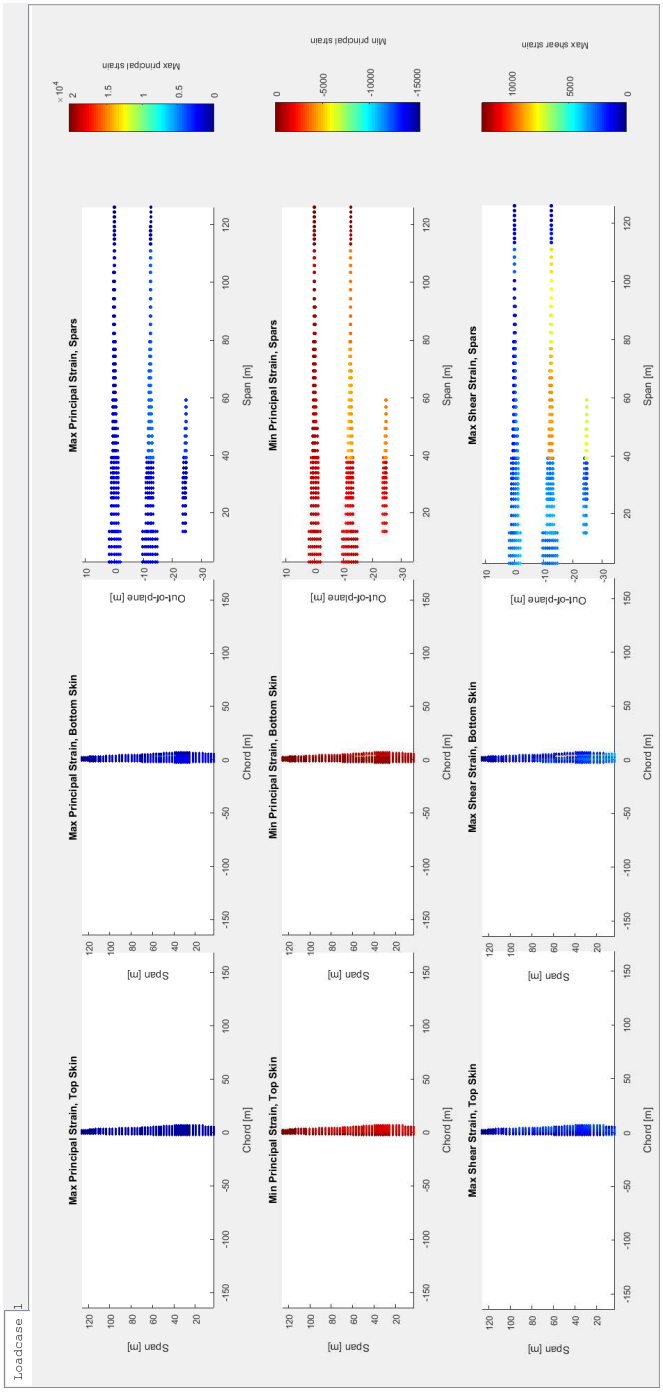

Figure B.8: Strain constraints of 20MW sandwich blade for EWS at 11.4 m/s.

C

AERODYNAMIC POWER CONSTRAINTS

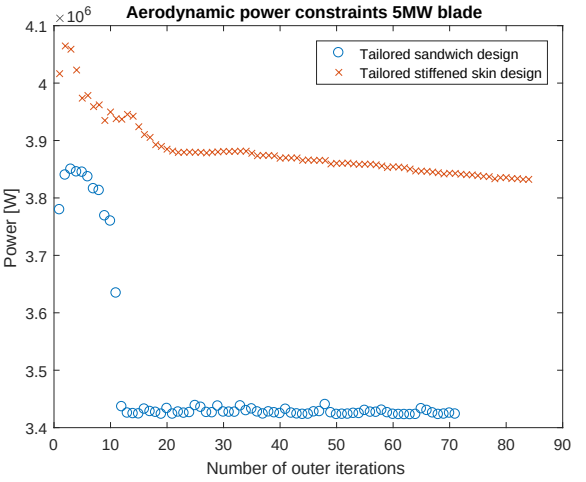

Figure C.1: Aerodynamic power constraints of 5MW blade for EWS at 11.4 m/s as a function of the number of outer iterations. In this graph, the difference of the stiffened skin concept versus the sandwich concept is shown.

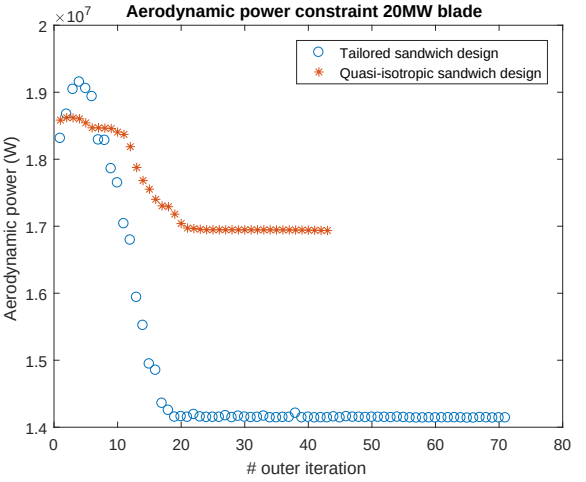

Figure C.2: Aerodynamic power constraints of the 20MW blade for EWS at 11.4 m/s as a function of the number of iterations. In this graph, the difference between a quasi-isotropic blade and a tailored blade is shown.

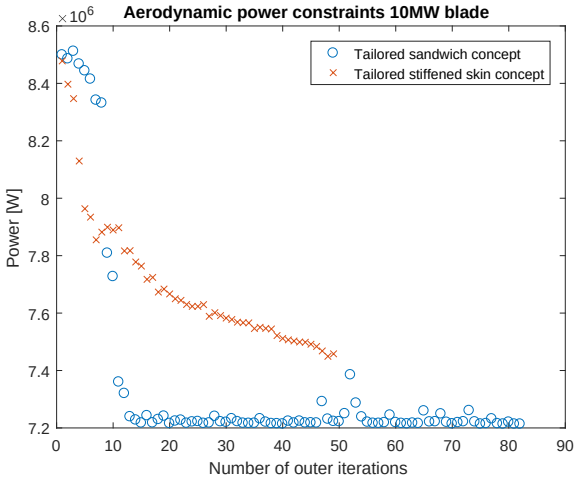

Figure C.3: Aerodynamic power constraints of the 10MW blade for EWS at 11.4 m/s as a function of the number of iterations. In this graph, the difference between a tailored sandwich design and a tailored stiffened skin design is shown.

BIBLIOGRAPHY

[Aerotrope, 1995] Aerotrope (1995). Carter 300 kW Two-Bladed Wind Turbine.

[Amin et al., 2012] Amin, M. M., Ghadiri, B., Abdalla, M. M., Haddadpour, H., and De Breuker, R. (2012). Continuous-time state-space unsteady aerodynamic modeling based on boundary element method. *Engineering Analysis with Boundary Elements*, 36:789–798.

[Ashuri, 2012] Ashuri, T. (2012). *Beyond Classical Upscaling: Integrated Aeroservoelastic Design and Optimization of Large Offshore Wind Turbines*. PhD thesis, Delft University of Technology.

[Ashuri et al., 2010] Ashuri, T., Bussel, v. G., Zaaijer, M., and Kuik, v. G. (2010). An analytical model to extract blade structural properties for optimisation and up-scaling studies. In *The Science of Making Torque form Wind, Heraklion, Crete, Greece, 28-30 June, 2010*.

[Bak et al., 2013] Bak, C., Zahle, F., Kim, T., Yde, A., Henriksen, L., Natarajan, A., and Hansen, M. (2013). Description of the DTU 10MW reference 5 wind turbine. Technical Report DTU Wind Energy-I-0092.

[Bernhammer, 2015] Bernhammer, L. (2015). *Smart Wind Turbine: Analysis and Autonomous Flap*. PhD thesis, Delft University of Technology.

[Bielawa, 1971] Bielawa, R. (1971). Techniques for stability analysis and design optimization with dynamic constraints of nonconservative linear systems. In *AIAA paper 71 - 388, 1971*.

[Blasques and Lazarov, 2011] Blasques, J. and Lazarov, B. (2011). BECAS - a beam cross-section analysis tool for anisotropic and inhomogeneous sections of arbitrary geometry. Technical Report RISO R 1785 Technical Report.

[Bottasso et al., 2016] Bottasso, C. L., Bortolotti, P., Croce, A., and Gualdoni, F. (2016). Integrated aero-structural optimization of wind turbines. *Multibody System Dynamics*, 38(4):317–344.

[Burger and Hartfield, 2006] Burger, C. and Hartfield, R. (2006). Wind turbine airfoil performance optimization using the vortex lattice method and a genetic algorithm. In *4th AIAA Energy Conversion Engineering Conference, San Diego, California, US, June 26 - June 29, 2006*.

[Carreira, 2009] Carreira, X. M. (2009). The skew non-orthogonal reinforcement problem.

[Castillo Capponi et al., 2011] Castillo Capponi, P., Bussel, v. G., Ashuri, T., and Kallesøe, B. (2011). A nonlinear upscaling approach for wind turbine blades based on stresses. In *EWEA 2011, Scientific Proceedings*.

[Cesnik and Hodges, 1997] Cesnik, C. E. and Hodges, D. H. (1997). VABS: A new concept for composite rotor blade cross-sectional modeling. *Journal of the American Helicopter Society*, 42(1):27–38.

[Chandra and Chopra, 1992] Chandra, R. and Chopra, I. (1992). Structural response of composite beams and blades with elastic couplings. *Composites Engineering*, 2(5-7):347–374.

[Chaviaropoulos, 2007] Chaviaropoulos, P. (2007). Similarity rules for wind turbine up-scaling. *Report no. WP 1B4, Upwind*.

[Chehouri et al., 2015] Chehouri, A., Younes, R., Ilinca, A., and Perron, J. (2015). Review of performance optimisation techniques applied to wind turbines. *Applied Energy*, 142:361–388.

[Chen, 2010] Chen, H. e. a. (2010). A critical assessment of computer tools for calculating composite wind turbine blade properties. *Wind Energy*, 13(6):497–516.

[Crisfield, 1986] Crisfield, M. (1986). *Finite elements and solution procedures for structural analysis*. Pineridge Press.

[De Breuker, 2011] De Breuker, R. (2011). *Energy-based Aeroelastic Analysis and Optimisation of Morphing Wings*. PhD thesis, Delft University of Technology.

[Dillinger, 2014] Dillinger, J. (2014). *Static Optimization of Composite Wings with Variable Stiffness Laminates*. PhD thesis, Delft University of Technology.

[Dumitrescu and Cardoş, 2001] Dumitrescu, H. and Cardoş, V. (2001). Prediction of unsteady hawt aerodynamics by lifting line theory. *Mathematical and Computer Modelling*, 33:469–481.

[Ferede, 2016] Ferede, E. (2016). *Static Aeroelastic optimization of Composite Wind Turbine Rotor Blades using Variable Stiffness Laminates*. PhD thesis, Delft University of Technology.

[Fingersh et al., 2006] Fingersh, L., M., H., and Laxon, A. (2006). Wind turbine design cost and scaling models. Technical Report NREL/TP-500-40566.

[Freno et al., 2011] Freno, B. A., II, R. L. B., and Cizmas, G. (2011). The role of structural nonlinearities in wind turbine blade aeroelastic analysis. In *49th AIAA Aerospace Sciences Meeting including the New Horizons Forum and Aerospace Exposition*.

[Gaudern and Symons, 2010] Gaudern, N. and Symons, D. D. (2010). Comparison of theoretical and numerical buckling loads for wind turbine blade panels. *Wind Engineering*, 34(2):193–206.

[Goeij, 1999] Goeij, d. J. (1999). Implementation of bending-torsion coupling in the design of a wind-turbine rotor-blade. *Applied Energy*, 63:191–207.

[Guermond, 1990] Guermond, J.-L. (1990). A generalized lifting-line theory for curved and swept wings. *Journal of Fluid Mechanics*, 211:497–513.

[Guyan, 1965] Guyan, R. (1965). Reduction of stiffness and mass matrices. *AIAA Journal*, 3(2):380.

[Hammer et al., 1997] Hammer, V., Bendsøe, M., Lipton, R., and Pedersen, P. (1997). Parametrization in laminate design for optimal compliance. *International Journal of SOlids and Structures*, 31(4):415–434.

[Hansen, 2003] Hansen, M. (2003). *Aerodynamics of Wind Turbines*. James & James Ltd, 2nd edition.

[Hansen et al., 2006] Hansen, M., Sørensen, J., Voutsinas, S., Sørensen, N., and Madsen, H. A. (2006). State of the art in wind turbine aerodynamics and aeroelasticity. *Progress in Aerospace Sciences*, 42:285–330.

[Hodges and Yu, 2007] Hodges, D. and Yu, W. (2007). A rigorous, engineer friendly, approach for modelling realistic, composite rotor blades. *Wind Energy*, 10:179–193.

[Hollaway, 1994] Hollaway, L. e. (1994). *Handbook of Polymer Composites for Engineers*. Woodhead.

[IEA, 2015] IEA (2015). Iea wind task 37. https://windbench.net/iea37.

[IEC, 2005] IEC (2005). *International standard IEC 61400-1, part 1: Design requirements*. Third edition.

[Jackson et al., 2005] Jackson, K., Zuteck, M., van Dam, C., Standish, K., and Berry, D. (2005). Innovative design approaches for large wind turbine blades. *Wind Energy*, 8:141–171.

[Joncas, 2010] Joncas, S. (2010). *Thermoplastic Composites Wind Turbine Blades*. PhD thesis, Delft University of Technology.

[Jonkman et al., 2009] Jonkman, J., S, B., Musial, W., and Scott, G. (2009). Definition of a 5mw reference wind turbine for offshore system development. Technical Report NREL/TP-500-38060.

[Jureczko et al., 2005] Jureczko, M., Pawlak, M., and Mezik, A. (2005). Optimisation of wind turbine blades. *Journal of Material Processing Technology*, 167(2-3):463–471.

[Karaolis et al., 1989] Karaolis, N., Jeronimidis, G., and Mussgrove, P. (1989). Composite wind turbine blades: coupling effects and rotor aerodynamic performance. In *European Wind Energy Conference and Exhibition 1989*.

[Katz and Plotkin, 2001] Katz, J. and Plotkin, A. (2001). *Low-Speed Aerodynamics*. Cambridge, 2nd edition.

[Leishman, 2002] Leishman, G. J. (2002). Challenges in modelling the unsteady aerodynamics of wind turbines. In *21^{st} Wind Energy Symposium and the 40^{th} AIAA Aerospace Sciences meeting*.

[Liao et al., 2012] Liao, C., Zhao, X., and Xu, J. (2012). Blade layers optimisation of win turbines using fast and improved pso algorithm. *Renewable Energy*, 42:227–233.

[Luo, 2008] Luo, Y. (2008). An efficient 3d timoshenko beam element with consistent shape functions. *Advances in Theoretical and Applied Mechanics*, 1(3):95–106.

[Nijssen et al., 2001] Nijssen, R., Zaaijer, M., Bierbooms, W., Kuik, v. G., Delft, v. D., and Holten, v. T. (2001). The application of scaling rules in up-scaling and marinisation of a wind turbine. In *European Wind Energy Conference and Exhibition, Copenhagen, Denmark, July 2001*.

[Passon et al., 2007] Passon, P., Kuhn, M., Butterfield, S., Jonkman, J., Camp, T., and Larsen, T. (2007). OC3-benchmark exercise of aeroelastic offshore wind turbine codes. *Journal of Physics, Conference Series*, 75(012071).

[Peeringa et al., 2011] Peeringa, J., Brood, R., Ceyhan, O., Engels, W., and de Winkel, G. (2011). Upwind 20MW Wind Turbine Pre-Design. Technical Report ECN-E–11-017.

[Prandtl and Tietjens, 1957] Prandtl, L. and Tietjens, O. (1957). *Fundamentals of Hydro- and Aeromechanics*. Dover Publications Inc., 2^{nd} edition.

[Sanderse, 2009] Sanderse, B. (2009). Aerodynamics of wind turbine wakes, a literature review. Technical Report ECN-C-09-016.

[Scott et al., 2017] Scott, S., Capuzzi, M., Langston, D., Bossanyi, E., McCann, C., Weaver, P. M., and Pirrera, A. (2017). Effects of aeroelastic tailoring on performance characteristics of wind turbine systems. *Renewable Energy*, 114:887–903.

[Sieros et al., 2012] Sieros, G., Chaviaropoulos, P., Sørensen, J., Bulder, B., and Jamieson, P. (2012). Up-scaling wind turbines: Theoretical and practical aspects and their impact on the cost of energy. *Wind Energy*, (1):3–17.

[Svanberg, 2002] Svanberg, K. (2002). A class of globally convergent optimization methods based on conservative convex separable approximations. *SIAM Journal on Optimisation*, 12(2):555–573.

[Timmer, 2017] Timmer, W. (2017). airfoil co-ordinated du shapes. In *personal communication*.

[Troen and Lundtang Petersen, 1989] Troen, I. and Lundtang Petersen, E. (1989). *Eureopean Wind Atlas*. Risø National Laboratory, 1^{st} edition.

[Tsai and Hahn, 1980] Tsai, S. and Hahn, H. (1980). *Introduction to Composite Materials*. Technomic Publishing Co.

[Tsai and Pagano, 1968] Tsai, S. and Pagano, N. (1968). Invariant properties of composite materials. Technical Report AIR FORCE MATERIALS LAB WRIGHT-PATTERSON OHIO.

[van Bussel, 1992] van Bussel, G. (1992). The use of the asymptotic acceleration potential method for horizontal axis wind turbines aerodynamics. *Journal of Wind Engineering and Industrial Aerodynamics*, 39:161–172.

[van Bussel, 2010] van Bussel, G. (December, 2010). Wind turbine performance calculations. Wind turbine performance calculation Excel sheet.

[van Garrel, 2003] van Garrel, A. (2003). Development of a wind turbine aerodynamics simulation module. Technical Report ECN-C–03-079.

[van Holten, 1976] van Holten, T. (1976). Some notes on unsteady lifting-line theory. *Journal of Fluid Mechanics*, 77:561–579.

[Veers et al., 1998] Veers, P., Bir, G., and Lobitz, D. (1998). Aeroelastic tailoring in wind turbine blade applications. In *Windpower 98, American Wind Energy Assocoiation Meeting and Exhibition, Bakersfield, California, US, April 28 - May 1, 1998*.

[Weisshaar, 1987] Weisshaar, T. (1987). Aeroelastic tailoring - creative use of ubusual materials. In *28^{th} Structures, structural dynamics and Materials conference, Monterey, CA, 6-8 April 1987*.

[Werter, 2017] Werter, N. (2017). *Aeroelastic Modelling and Design of Aeroelastically Tailored and Morphing Wings*. PhD thesis, Delft University of Technology.

[Werter et al., 2017] Werter, N. P. M., De Breuker, R., and Abdalla, M. M. (2017). Continuous-time state-space unsteady aerodynamic modeling for efficient loads analysis. *AIAA Journal*, 56(2):1–12.

[Willaert and Abdalla, 2010] Willaert, M. and Abdalla, M. (2010). A simple finite element cross-sectional modelling of thin-walled beams. In *Proceedings of the 2nd Aircraft Structural Design Conference*.

[Zhale et al., 2016] Zhale, F., TIbaldi, C., Pavese, C., McWilliam, M. K., Blasques, J. P., and Hansen, M. H. (2016). Design of an aeroelastically tailored 10 mw wind turbine rotor. In *Journal of Physycs: Conference series 753, 062008*.

[Zhu et al., 2012] Zhu, J., Cai, X., Pan, P., and Gu, R. (2012). Optimization design of spar cap layup of wind turbine. *Frontiers of Structural and Civil Engineering*, 6(1):53–56.

[Zhu et al., 2014] Zhu, J., Cai, X., Pan, P., and Gu, R. (2014). Multi-objective structural optimization design of horizontal-axis wind turbine blades using the non-dominated sorting genetic algorithm ii and finite element method. *Energies*, 7:988–1002.

ACKNOWLEDGEMENTS

Finally! It is done! Nine years of work, combined with a growing family (Gohan was born in 2014 and Jadzia in 2016), and the teaching job at Inholland University of Applied Sciences. I don't know how I did it, but I succeeded! Of course, I could not have succeeded without the help of many people. First of all, I have to thank my beloved wife, who took care of my children while I worked at some part of the Matlab code, writing a paper, or something like that. Secondly, Inholland made it possible to do this research during the past nine years. Many thanks to my employer. Then, of course, I have to thank both promotors Roeland De Breuker and Gerard van Bussel for their valuable suggestions and sometimes they provided me of new and necessary motivation to continue the research and finishing it.

Next, I should apologise to my colleagues, for the complains they had to listen to after they asked the question: "How are things with your Ph.D. research?". Few colleagues were willing to listen more closely to the problems I encountered, which helped me a lot for continuing the research: thank you Arjan, Jan, Pieter and John! One colleague I must mention as well: Marjoke Cornelissen. She passed away in December 2017. I miss her very much and I regret that she cannot celebrate the final steps in my PhD adventure.

During the nine years, I shared my room with several Fellow Ph.D.s. I want to thank you guys, for all good times we had during this nine years. Especially in the early days of the adventure, I shared the room with Glenn, Mathieu and Mohammed. We had a lot of fun back then, thank you all guys.

Last but not least, I want to thank my parents and parents in law for the relaxing moments that are very necessary during a Ph.D.!

Terry
Den Hoorn, January 2019.

BIOGRAPHICAL NOTE

Terry Hegberg was born on April 29, 1970, in Zaandam, The Netherlands where he grew up. He followed his High-school education at the Zaanlands Lyceum, which he completed in 1990. In 1990 he started the study of Aeronautical Engineering at the University of Applied Sciences in Haarlem. After graduating in 1994, he followed a master in Delft, University of Technology at the faculty Aerospace Engineering. He graduated in 1998 in the field of aeroelasticity and helicopter rotor blades. In the same year, he started a job at the Energy research centre of the Netherlands at the wind energy department where he did research on aeroelastic behaviour of wind turbines, wind power meteorology and wind farm design. In 2005 he switched jobs and became a teacher at Inholland University of Applied Sciences, Aeronautical Engineering. In 2009 he started a part-time Ph.D. research track in collaboration with the Delft University of Technology, which he finished in 2019.